

PEPTIDE EPITOPE FUNCTIONALIZED MONOLAYER-PROTECTED CLUSTERS
FOR LIFE SCIENCE APPLICATIONS

By

Aren E. Gerdon

Dissertation

Submitted to the Faculty of the
Graduate School of Vanderbilt University
in partial fulfillment of the requirements
for the degree of

DOCTOR OF PHILOSOPHY

in

Chemistry

December, 2006

Nashville, Tennessee

Approved:

Professor David E. Cliffel

Professor David W. Wright

Professor Ned Porter

Professor Eva Harth

Professor Raymond Mernaugh

ACKNOWLEDGEMENTS

The last twenty one years of my life have been dominated by academics and education, in one form or another. I would sincerely like to thank all the educators and mentors that I have benefited from along the way. I would not have made it this far without them. In high school I was exceptionally influenced by the unstoppable Glen Menke, who has a serious devotion to science and his students and who introduced me to a cornucopia of chemistry, and the unpredictable Keith Younker, who was excentric enough to encourage my creative and critical thinking. Both of these instructors also provided me with my first taste of freedom in academics, which is so often stifled in primary and secondary education.

Hanover College was the ideal environment for my undergraduate education and I would like to particularly thank Paul Austin and Paul Ellefsen. I thank Dr. Ellefsen for his unyielding knowledge of analytical instrumentation, his unflinching and sometimes brash handling of unknown chemicals, and for setting me lose on a room full of expensive tools. Dr. Austin had a major impact on my scientific education and I owe much of my excitement of chemistry and biochemistry to him. I appreciate the hours that he allowed me to argue about the nuances of general chemistry, the time he spent mentoring me in my classwork and labwork, and his support in the development of my leadership skills. He is a true mentor and a valuable resource to all students willing to learn from him. He is the main reason I aspire to teaching.

I would also like to thank my advisors during this final aspect of my formal education. I began interacting with David Cliffel and David Wright as soon as I arrived on campus and though I tried to escape through various rotations I simply couldn't evade

their combined genius. I feel as though I should thank the Davids together as they were often side-by-side in my many formal presentations and hallway or office conversations. I should also thank them separately as, though they work well together, they often have different approaches to the same problem. This duality was a major advantage in my graduate education. I appreciate David Cliffler's patience and availability in the many times I knocked on his office door aggressively refusing to be deterred by his apparent work or grant due the next day. Similarly, I appreciate his ability to let me work independently. I also admire his hard work and dedication to science as well as his analytical chemistry prowess. In quite the opposite way, I would like to thank David Wright for his constant badgering, barrage of aggressive questions, and seriously intense group meetings, which helped my confidence in scientific discussions. David was always available when experiments were failing or the next step was unclear to me. His critical and creative thinking are truly admirable and I aspire to that level of scientific knowledge and thought. What excitement about science I didn't obtain from Paul Austin was quickly filled in by David Wright, as he is the most excited and excitable man I've yet to know. I would also like to thank David for transferring his appreciation for finer things such as good beer, scotch, wine, music, literature, and fountain pens. I would also like to apologize to David for shamelessly kicking his ass so many times. I learned a great deal about science, research, science education, and the politics of science from both of these individuals.

My dissertation committee including Ned Porter, Eva Harth, and Ray Mernaugh and collaborators including James Crowe and David Hercules were also helpful mentors in scientific discussions and in making me a better scientist. I would particularly like to

thank Dr. Porter for his convincing me to attend Vanderbilt University and his help with funding. I also need to thank the Vanderbilt Institute of Chemical Biology, the Chemical Biology Interface training grant, the National Institute of Health, the Vanderbilt Institute of Nanoscale Science and Engineering, and the Southeast Regional Center for Excellence in Biodefense for funding.

Next I would like to thank all those members of the Cliffel and Wright groups that I interacted with and learned from along the way. Sven Eklund, Madalina Ciobanu in her meticulous work, and Morgan Krim (Golden Boy) had an early influence on my work in the Cliffel lab that I much appreciate. Rachel Peterson, Grey Tilden, Dale Taylor, Helen Kincaid, Jeremy Wilburn, Rachel Snider, Brian Huffman, Joe Chambers, Brian Turner, Brian Hixson, Yibin Zhang, Xun Yan, and Chris Green also have my thanks. I was Karl Richardson's graduate student and I was fortunate to have had the opportunity to work with/for him. He helped me learn a lot about mentoring. In the Wright lab I appreciate the help of Lisa Pasierb, Clare Kenny, Marc Knecht, Scott Miller, Liddy Bentzen, Sarah Sewell, Ryan Rutledge, Reese Harry, Kristin Halfpenny, Alex Schrimpe, Goska Broncel, Jonas Perez, Melissa Carter, and Leila Deravi. I particularly would like to thank Joe Slocik for introducing me to the nanolegacy and for his interesting approach to work in the Wright lab; Crystal Miller for being the best damn softball coach out there; and Reese Harry for being the most drunk person in the room at any given point in time.

Upon arriving at Vanderbilt I promptly informed my peers that there is more to life than chemistry. I would very much like to thank all those that helped me keep my sanity and focus with constant diversions. The 8th floor lunch crowd, spanning many classes of students, always got me through the middle of the day. Thanks to Sheerin

Shahidi and Joe Ferguson for helping me realize my polish heratige; Matt Wellons and Kyle Brown for important planning meetings and exploring Tennessee; Mike Warnement and Chris Rector for sweating over the hot coals burning uncooked brats; Keith Quissenbery for endless entertainment while lifting weights; Provence for the best coffee in town and fantastic chocolate crossaints; Mr. Burns for providing low cost housing near campus; and Sam's for happy hour, hot wings, and pizza. Most importantly I really want to thank Rosemary White for so many things. We struggled through Dr. Lowe's and many other's classes together. We worked side-by-side on all our exams and formal presentations. Her hard work and dedication inspired the same in me. She provided endless amounts of laughter, work, fun, and stress and I sincerely appreciate it all of it.

Finally, I would like to thank my family for all their love and support over the years. Ian, especially, has never stopped pushing me in academic matters, be it my research, evolution, existentialism, Catholicism, or any other topic. He is the eternal academic and I admire that. I owe much of my success to my parents, Doug and Anita Gerdon. Their love and support of my many various endeavors has been unflinching. Most importantly, they taught me the meaning of hard work, unselfishness, and leadership. For that I owe them everything.

TABLE OF CONTENTS

	Page
ACKNOWLEDGEMENTS	ii
LIST OF TABLES	viii
LIST OF FIGURES	ix
LIST OF ABBREVIATIONS.....	xiii
 Chapter	
I. INTERFACING BIOLOGY AND NANOMATERIALS FOR SENSING APPLICATIONS	1
Introduction.....	1
II. QUARTZ CRYSTAL MICROBALANCE DETECTION OF GLUTATHIONE-PROTECTED NANOCLUSTERS USING ANTIBODY RECOGNITION	39
Introduction.....	39
Experimental.....	44
Results and Discussion	50
Monolayer-Protected Cluster Synthesis and Characterization	50
Quartz Crystal Microbalance	53
Immunosensor Assembly.....	55
Analyte Detection	59
Conclusions.....	66
III. HEMAGGLUTININ LINEAR EPITOPE PRESENTATION ON MONOLAYER-PROTECTED CLUSTERS ELICITS STRONG ANTIBODY BINDING	68
Introduction	68
Experimental	72
Results and Discussion.....	78
Nanostructure Assembly.....	78
QCM Immunosensor.....	82
Antibody Detection.....	85
Conclusions	88

IV.	ENHANCED ANTIGENICITY OF NANOCCLUSERS PRESENTING CONFORMATIONAL PEPTIDE EPITOPES OF THE PROTECTIVE ANTIGEN OF B. ANTHRACIS.....	89
	Introduction	89
	Experimental	97
	Results and Discussion.....	106
	Antigen Mimic Synthesis and Characterization	106
	Characterization of Epitope Conformation.....	110
	Epitope Mapping.....	113
	Monoclonal Antibody Binding	114
	Antigen Mimic Immunogenicity.....	123
	Conclusions	131
V.	COUPLED MONOLAYER-PROTECTED CLUSTERS EXHIBIT ENHANCED NEAR-IR FLUORESCENCE.....	132
	Introduction	132
	Experimental	134
	Results and Discussion.....	136
	Monolayer-Protected Cluster Synthesis and Characterization	136
	Fluorescence Enhancement of Coupled Nanoparticles.....	139
	Enzymatic Linker Cleavage.....	145
	Conclusions	148
Appendix		
A.	DETECTION OF EBOLA VIRUS GLYCOPROTEINS USING A QUARTZ CRYSTAL MICROBALANCE IMMUNOSENSOR.....	149
B.	QUARTZ CRYSTAL MICROBALANCE STUDY OF PIEZOELECTRIC INK JET PROCESSING OF MATERIALS	153
C.	ELECTROSPRAY MASS SPECTROMETRY STUDY OF TIOPRONIN MONOLAYER-PROTECTED GOLD NANOCCLUSERS	155
D.	SINGLE-CHAIN FRAGMENT-VARIABLE RECOMINANT ANTIBODIES WITH AFFINITY FOR ZERO-VALENT METALS.....	156
	REFERENCES	158
	CURRICULUM VITAE.....	169

LIST OF TABLES

Table	Page
1. Results of calculations from MPC characterization.....	53
2. Data for Δm dependence on flow rate for two doses of equal concentration.....	61
3. Ratio of nanocluster thiolate to exchanging thiolate alters the extent of peptide exchange.....	80
4. Equilibrium association constants and kinetic rate constants for antibody binding to HA-MPC and HA-SAM.....	87
5. Amino acid sequences for peptides used in antigen mimic design	107
6. Final composition of antigen mimics	110
7. Results of immunosensor assembly and for screening monoclonal anti-PA antibodies against four antigen mimics.....	114
8. Results from equilibrium calculations for two antigen mimics and the protective antigen protein.....	115
9. Summary of injection groups and concentrations of antigens used in antibody production assay	123
10. Qualitative Au detection in organ tissue extraction using EDAX.....	125
11. Fluorescence ratio of coupled MPCs relative to uncoupled MPCs.....	142

LIST OF FIGURES

Figure	Page
1. Examples of successful interfaces between biology and inorganic materials.....	4
2. Cartoon structure of a typical IgG antibody.....	6
3. Size comparison between single chain fragment variable antibody and full length antibody.....	7
4. Representative synthesis and characterization for a tiopronin (N-2-mercaptopropionylglycine)-protected cluster.....	9
5. Cartoon schematic of nanocluster presenting antibody and of nanocluster presenting antigen.....	12
6. Possible applications for immuno-functionalized nanoclusters.....	13
7. Top and side view of a QCM resonator and cross sectional view of a QCM resonator in contact with a liquid.....	16
8. Examples of QCM functionalization techniques to impart specificity.....	21
9. Representative QCM-based sensors for chemical, biological, and immunological applications.....	28
10. Structures of cluster-protecting ligands.....	50
11. Characterization data for GSH-MPC and Tiop-MPC.....	51
12. Data from QCM mass calibration.....	54
13. Cartoon of immunosensor assembly.....	55
14. Detection of Cu^{2+} , GSH-MPC, and antibody binding via QCM.....	56
15. Representative Protein A, BSA, IgG, and MPC binding.....	58
16. Antibody recognition and binding of GSH-MPC, followed by non-specific aggregation over an extended period of time, showing no saturation point.....	60
17. Plot of Δm against the [GSH-MPC], linear Langmuir adsorption isotherm fit,	

	and adsorption kinetics fit	63
18.	Binding curves for GSH-MPC doses, Tiop-MPC, and free GSH	64
19.	Cartoon representations of functional nanostructures	70
20.	Cartoon schematic showing one-to-one place exchange between peptide thiolate in solution and thiolate on the surface of an MPC	71
21.	Data for nanocluster characterization.....	78
22.	Data for peptide epitope characterization.....	79
23.	¹ H NMR of Tiop-MPC after place exchange with HA peptide epitope.....	80
24.	Antibody to functionalized nanocluster binding efficiency increases with decreasing density of peptide	81
25.	Electrodeposition of MEAV-HA-MPC	83
26.	Representative polyelectrolyte, HA-MPC, BSA, and anti-HA antibody binding, and representative antibody binding to a mixed, two-dimensional monolayer	84
27.	Antibody binding to immobilized HA-MPC and HA-SAM	86
28.	Crystal structure of the protective antigen of <i>B. Anthracis</i> and cartoon of corresponding antigen mimic displaying a conformational loop structure	91
29.	Calculation and cartoon suggesting the optimal size of MPC for bidentate place exchange	92
30.	¹ H NMR of free PA680B peptide, pure Tiop-MPC, and peptide presenting MPC, showing successful peptide presentation	108
31.	2D TOCSY NMR of synthetic peptide and corresponding proton 1D spectra ...	108
32.	X-ray crystal structure of the protective antigen of <i>B. anthracis</i> and cartoons of PA mimics highlighting the conformational and linear epitopes	110
33.	¹ H NMR of Ellman's Reagent derivatized free peptide (PA680M), PA680B-MPC, and PA680B-MPC after isolation of ligands only	112
34.	Representative polyelectrolyte, PA680B-MPC, BSA, and antibody 110 binding in phosphate buffer	113

35.	Plot of Δm against [anti-PA 110] for PA protein antigen, PA680B-MPC, PA680M-MPC, and PA680B-MPC in PBS showing saturation of the Immunosensor in all cases.....	115
36.	Control experiments showing relative binding percent for 300 nM 110 antibody to seven different nanocluster systems.....	116
37.	AFM measurements of an HDT SAM on a gold QCM electrode with and without place exchange of Tiop-MPC.....	121
38.	Representative SPR experiment involving chip washing, PA680B-MPC immobilization, and antibody detection.....	120
39.	Plot of [Ab110] versus RU for binding to PA680B-MPC in Biacore SPR instrument.....	121
40.	Percent of mice surviving 72 hr after injection with various concentrations of antigen.....	124
41.	Results of ELISA experiments for immunized mice sera binding to PA protein, HA protein, and PA680B-MPC.....	127
42.	Results of QCM experiments for immunized mice sera binding to PA protein and PA680B-MPC.....	129
43.	Characterization of Au-MPCs and Pt-MPCs via proton NMR, TEM, and TGA.....	137
44.	Absorbance and fluorescence of Au-MPCs, Pt-MPCs, and of a mixture of Au-MPCs and Pt-MPCs.....	138
45.	Idealized cartoon of monolayer-protected clusters, conjugates, and mixtures and their fluorescence when excited at 400 nm or 680 nm.....	140
46.	Characterization of MPC conjugates via proton NMR and TEM.....	141
47.	Fluorescence enhancement after fractionation of coupled nanoparticles using size-exclusion column chromatography.....	143
48.	Decrease in fluorescence upon enzymatic cleavage of the peptide linker in coupled nanoparticles.....	146
49.	EBO/G recognition by immobilized antibody, showing saturation of the immunosensor and estimated detection limit.....	151
50.	Weight measurement of multi-walled carbon nanotubes solutions using a	

	quartz crystal microbalance.....	153
51.	Anti-Ag ScFv antibody binding to a newly formed silver oxide surface shows a larger Δm than oxide formation only, while fluorescence microscopy shows antibody binding as compared to a control	157

LIST OF ABBREVIATIONS

Symbol

Δf	change in frequency, Hz
C_f	Sauerbrey constant, $2f_0^2/A(c_{66}\rho_q)^{1/2}$ sensitivity factor
Δm	change in mass, g
f_0	frequency of crystal in air (unperturbed), Hz
A	area of the QCM electrode
c_{66}	piezoelectrically stiffened quartz elastic constant
ρ_q	quartz mass density
$\Delta\rho$	change in density
$\Delta\eta$	change in viscosity
R_L	loading resistance
η_q	effective quartz viscosity
C_1	motional capacitance of the unperturbed crystal
N	overtone number
Θ	fractional coverage of a surface by a species
$[C]$	concentration of a bulk solution
$[C]_0$	initial concentration, initial concentration of surface immobilized analyte
Θ_∞	fractional coverage at infinite time
ΔG_{ads}	Gibbs free energy of adsorption
R	gas constant, J/(K•mol)
T	temperature, K

k_f forward kinetic rate constant
 k_r reverse kinetic rate constant
 τ^{-1} kinetic time constant, equal to $k_f C + k_r$

CHAPTER I

INTERFACING BIOLOGY AND NANOMATERIALS FOR SENSING APPLICATIONS¹

Introduction

The characterization of functional nanostructures is crucial in determining their efficacy for life sciences. Nanostructure design requires careful consideration of recognition units and material properties, while synthesis can be meticulous, but evaluation and characterization of the system is equally challenging and important. Nanostructure creation can not easily be deemed successful without analytical evaluation. Furthermore, it may not be used to its potential if it is not well defined and well understood. The design and development of analytical tools and techniques for characterization of nanomaterials is, therefore, imperative. A widely-used and effective tool for structure assembly evaluation is the quartz crystal microbalance (QCM). QCM is a sensitive technique based on the propagation of evanescent acoustic waves, which are affected by adsorption processes as well as local changes in density and viscosity of the contact liquid. Real-time analyte adsorption is monitored through simultaneous measurement of the quartz crystal's resonant frequency of oscillation and the damping resistance caused by liquid loading. One of the paramount applications of QCM has been the study of adsorption of biomolecules on functionalized surfaces. It has also been used in a variety of other applications and is particularly suited to the study of nanoscale materials.^{2,3} This chapter will address the importance of interfaces between biology and nanoscale materials and detail the principles and operational aspects of QCM. Examples

of QCM applications to the life sciences, as well as nanoparticle-based chemical, biological, and immunological sensors will then be addressed. Subsequent chapters will detail QCM analysis of several antigenic nanoparticle/antibody interfaces. An initial, proof-of-concept example of a successful interface between glutathione-protected nanoparticles and antibodies and the evaluation of that interface will be described in Chapter II. This was one of the first examples of such an interface and showed that QCM is an effective technique for quantitative analysis. A more complicated and, perhaps, biologically-relevant nanostructure displaying a linear epitope from the hemagglutinin protein of influenza was developed and shown to effectively interface with monoclonal antibodies, as discussed in Chapter III. Antigen mimic design was taken one step further to include secondary structure or local conformation and allowed the conformational epitope mapping of the Protective Antigen of *B. Anthracis*. This antigen mimic was shown to be more antigenic than its linear counterpart and showed some immunogenicity in mouse model studies, as illustrated in Chapter IV. Chapter V describes a different union between biology and nanomaterials, where a protease-labile peptide is used to join Pt and Au nanoparticles, resulting in enhanced near-IR fluorescence. Additional nanostructures and QCM detection strategies and applications are reported in the Appendices.

Interface Between Biology and Nanomaterials

Fundamental advances in chemistry and biology have allowed biotechnology and materials science to develop over the past decades. Biotechnology has attempted to emulate naturally occurring functional assemblies, from the double helix of DNA to the

multi-subunit protein cage, ferritin. On the other hand, material science has taken advantage of chemical methods for the miniaturization of functional devices. The further evolution of these disciplines into the emerging field of bionanotechnology depends on the successful development and evaluation of structurally well-defined interfaces that bridge biology and inorganic materials chemistry. Interdisciplinary collaboration between these fields will allow for improved biological components to generate new materials while advanced materials will be used to ameliorate biological problems.⁴ The design, synthesis, and characterization of readily programmable, structurally well-defined biological interfaces for inorganic materials represent significant challenges for the realization of these goals.

Progress has been made towards the development of such interfaces, though many options have yet to be explored. Some encouraging synthetic attempts have used DNA, semiconductor-binding peptides, genetically-engineered viruses, and silica-precipitating peptides. Specifically, synthetic single-stranded oligonucleotides coordinated to nanoparticles have been shown to self-assemble with the appropriate complement to form higher ordered structures (Figure 1a).⁵ Phage-display libraries have been used in the successful selection of 12-mer peptides that specifically bind to the 100 face of GaAs single crystals (Figure 1b).⁶ Bivalent peptides of this nature could be used in the directed assembly of nanoscale components. Recently, the iron-storage protein ferritin, which contains its own interface between biology and inorganic iron oxide, has been used as inspiration for the design of a genetically-engineered viral cage that has the ability to precipitate nanoclusters. The virus, cowpea chlorotic mottle virus, was engineered with

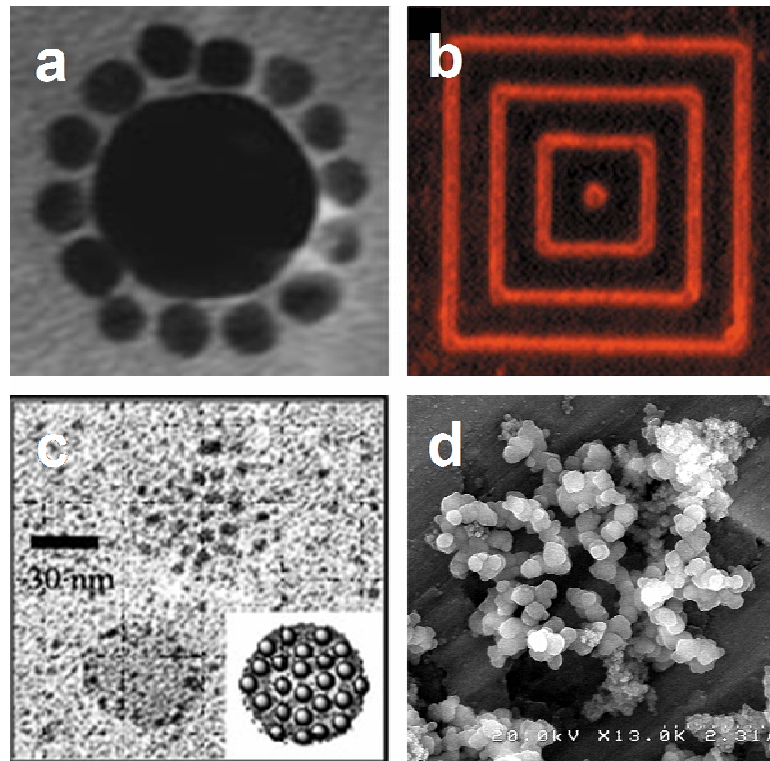


Figure 1. Examples of successful interfaces between biology and inorganic materials. (a) TEM image of 8 nm diameter Au nanoparticles connected to a 31 nm diameter Au nanoparticle through complimentary strands of DNA. (b) Fluorescently labeled antibody bound to peptide presenting phage, which specifically recognized the 100 face of GaAs. (c) TEM image of virus templated synthesis of Au nanoparticle. (d) Electron micrograph of silica particles precipitated via a synthetic peptide.

HRE peptide epitopes on its surface and provided a template for the symmetry directed synthesis of Au nanoparticles (Figure 1c).⁷ Another attempt at interfacing biology and inorganic materials has made use of a synthetic peptide based on silaffin from a variety of eukaryotic algae or diatoms. This peptide was shown to efficiently precipitate silica under mild conditions, mimicking diatom activity (Figure 1d).⁸ These functional materials have enjoyed success in the assembly of nanoscale materials, but have limited application to sensor development. Still, they have succeeded at interfacing biology and

inorganic materials and have served as inspiration for the subsequent design of sensor interfaces.

One biomolecular recognition method that has not been widely employed in the assembly of nanoscale materials is immunomolecular recognition. Immunoglobulin G (IgG) antibodies have affinities (association constant, K_a) on the order of $10^6 - 10^{12} \text{ M}^{-1}$ and have been well-studied for sensor development.⁹⁻¹² Applications of such immunoassays have had a tremendous impact on medical diagnosis and the treatment and understanding of disorders and diseases. Interfacing immunology and nanomaterials will expand these applications and provide potential for improvements on existing assays and treatments. There are several cases where immunology and inorganic materials have been successfully brought together to provide a ground work for further development.

Progress began with the non-specific immobilization of antibody on micron-sized, hydrophobic, latex beads.¹³⁻¹⁵ Antigen binding to immuno-reactive beads causes agglutination, which can be quantified by changes in solution turbidity.¹⁵ Similarly, antibodies have been non-specifically immobilized on 11 nm diameter colloidal gold particles. These particles were used in traditional sandwich immunoassays, where the gold particle provided signal amplification when binding was detected with surface plasmon resonance spectroscopy (SPR).¹⁶ More recently, Nam, et al. created an immunoassay using micron-diameter immuno-magnetic particles in conjunction with 13 nm diameter DNA/antibody derivatized gold clusters. Magnetization allowed for facile separation of agglutinated particle, while double stranded DNA provided an amplification avenue through polymerase chain reaction (PCR).¹⁷ Other strategies have used nanocluster/antibody interfaces as means for multiplexing and amplification.¹⁸⁻²⁰

Another approach made use of a peptide epitope known to bind monoclonal antibody associated with the human malarial parasite, *Plasmodium falciparum*, and was the first example of antigen encapsulated nanoclusters assembling with antibodies through the antibody (paratope)/antigen (epitope) interface.²¹ This important advancement appears to provide a robust, functional nanostructure that has the potential of successfully mimicking a biological entity. Together these interface-dependent techniques have suggested new routes for the study and detection of human IgG, prostate specific antigen, hepatitis B surface antigen, and the human malarial parasite.

Antibodies will continue to be studied as analytical reagents and recognition units in interfacing with nanoscale materials due to their extraordinary binding affinities, ease of use, and relevance to medical disorders. The classic IgG protein has a prototypical Y-shape made up of two heavy and two light chains (Figure 2).

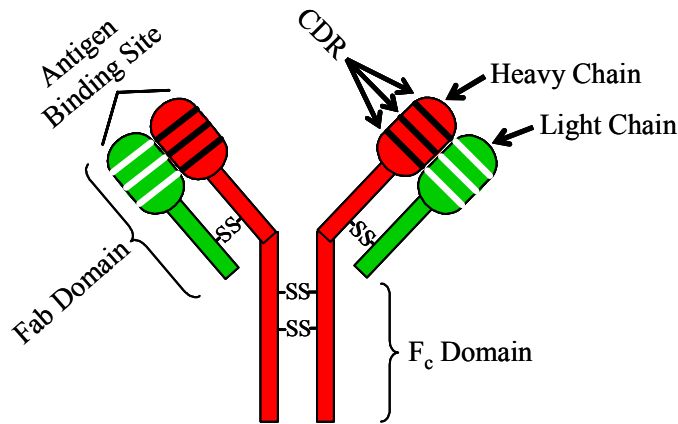


Figure 2. Cartoon structure of a typical IgG antibody, highlighting heavy and light chains joined by disulfides, a constant fragment (Fc), two fragments of antigen binding (Fab), and complementarity determining regions (CDR).

The antigen binding site (paratope), within the Fab (fragment of antigen binding), is formed by the three dimensional arrangement of the complementarity determining regions (CDR). In antibodies, this is the key region of immunorecognition and results in the proteins valency. Three major types of antibody preparations are in use for immunoassays: polyclonal, monoclonal, and single chain fragment variable (ScFv). Polyclonal antibodies (pAb) are generally collected from animals and result as a response to the injection of an antigen. They are produced by many different B lymphocytes and recognize different epitopes within the same antigen, resulting in a mixture of antibodies, with only a subset of total IgG recognizing the epitope of interest. Monoclonal antibodies (mAb), on the other hand, are produced in a colony of identical B cells. Each antibody binds to the same epitope and the mAb sample is homogeneous.⁹ Single chain fragment variable (ScFv) antibodies represent the smallest functional domain of a traditional monoclonal or polyclonal antibody as they consist of one linked Fab domain (Figure 3).^{22, 23}

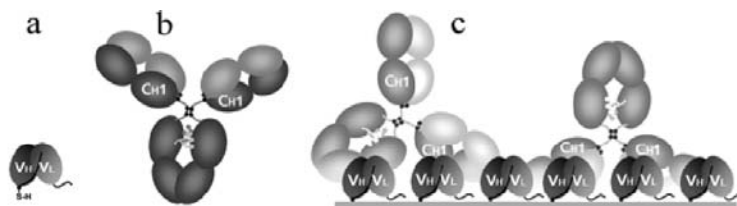


Figure 3. (a) Single-Chain Fragment Variable recombinant antibody with cysteine incorporated into linker, (b) Rabbit IgG, (c) Interaction between immobilized ScFv and rabbit IgG.

Phage-display recombinant antibody technology has produced high-quality, antigen-specific ScFv antibodies with affinities (binding strengths) comparable or greater than

those of traditional antibodies.⁶ This technique and these antibodies are particularly useful for antigens that are poorly immunogenic, readily degrade, or for which monoclonal or polyclonal antibodies are difficult to obtain. These three types of antibodies provide a range of options for interfacing immunology with nanoscale materials.

The interface between biology and inorganic materials has manifested in many different forms, covering the range of biological systems and the range of inorganic materials. Immunology has interfaced with many substrates, including two-dimensional surfaces,²³⁻²⁵ organic polymers,^{13, 15, 17} large metal particles,^{16, 21} semiconductor quantum dots,²⁶ and small, ligand-capped metal cores.² The interface of antibodies with each of these substrates has produced interesting functional materials, though ligand-capped noble-metal clusters (monolayer-protected clusters, MPC) have recently received attention for their unique consolidation of self-assembly techniques and metal nanoparticle chemistry.²⁷⁻²⁹ Furthermore, their chemical, electronic, and physical properties, a lack of air and water sensitivity, and convenient characterization make them robust materials.^{21, 30-33} Programmed specificity through the introduction of biologically relevant molecules is one of their most promising features and lends to the development of an immuno-interface.^{34, 35}

Synthesis and assembly of MPCs can occur through several routes, using various metals (Au, Ag, Cu, Pt, CdS, ZnS, Ag₂S),³⁶ reductants (citrate, Na₂S, NaBH₄), and capping ligands (thiolate, disulfide, amine, imidazole, carboxylic acid, phosphine, iodine). Surfactants, templates, and physical methods (photochemistry, sonochemistry, radiolysis, thermolysis) have also been employed.³⁷ Conventional methods have

primarily been based on the Brust-Schiffrin Method, published in 1994.³⁸ This was originally a two-phase synthesis with stabilization by organic soluble thiolates and reduction by NaBH₄ (Figure 4a).

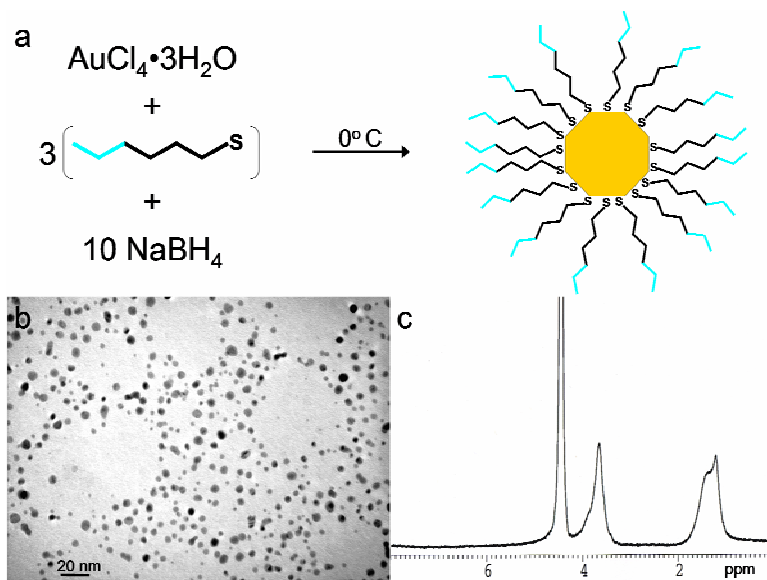
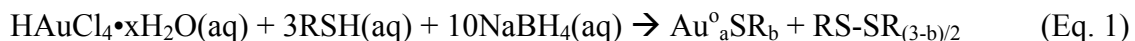


Figure 4. Representative synthesis and characterization for a tiopronin-protected cluster. (a) Synthesis conditions based on a modified Brust method and cartoon schematic of a monolayer protected cluster. MPC ligands are connected through thiolate moieties at one end and generally have a functional group at the opposing end (turquoise). (b) TEM image of MPC showing spherical shape, size, and size dispersity. (c) ¹H NMR of tiopronin MPC showing broad -CH₃ (~1 ppm) and -CH₂-/-CH- (~3.5 ppm) peaks. The water peak is at 4.8 ppm.

This method was subsequently adjusted for the synthesis of water-soluble MPCs, which is generally a one-phase synthesis and follows the simple equation below (Eq. 1).³¹



Templeton, et al. reported the synthesis of water-soluble tiopronin (N-(2-mercaptopropionyl)glycine) MPCs with a 1.8 ± 0.7 nm diameter according to this method. Characterization of these nanoclusters follows from traditional materials techniques, as previously described in depth.^{28, 31, 39} Examples of a transmission electron microscopy (TEM) image and proton nuclear magnetic resonance spectroscopy (¹H NMR) spectrum are available in Figures 4b and 4c. A more complete review of gold nanoparticle synthesis, characterization, and applications was recently published by Daniel et al.³⁷

One of the most promising features of MPCs is their ability to exchange thiolate ligands with ligands in solution. This allows for the specific introduction of biologically active molecules, programmable specificity, and the synthesis of functional nanoclusters. In this way, nanoscale inorganic materials make potentially interesting solid supports for the immobilization and presentation of antibody or antigen, leading to a successful interface with an immunological system. Place exchange of free thiol onto three-dimensional MPCs is a relatively facile process that is regulated by solvent, reaction temperature, reaction time, and properties and concentration of original and replacement thiol.³⁴ Investigation of the dynamics, kinetics, and mechanism of place exchange are abundant and generally support an associative, S_N2 mechanism.^{34, 35, 40, 41} Place exchange on MPCs has been compared to preceding studies of place exchange on two-dimensional self-assembled monolayers.^{42, 43} Exchange is more likely to occur on 3D surfaces (MPCs) over 2D surfaces (SAMs) due to the higher propensity for defect sites in structures with a substantial radius of curvature.³⁴ Another important feature of place exchange reactions is the idea that fast-exchange sites are not static. Evidence for this

has come from the exchange of several different ligands onto the same MPC^{28, 35} and from an inability to completely remove ligand that had been previously exchanged on a cluster.^{34, 35} A significant implication of these results is the ability of a thiolate to migrate across the monolayer of an MPC and position itself for an optimal interface.

There are many examples of successful place exchange and coupling reactions with organic and water soluble MPCs, resulting in functional nanostructures. For example, Templeton et al³⁵ used traditional amide coupling techniques to attach 12 different functional ligands to nanoclusters, introducing spin labels, amino acids, fluorophores, sugars, and electroactive moieties. Place exchange has also introduced fluorescein and an electroactive viologen species. Electrochemical quartz crystal microbalance of this MPC showed redox activity of the viologen as well as deposition of the MPC upon viologen reduction.⁴⁴ Antimicrobial nanoclusters have been prepared by functionalization with vancomycin,⁴⁵ glutathione-protected nanoclusters have been shown to interact with the enzyme glutathione transferase,⁴⁶ and biotinylated nanoclusters bind to streptavidin.⁴⁶ This type of MPC functionalization produces nanostructures with specific activity and suggests potential for further nanocluster modulation in the design of bioreactive materials.

There are two ways that functional nanoclusters can interface with immunology through paratope/epitope recognition: an antibody can be covalently attached to an MPC or an MPC can play the role of the antigen (Figure 5). Antibody/nanocluster complexes have been previously studied as mentioned above. Briefly, immunoassays for human IgG have been developed using antibody bound latex beads,^{14, 15} signal amplification was observed with antibody bound gold nanoclusters in SPR immunoassays,¹⁶ and antibody

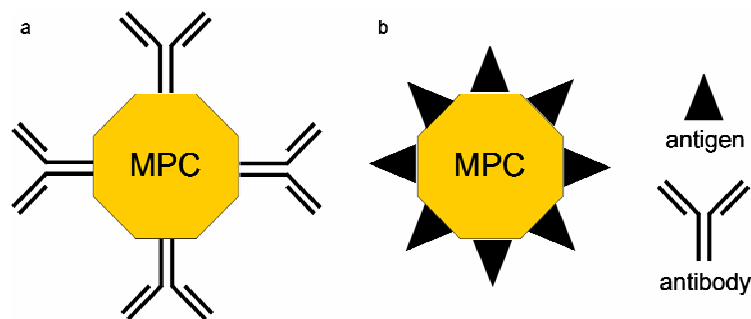


Figure 5. Cartoon schematic of (a) nanocluster presenting antibody (antibody mimic) and of (b) nanocluster presenting antigen (antigen mimic). Epitope antigens are generally smaller than antibodies and can be presented at a higher areal density than antibodies.

bound magnetic microparticles have been used as capture agents.¹⁷ There is further interest in using nanoparticle labeled antibodies as nanoprobes for imaging.⁴⁷

An alternate approach would be to attach an antigen to an MPC or functionalize an MPC with a peptide epitope (Figure 5b). An epitope is the antigenic determinant of a protein and corresponds to the region of the protein that is specifically recognized by the antibody.⁴⁸ Accordingly, epitopes are only defined in an operational or functional sense: anything that is bound by an antibody is, by definition, an epitope. Therefore, epitope regions from proteins have been synthesized and expressed as smaller functional units and have been shown to bind antibodies. Examples of these would be the FLAG or E tags commonly used in protein expression.^{23, 25}

Motivation for the design of antigen mimics is widespread in the realm of biology, medicine, and materials research (Figure 6). The medical field and population health could improve through the establishment of antigen-functionalized nanoclusters, or antigen mimics, that act as effective, inexpensive, non-toxic vaccines for bacterial, viral, and toxin-related diseases, such as anthrax, ebola, respiratory syncytial virus, and small pox.

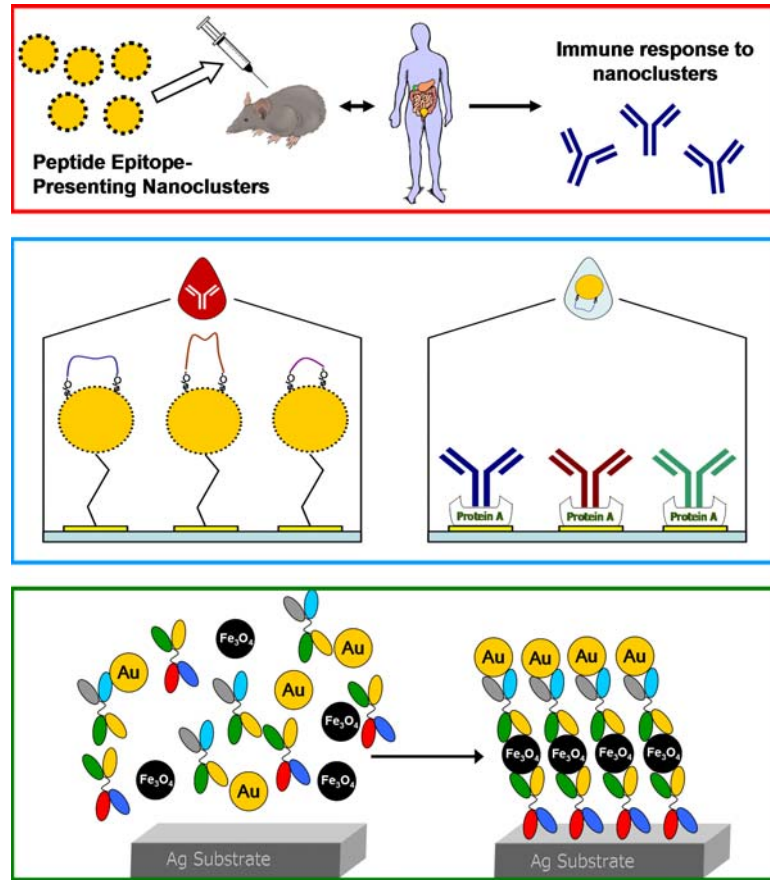


Figure 6. Possible applications for immuno-functionalized nanoclusters. (top) Non-toxic vaccines for bacterial, viral, toxin-related disease; (middle) Nanocluster array for medical diagnosis or antigen mimics for sensor calibration; (bottom) Assembly of nanoscale architectures.

Diagnostic techniques could also benefit from using antigen mimics to confirm immunity or identify disease. Field sensors could be regularly tested using non-toxic antigen mimics as positive controls. In a very different area, engineering feats could be performed using high-affinity interfaces to build nanoscale architectures. These benefits are far-reaching future goals, but provide motivation for antigen mimic design.

The current approach to this type of antigen mimetics is to synthesize the linear epitope and rely on primary structure (amino acid sequence) to provide specificity. Combining this type of mimetics with nanoscale materials produced the first example of

antigen encapsulated nanoclusters assembling with antibodies through the paratope/epitope interface. A linear peptide epitope known to bind monoclonal antibodies associated with the human malarial parasite, *P. falciparum*, was used in the assembly of a robust, functional nanostructure that successfully mimicked a biological entity.²¹ A more recent example used glutathione-protected nanoclusters and polyclonal anti-glutathione antibodies. This approach confirmed the ability to assemble epitope-protected nanoclusters with antibodies and provided quantitative binding information through improved analytical techniques.²

These two examples used nanoclusters with peptide epitopes completely covering their surface and were synthesized with large amounts of ligand, rather than specifically functionalized with small amounts of peptide. The next step in antigen mimic design is to functionalize pre-existing nanoclusters through place exchange reactions described above. This type of assembly provides a more complex nanostructure with three or more components and allowed for the use of more complicated linear and conformational epitopes. In a recent study a linear peptide epitope, from the hemagglutinin (HA) protein related to influenza, was synthesized and specifically presented at a controlled density on the surface of a pre-existing tiopronin-protected cluster.⁴⁹ This mimic of the HA protein was shown to interface with monoclonal anti-HA antibodies and was compared to a self-assembled monolayer of the same peptide epitope.

Linear peptide epitopes used in the malaria, glutathione, and HA examples rely on primary amino acid sequence to provide antigenicity and specificity. This does not take into account the complex secondary structure (local conformation) exhibited by native proteins, which is essential to antibody recognition. Cyclization of peptides to

approximate a loop structure has been used to introduce epitope conformation,⁵⁰ but the development and presentation of a peptide epitope that reconstitutes a physiological conformation is an interesting alternative. This was recently achieved through the bidentate presentation of a peptide epitope from a loop region of the protective antigen (PA) of *B. anthracis*.⁵¹ The conformational antigen mimic was able to interface with monoclonal anti-PA antibodies and showed enhanced affinity over a linear antigen mimic.

This variety of antigen mimics using small molecule, linear, and conformational epitopes suggests multiple routes to interfacing inorganic nanoclusters with biological antibodies. Many other options are also available and, together, supply a “toolbox” of interfaces that can be used and studied in a multitude of systems. The three cases of GSH-MPC, HA-MPC, and PA-MPC are detailed in Chapters II, III, and IV, respectively.

Principles and Operation of QCM

The quartz crystal microbalance relies on the converse-piezoelectric effect, reported by the Curie brothers in 1880. Piezoelectricity describes the electrical charge produced by pressure applied to solids having certain geometries, while the converse effect produces a strain on the crystal when an electric field is applied.⁵² Coupling the crystal to an oscillating circuit provides crystal oscillation at a resonant frequency (Figure 7). These quartz resonators have been widely used in communication devices, commercial acoustic electronics, and sonar.^{52, 53} Sauerbrey first demonstrated the usefulness of this effect for analytical chemistry by showing a linear relationship between mass deposited on the crystal and the frequency of oscillation (Eq. 2).^{2, 52}

$$\Delta f = -C_f \Delta m \quad (\text{Eq. 2})$$

Initially, QCM was used in the gas phase, where oscillator resistance is low and mass adsorption is rigid. The device was improved in 1982 by the advent of circuitry capable of crystal operation in liquids.

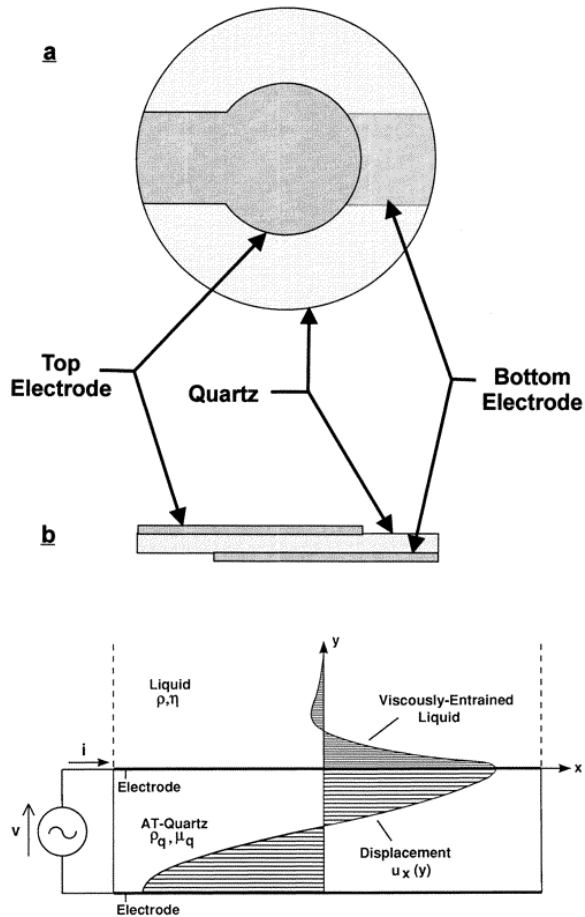


Figure 7. Top and side view of a QCM resonator (top) and cross sectional view of a QCM resonator in contact with a liquid (bottom). Wave propagation is relatively loss-less in the piezoelectric material, but becomes evanescent in the viscous liquid.

While this advancement introduced QCM to the world of bioanalytical chemistry, it also introduced new challenges. The first is that operation in liquid slows the mass transport of analyte to the sensor surface. The second is that many binding events in liquid, especially those biological in nature, are not static, but tend to be in equilibrium. The third is resonator damping and viscous loading (Figure 7).⁵⁴ It has been shown that the density and viscosity of the contact solution affects crystal frequency response, convolutes mass measurements, and requires modification of the Sauerbrey equation (Eq. 2).^{52, 55} Careful consideration of simultaneous mass and liquid loading by Kanazawa⁵⁶ and Martin⁵⁷ has shown that Δf relates to adsorbed mass and the density and viscosity of the contact liquid, according to the following equation (Eq. 3):⁵⁷

$$\Delta f \simeq C_f \Delta m - C_f (\Delta \rho \eta / 4 \pi f_o)^{1/2} \quad (\text{Eq. 3})$$

It is, therefore, impossible to distinguish mass loading from liquid loading by frequency measurements alone. Fortunately, the independent term of liquid loading resistance, R_L , depends solely on density and viscosity (Eq. 4):⁵⁷

$$\Delta R_L \simeq (\eta_q / [c_{66} C_1]) + (N \pi C_1)^{-1} (\Delta \rho \eta / \pi f_o c_{66} \rho_q)^{1/2} \quad (\text{Eq. 4})$$

Measuring both changes in frequency and resistance provide a means for decoupling mass and liquid loading effects, though different methods have been described.^{2, 52, 54, 56-59} Applying the above equations (Eq. 3 and 4) to frequency and resistance measurements to reliably calculate adsorbed mass has proven to be non-trivial. A simple approach to a

reliable mass measurement has been to create a calibration curve of change in frequency as a function of change in resistance for a system in which mass loading is minimal. In one case, sucrose, a hydrophilic molecule that will not independently adsorb to the QCM electrode, was dissolved in DI water at 0, 5, 10, 20, and 40% by weight. Sequential addition of these five solutions to the QCM sensor provided simultaneous changes in frequency and resistance that were due to density and viscosity effects only (Chapter II, Figure 11).² The relationship between frequency and resistance within this range is linear and provides an accurate calibration. Above approximately 40% sucrose, the relationship deviates from linearity, making this approach only applicable to systems in which the resistance changes by less than 500 Ω .^{56, 60} Problems also occur with this calibration, as in any QCM measurement, when coupling to the sensor is non-rigid and the analyte has its own viscous properties. Calibration allows for the calculation of Δm through simultaneously solving equations 3 and 4 and using a sensitivity factor, C_f , of 56.6 $\text{Hz}\cdot\text{cm}^2\cdot\mu\text{g}^{-1}$, which is known for a 5 MHz crystal.⁶¹ Decreasing the crystal thickness increases the resonant frequency and can provide enhanced sensitivity.

Since his study of simultaneous QCM mass and liquid loading in 1991,⁵⁷ Stephen Martin from Sandia National Laboratory and collaborators at Leicester University have continued to contribute experimental and theoretical-based insight into the details of QCM measurement in liquids. Four contributions, since 1997, have covered resonator response to liquid loading,⁵⁴ the modeling of resonator response under loading conditions,⁶² the modeling of viscoelastic film response,⁶³ and a model for wetting characteristics of roughened surfaces.⁶⁴ This collective work has provided a better

understanding of loading responses in QCM and has supported more rigorous evaluation of important systems.

Another area of QCM sensor development has been in the area of multi-channel QCM. Using arrays of resonators or micro-fluidics to partition individual resonators could provide the simultaneous measurements needed for multi-analyte detection strategies. A significant challenge in multi-channel QCM is the isolation of each electrode. Circuit shorting or resonance overlap from electrode to electrode could cause considerable problems. Two approaches to this problem have made use of electrode miniaturization⁶⁵ and the restriction of oscillation to indented areas surrounded by thicker quartz.⁶⁶ Both of these approaches have had success in the construction of a multi-channel QCM instrument.

QCM has been shown to work well with 3D substrates and multilayer adsorptions often encountered in materials applications.² QCM acoustic shear waves are evanescent and decay exponentially in the contact liquid, causing a loss of sensitivity at distances from the sensor surface (Figure 7). Mass that is rigidly coupled to the sensor propagates the wave without loss, where viscous material causes immediate wave decay.⁵⁸ The depth at which these waves penetrate the contact liquid affects instrument sensitivity. QCM, at 5 MHz, has a calculated penetration depth of 250 nm,⁵² with a total decay length of 1 μm ,⁵⁸ though experiments have shown no loss of sensitivity for layers as large as 400 nm.^{2, 58, 67, 68} In comparison, surface plasmon resonance spectroscopy (SPR) has a calculated penetration depth of only 150 nm and has shown significant peak broadening with layers less than 200 nm.^{69, 70} Examples of peak broadening in SPR come from the use of metal nanoclusters for signal amplification.^{16, 71, 72} It was shown that antibody-

presenting gold nanoclusters binding to immobilized anti-IgG increased the SPR shift as compared to free antibody.^{16, 71} This also caused broadening of the SPR curve, which increased in width as the density or diameter of the colloidal gold was increased.⁷² QCM has not suffered from this sensitivity loss, even at extensive adsorption.²

A challenge in QCM, and in many biosensors, is sensor functionalization for improved specificity. While the gold QCM electrode imparts almost no specificity of its own, it provides a substrate for a variety of functionalizations. The gold electrode is amenable to hydrophobic interactions, is well-suited for self-assembled monolayer (SAM) formation, and enables electrochemical surface reactions. Approaches to improve specificity in QCM have used SAMs,^{24, 43, 73} ionic interactions,⁷⁴⁻⁷⁷ electrochemical deposition,^{44, 78} and protein adsorption (Figure 8).⁷⁹⁻⁸¹ These methods allow for the immobilization of a variety of biological species and nanostructures and permit a variety of detection schemes. SAMs have been studied extensively^{42, 73, 82} and feature a defined orientation, high areal density, and programmability in the exposed head-group. They have recently been used for the covalent immobilization of oligosaccharides²⁴ and peptide epitopes.²⁵

Ionic layering, using polyelectrolyte⁷⁵⁻⁷⁷ or SAMs with ionic head-groups,⁷⁴ has allowed for effective immobilization and orientation of a variety of nanoparticles. Though the interaction is generally non-specific, relying on electrostatic and van der Waals interactions, layer-by-layer growth is highly tunable according to concentration, ionic strength, and pH. This promotes high affinity binding, reversibility, and high packing density, and has been used for single layer deposition and multilayer nanorainbow assembly.^{75, 77}

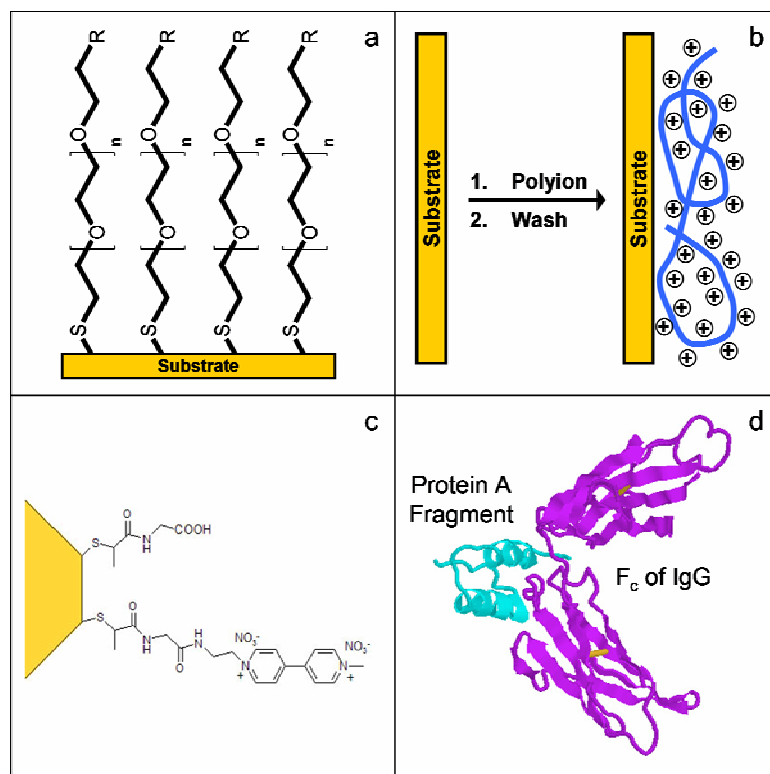


Figure 8. Examples of QCM functionalization techniques to impart specificity. (a) Self-assembled monolayers immobilize ligands in a high density and often use polyethyleneglycol spacers. (b) Polyelectrolyte provides a thin layer of charge (positive or negative) for ionic interactions. (c) Viologen functionalized electroactive nanoclusters can be electrochemically deposited on the QCM surface. (d) X-ray crystal structure of a Protein A fragment commonly used in the immobilization of antibody.

Electrode functionalization and nanoparticle immobilization has also been pursued with electrochemical deposition, using electrochemical quartz crystal microbalance (EQCM). Viologens, such as N-(methyl)-N'-(ethylamine)-viologen dinitrate (MEAV), have been previously studied⁷⁸ as electroactive species and are known to adhere to electrodes upon reversible reduction of the [viologen]^{2+/1+} couple. Attachment of MEAV to nanoclusters allows similar adhesion to electrodes, thereby immobilizing the nanocluster on the QCM surface.⁴⁴

Another route employs Protein A for immobilization of antibodies in an accommodating conformation. Protein A is a cell wall protein that forms stable complexes with gold through van der Waal interactions ($K_a \sim 10^8 \text{ M}^{-1}$)⁷⁹ and contains five tandem domains that bind the Fc region of IgG with high affinity and selectivity. These properties optimize the presentation of antibodies such that both antigen binding regions (Fab) are unobstructed (see also Figures 2 and 3).⁷⁹⁻⁸¹

Another advantage of QCM would be the ability to make time-resolved measurements, which allows the derivation of equilibrium binding constants and kinetic rate constants. These constants provide valuable information concerning the affinity or avidity of one material for another, the rate at which they interact, and the interaction order. A molecule's affinity is defined through the equilibrium association constant (K_a) for the interaction and is generally valid for monovalent, one-to-one interactions. Avidity is related to the same equilibrium process (K_v), but describes multivalent processes. For example, at low ligand concentrations a multivalent ligand could bind to several monovalent receptors, increasing the affinity of the ligand for the receptor. There are also cases of multivalent receptors with monovalent ligands as well as multivalent receptors with multivalent ligands.⁸³ The complexity of these interactions can be daunting, especially for molecules like lectins that are designed for increased affinity through multivalency. The simplest case would be the interaction of a monovalent ligand (an antigen, for example) with a monovalent receptor (a ScFv antibody, for example): $\text{Ag} + \text{Ab} \leftrightarrow \text{Ag-Ab}$. The elementary equilibrium expression for the formation of the complex is (Eq. 5),

$$K_a = [Ag-Ab]/([Ab][Ag]) \quad (\text{Eq. 5})$$

K_a is the equilibrium association constant and is generally in the range of 10^6 to 10^{12} M^{-1} for monoclonal antibody interactions, indicating a large equilibrium shift to product formation when antigen is in the presence of antibody. If this association and equilibrium shift occurs at a surface, where the first component adsorbs to the surface-supported second component, the equilibrium expression can be rearranged to an adsorption isotherm. The adsorption isotherm represents the connection between the amount of substance adsorbed, the concentration of the bulk solution, and the equilibrium constant, K_a . The Langmuir isotherm is commonly used and relies on three important assumptions: (1) there is no lateral interaction between adsorbed species; (2) the surface is homogeneous; (3) the maximum adsorption is saturation to a monolayer. Adsorption isotherms are sometimes written in terms of fractional coverage (Θ) or percent of monolayer formation. A generalized Langmuir isotherm in this form is (Eq. 6),

$$\Theta/(1-\Theta) = K_a C \quad (\text{Eq. 6})$$

In the case of QCM studies, the fractional coverage is related to the change in mass (Δm) and the initial concentration of surface immobilized antibody is related to the maximum change in mass (Δm_m). Rearranging to solve for Δm provides a commonly used form of the Langmuir isotherm (Eq. 7),

$$\Delta m = \Delta m_m (K_a C / (1 + K_a C)) \quad (\text{Eq. 7})$$

Plotting Δm as a function of bulk concentration (C) shows a steep increase in adsorption that levels off with increasing concentration as a complete monolayer is achieved (see Chapter II, Figure 16). This line can be fit to non-linear regressions, but does not provide a simple means for extracting the equilibrium constant. Instead a reciprocal plot can be used to obtain a straight line fit. There is more than one way to obtain a reciprocal plot by rearranging the Langmuir isotherm (Eq. 7). Two options are (Eq. 8) and (Eq. 9),

$$\Delta m = -(K_a)^{-1}(\Delta m/C) + \Delta m_m \quad (\text{Eq. 8})$$

$$C/\Delta m = (\Delta m_m)^{-1}(C) + (\Delta m_m K_a)^{-1} \quad (\text{Eq. 9})$$

In (Eq. 8) Δm is plotted against $\Delta m/C$ and the inverse of the slope provides the K_a . In (Eq. 9) $C/\Delta m$ is plotted versus C and the K_a must be extracted from a combination of the slope and y-intercept. Both techniques have been used in literature and provide reliable K_a values.^{2, 24, 84-86} Once the equilibrium association constant is known, it can be used to calculate both the fractional coverage at an infinite time point (Θ_∞ , Eq. 10) and the Gibbs free energy of adsorption (ΔG_{ads} , Eq. 11),

$$\Theta_\infty = C/(C + K_a^{-1}) \quad (\text{Eq. 10})$$

$$\Delta G_{\text{ads}} = -RT \ln K_a \quad (\text{Eq. 11})$$

This method offers a simple way to determine equilibrium constants for systems that generally follow the assumptions outlined for a Langmuir isotherm, though variations on the Langmuir isotherm can account for more complex systems.⁸⁷

Equilibrium association constants for antibody/antigen interactions can be determined with different techniques, not necessarily involving real-time measurements. Kinetic information, on the other hand, requires time-resolved information. The rate at which an interaction takes place can be valuable in evaluating component efficacy. The time course for monolayer formation is given by (Eq. 12),

$$\Theta(t) = [C/(C+K_a^{-1})][1-\exp(-(k_f C+k_r)t)] \quad (\text{Eq. 12})$$

According to (Eq. 10) Θ_∞ can be substituted in and the exponent can be simplified by calling $(k_f C+k_r)$ equal to the time constant, τ^{-1} , (Eq. 13),

$$\Theta(t) = \Theta_\infty[1-\exp(-\tau^{-1}t)] \quad (\text{Eq. 13})$$

For a given concentration of the bulk solution (C), $\Theta(t)$ is related to Δm at a particular time and Θ_∞ is related to the maximum change in mass (Δm_m , Eq. 14),

$$\Delta m_t = \Delta m_m[1-\exp(-\tau^{-1}t)] \quad (\text{Eq. 14})$$

Fitting (Eq. 14) to each time point in the real-time adsorption binding curve yields the time constant. Knowing the concentration of the bulk solution allows the extraction of forward (k_f) and reverse (k_r) rate constants. The ratio of these kinetic constants is equal to the equilibrium constant ($K_a = k_f/k_r$) and can be used for comparison with isotherm methods.

QCM Applications to Life Sciences

The benefits of QCM and detailed functionalization strategies have allowed the study of many biological and chemical systems.^{52, 88} An early and notable example of a chemical study, is the direct kinetic measurements of thiolate molecules self-assembling on two-dimensional gold surfaces.⁸² This helped provide a foundation for QCM kinetic studies and was quickly followed by a kinetic study of anti-fluorescein antibody binding to fluorescein lipids in Langmuir-Blodgett films.⁸⁵ The fluorescein hapten was coupled to lipids and mixed with unfunctionalized lipids to form a bilayer with approximately 5% fluorescein lipid. Through QCM measurements, monoclonal antibody was found to have an affinity (K_a) in the range of $10^7 - 10^8 \text{ M}^{-1}$ and forward and reverse rate of reaction constants of approximately $2 \times 10^5 \text{ M}^{-1}\text{s}^{-1}$ and $2 \times 10^{-3} \text{ s}^{-1}$, respectively.

More recently, Zeng, et al. conducted two immunoassay experiments using QCM.^{23, 24} The first was a study of α -Gal carbohydrate antigen as anti-Gal antibodies are of interest for therapeutics in xenotransplantation. Thiolated trisaccharides were immobilized on the surface of the QCM through the formation of a self-assembled monolayer and exposed to polyclonal anti-Gal antibodies, a lectin from *Griffonia simplicifolia*, and a lectin from *Marasmius oreades*. The antibody displayed the strongest binding, with a dissociation constant (K_d) three orders of magnitude greater than either of the lectins. They concluded that this QCM approach is competitive with established label-free techniques.²⁴ The second immunoassay made use of single-chain fragment variable (ScFv) antibodies to increase the surface density of antigen binding sites (Figure 3). The recombinant antibodies were genetically engineered to contain a linker arm and cysteine residue to ensure self-assembly in a defined orientation. Considering their size (27 kDa)

and ease of engineering, they have a considerable advantage over Fab fragments or full-sized IgG for the detection of antigen. The ScFv antibodies were initially expressed and evaluated using SDS-PAGE and Western Blot Analysis. After immobilization on the QCM gold electrode, the monolayer assembly was verified electrochemically with cyclic voltammetry and electrochemical impedance. This confirmed surface coverage, but provided no information on antibody orientation. The ScFv rabbit anti-IgG antibody was successful in detecting rabbit IgG down to 1.1 nM, which is more than 7 times lower than that detected with an anti-IgG Fab fragment sensor. Another benefit of this system is the reversibility of IgG binding coupled with the stability of the ScFv monolayer to allow regeneration and reusability of the sensor.²³

A piezoelectric immunosensor has also been developed for the detection of aerosolized SARS-associated coronavirus (Figure 9a).⁸⁹ Since the introduction of circuitry able to operate QCM in liquids, gas phase measurements have primarily been used in metal vapor deposition techniques, rather than biological studies. A functionalized QCM crystal could be used as a biological “nose” for the detection of aerosolized agents, such a coronavirus. In this example, polyclonal anti-SARS-CoV was presented on the gold QCM electrode through a specific Protein A intermediate. Antigen powder was then reconstituted in the saliva of a healthy volunteer and aerosolized in the presence of the sensor. The antigen bound quickly to the antibody and was detected at concentrations down to 0.60 mg/mL.

Many other interesting and pertinent biological systems have been studied, including the use of glycosphingolipids for detection of ricin,⁹⁰ the use of high resonant frequency

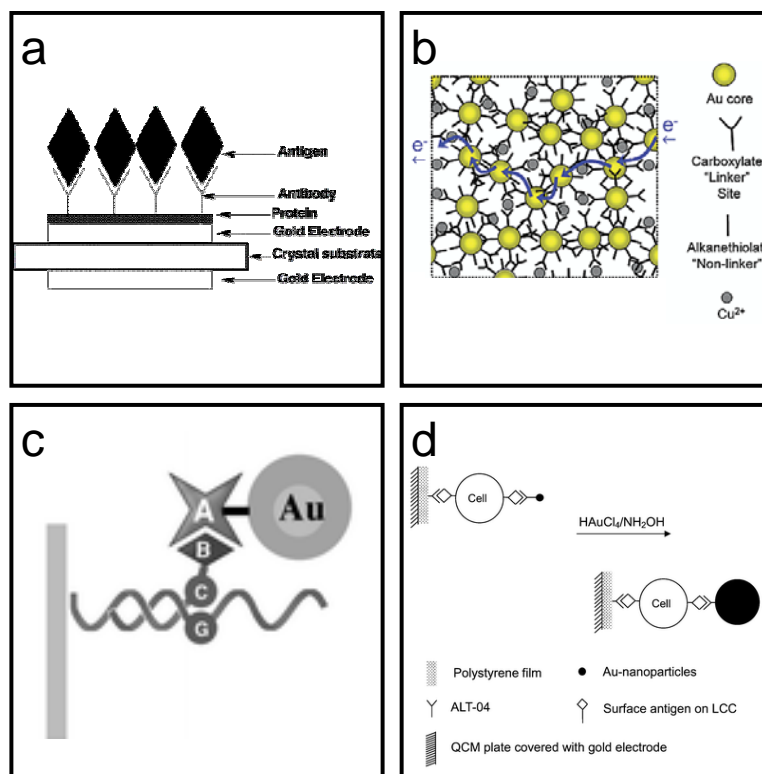


Figure 9. Representative QCM-based sensors for chemical, biological, and immunological applications. (a) QCM immunosensor for aerosolized SARS-associated coronavirus; (b) EQCM chemical sensor using change in electron flow through nanoparticle films; (c) QCM DNA base mismatch detection using gold nanoparticle growth for signal amplification; (d) QCM immuno-detection of lung carcinoma cells and gold nanoparticle growth for signal amplification.

quartz crystals (39 to 110 MHz) for the detection of phages,⁹¹ and the study of annexin A1 binding to solid-support membranes.⁹² A complete review of QCM applications to the life sciences is not the scope of this chapter, though other sources can be consulted for further examples.^{52, 88}

QCM Nanoparticle-based Chemical Sensors

The evaluation of interfaces between biology and nanotechnology has been an area of recent research interest, but originally started through the early development of chemical

sensors. Originally, QCM was designed for gas phase measurements and has been used in the control of metal vapor deposition. QCM continues to be used for gas phase measurements, but has employed polymer and nanoparticle films for organic vapor sensing.⁹³⁻⁹⁵ In 2001, dodecanethiol MPCs of 2 and 5 nm diameter were covalently assembled on a QCM substrate through dithiol linkages or non-covalently through carboxylic acid hydrogen bonding.⁹³ The nanoparticle thin-layers were then studied for their ability to partition toluene, hexane, methanol, ethanol, and water vapors. Vapor sorption was detected by simultaneous monitoring of frequency and resistance. Results suggested the viability of nanostructure films for vapor sensing and highlighted similarities and differences between the size of MPC used and the assembly technique.

Shortly thereafter, Zamborini, et al used electrochemical QCM to simultaneously measure conductivity and vapor partitioning in MPC films (Figure 9b).⁹⁴ This approach used small (1.6 nm diameter) nanoclusters with mixed monolayers of alkanethiolate and ω -carboxyalkanethiolate. The free carboxylic acid was used in conjunction with Cu^{2+} ions to assemble a network polymer of carboxylate- Cu^{2+} -carboxylate bridges. These ion bridges allowed for electron transport through the polymer, while film swelling due to vapor partitioning (ethanol or dichloromethane) diminished electron flow.

Another example⁹⁵ made use of a greater variety of nanoclusters, protected with dodecanethiol, benzenethiol, 4-chlorobenzenethiol, 4-bromobenzenethiol, 4-(trifluoromethyl)benzenethiol, 4-hydroxybenzenethiol, and 4-aminobenzenethiol. Nanoparticle films were spray coated onto a QCM substrate and monitored by QCM to a final change in frequency of $\sim 10,000$ Hz. It was important to deposit a film with a thickness large enough to partition vapor, but small enough to rigidly couple the entire

film to the sensor, maintaining an accurate sorption response. Motional resistance was monitored during film deposition to ensure rigidity as resistance is related to film viscoelastic properties. Results implied that different nanocluster films had increased sensitivity for different vapors (hexane, toluene, butanone, and butanol) and compared with vapor partitioning into organic polymers.

QCM Nanoparticle-based Biosensors

Inspired by the success of QCM bioassays and bionanotechnology, researchers have developed nanoparticle-based detection schemes using QCM for improved sensitivity. A popular area of analytical biochemistry involves the detection of DNA for a range of applications from gene analysis to forensic applications, where low detection limits are required. Willner, et al. have developed three different amplification paths for the detection of single-base mismatches in DNA with QCM detection (Figure 9c).⁹⁶⁻⁹⁸ Each path begins with the immobilization of ssDNA (25 bases) through SAM technology. Its complementary strand with an extra 16 bases is then introduced and allowed to base pair. In some cases a complement DNA strand with a single base-pair mismatch is purposely assembled. This allows for a single nucleotide, coupled with biotin, to bind at the mismatch site. At this point, three different approaches can be used: (1) free avidin can bind to the base-pair biotin, followed by biotin-labeled liposome binding; (2) avidin-labeled nanocluster can bind, followed by controlled nanoparticle growth for amplification; (3) avidin-labeled alkaline phosphatase can bind and catalyze the precipitation of an insoluble organic product for amplification. These methods lead to mismatch detection with detection limits ranging from 10^{-12} – 10^{-16} M. The QCM

gravimetric technique is well-suited for these types of precipitation/amplification schemes.

A similar approach to DNA hybridization detection and amplification also uses avidin-labeled alkaline phosphatase (as above).⁹⁹ In this case, the enzyme catalyzes the production of the reducing agent, p-aminophenol, from a p-aminophenyl phosphate precursor. The reducing agent reduces Ag^+ ions in solution, which biomineralize into Ag nanoparticles on the DNA strand or on the QCM sensor surface, causing QCM signal amplification. The deposited silver can then be used in anodic stripping voltammetry to further confirm DNA binding, down to 100 aM concentrations.

QCM Nanoparticle-based Immunosensors

The design, synthesis, and assembly of functional nanostructures are important challenges in the interface with immunology. Finding key recognition units and presenting them in the appropriate environment and conformation are crucial to programming material specificity and affinity. A unique and creative idea for interface assembly may provide a good starting point, but redesign and optimization is difficult without a method for evaluating the proposed interface. The understanding of an interaction places interface development and application within reach. Traditional techniques have supplied qualitative information on antibody recognition for interface design and are widely used. Nanotechnology has expanded immunoassay options for the study of more diverse systems and, combined with QCM, provides a label-free, quantitative alternative. These analytical techniques can determine structural integrity of assembled nanoarchitectures, can provide equilibrium and kinetic binding constants of

biological entities, and can detect analytes (antibodies, toxins, etc.) for medical diagnostic applications.

Radiolabelled immunoassays were one of the first techniques used in the detection of antibody or antigen in biological systems. In this assay, radioisotopes, commonly ^{125}I , were used to label the antibody or antigen and scintillation counters measured the gamma or beta emission of the isotope. This provided low detection limits needed for immunoassays, but regulation of radioactive isotopes made this technique inconvenient to use.¹⁰⁰

Another standard immunoassay is the enzyme-linked immunosorbant assay (ELISA). Its success comes from the ability to amplify binding through an enzyme reaction, which produces a spectroscopic signal. There are many formats for an ELISA experiment, though the indirect sandwich assay format has been widely accepted. In this format, the primary antibody is immobilized on a solid support (typically a well-plate) and antigen is allowed to bind. A second, polyclonal antibody for the antigen from a different species than what was used as the primary antibody is then added and binds to the other side of the immobilized antigen, creating a “sandwich”. An antibody that recognizes the second antibody (an anti-antibody) is functionalized with an enzyme (typically horseradish peroxidase) and allowed to bind. Finally, a substrate for the enzyme is introduced, which produces an enzyme product that is chromogenic. The chromophore is detected by conventional spectroscopic methods.¹² While the signal amplification from the enzyme reaction is beneficial, there are certain limitations to ELISA experiments. A lack of simple quantitation and excessive time required to assemble the complex immunomolecular biosensor, as in the case of an indirect sandwich assay, are poignant

drawbacks. An example is the recent development of a quantitative ELISA assay for the detection of human IgG, which requires 19 hours from analyte immobilization to chromophore detection.¹⁰¹ Other limitations include the need for labeling with a bulky enzyme, which could interfere with the antibody/antigen interaction, and the nonspecific adsorption of analyte to a hydrophobic well plate could lead to random orientation of binding sites and possible denaturation of substrate.¹²

Surface plasmon resonance spectroscopy (SPR) has recently been used for the detection of antibody binding. The details of SPR phenomena have been previously outlined.^{70, 102} Briefly, SPR is an optical technique that takes advantage of plasmon excitation in bulk metal by wave vector matched photons. The photons induce oscillations of free electrons in the metal, which then propagate an additional field into the contacting dielectric medium. The plasmon excitation requires a transfer of energy from the photons, which can be observed through the sharp minimum of reflectivity during resonance, leading to an SPR signal.¹⁰² Therefore, measuring the change in reflection angle provides real-time, label-free detection of antigen/antibody interaction. SPR has been used to study several different systems, an example being the characterization of FLAG peptide epitope arrays.²⁵ Important drawbacks of the SPR method are the complicated and expensive optics required for operation, loss of sensitivity at distances from the sensor, and interference from molecules with high molar absorptivity (Chapter II).

Radiolabelling, ELISA, and SPR are important and effective techniques for the evaluation of traditional antibody/antigen interactions. Inorganic materials, such as nanoclusters, offer useful spectroscopic and nanoscopic properties that can make analysis

convenient, but can also introduce added challenges. One of the first interfaces between materials and antibodies¹³ was designed because radiolabel immunoassays were cumbersome and enzyme immunoassays require delicate procedures.¹⁴ The potential of materials was harnessed to design a more simple method and successfully used antibody-functionalized latex beads and turbidity measurements to detect agglutination.^{13, 15} Improvements to this method quickly followed using electric pulses to promote antibody/antigen interaction and decrease reaction time.¹⁴

A similar, though more recent, nanoimmunoassay also used antibody-functionalized particles. These 70 nm diameter silica particles had exterior antibody functionalization and interior fluorophore entrapment. Fluorescent-labeling techniques have enjoyed long-lived success, though low fluorescence intensity and photoinstability have been recurring problems. Encapsulation of Ru(bpy)₃²⁺ fluorophore in silica nanoparticles yielded high intensity fluorescence and increased photostability due to exclusion of damaging oxygen.¹⁰³ These nanoparticles were compared to popular quantum dots (QDs), which are semiconductor nanoparticles with intense intrinsic fluorescence, and were found to have similar intensity and stability. Antibody-functionalized QDs have also been used as fluorescent tags for the imaging of live cells.^{26, 104}

Metal nanoparticles have been used as electrochemical labels for the simultaneous detection of four antigens, β_2 -microglobulin, IgG, bovine serum albumin, and C-reactive protein.²⁰ In this experiment, a large magnetic bead was functionalized with four types of antibodies corresponding to the four different antigens. After binding antigen to the antibody on the magnetic bead, antibody with unique nanoparticle labels bound to the immobilized antigen. Collection of the nanoparticle-labeled antibody and detection with

square-wave stripping voltammetry provided four unique signals from the reduction of four unique metal nanoparticles.²⁰

A microscopic technique often used in nanocluster characterization, but not in immunoassay, is transmission electron microscopy (TEM). Metal nanoclusters absorb electrons, making them visible in TEM, while small carbon-based molecules do not. In a recent study, antibody-functionalized nanoparticles were incubated with pathogens *Staphylococcus saprophyticus* and *Staphylococcus aureus* and examined with TEM. Functionalized nanoclusters bound to antibody binding sites and were detected. Furthermore, bacteria-bound magnetic particles were collected, thereby concentrating target pathogens.¹⁹

Success with traditional immunoassay formats prompted SPR research in the area of nanoimmunotechnology. In 1998, the Natan group showed SPR signal amplification of antibody-nanocluster complex binding as compared to free antibody.¹⁶ The usefulness of this technique was confirmed with the detection of human complement factor 4 (C4) and C4 attached to colloidal Au particles.¹⁰⁵

These techniques, along with others, have had some success in the evaluation of interfaces between immunology and nanoscale materials. They also have their drawbacks. Many suffer from a lack of sensitivity and use large diameter particles (50 – 1000 nm) with relatively low surface area. Others rely on labeling to provide a detectable signal, which can interfere with recognition events and change the immunoassay dynamics. In the case of SPR, nanoparticle labeling is used to acquire enhanced binding signals. Unfortunately, this has also been shown to significantly broaden peaks, leading to a loss of sensitivity, complicated time-resolved measurements, and limited structural

information.^{69, 70} Efforts to develop a label-free, time-efficient, quantitative assay format that allows for 3D substrates and multilayer adsorptions have involved the quartz crystal microbalance (QCM).²

Piezoelectric biosensors developed since 1990 have gained ground on traditional labeling experiments and on competing label-free instrumentation such as SPR.^{52, 106, 107} The field of QCM immunosensors has also developed rapidly.⁸⁸ Considering the age of the new, though explosive, field of nanotechnology (the Brust nanoparticle synthesis was published in 1994), QCM immunosensors for nanotechnology applications are limited. One example used gold nanoparticle growth to amplify antibody-mediated lung carcinoma cell detection using QCM (Figure 9d).¹⁰⁸ In these experiments a monoclonal antibody to cell surface antigen was immobilized on a polystyrene film and captured lung carcinoma cells. The same antibody conjugated to 10 nm diameter citrate-reduced gold nanoparticles bound to the immobilized cell in a typical sandwich scheme. Auric acid and NH₂OH were then introduced, reacted with the pre-existing gold nanoparticle, and caused the nanoparticle to grow. This growth created an increased QCM signal and allowed for the detection of cells at levels as low as 100 cells/mL. This method provided results similar to ELISA, but was less time consuming.

Another example used polymer immobilized colloidal gold particles (~ 15 nm diameter) as an alternative approach to antibody immobilization.¹⁰⁹ Thiol-terminated Fab antibody fragments will often denature on an unprotected hydrophobic gold QCM electrode, but retained activity when bound to the polymer/nanogold mixture. This nanoparticle-based immunosensor supplied a means for phenotyping leukemia cells for medical diagnostics with detection limits of 6000 cells/mL. An important technical detail

of this work was the ability to detect four different phenotypes simultaneously using an array of QCM sensors. Other nanoparticle-based QCM immunosensors have made use of peptide epitope functionalized nanoclusters (Chapters II-IV).

Conclusions and Future Directions

The future of bionanotechnology lies at the interface between biology and inorganic nanomaterials and relies on the ability to probe and evaluate that interface. Many analytical techniques, including AFM, TEM, NMR, and molecular imaging, have been developed for this very purpose, for the analysis of all types of interfaces. The quartz crystal microbalance is another technique that has evolved to become a central tool in the study of both biological and nanomaterials applications. QCM has principal advantages for the investigation of bionanotechnology over existing immunological techniques: low cost and ease of operation, quantitation, real-time measurements, and large wave penetration depth, to name a few. For these reasons QCM technology has been applied to the exploration of a variety of life science applications. Quartz crystal microbalance nanoparticle-based immunoassays are a relatively new field, but have been designed for the evaluation of several antigen mimics. Specifically, QCM has shown that antibody can recognize and interface with immunoreactive nanomaterials designed with linear and conformational peptide epitopes presented on the surface of monolayer protected clusters. This is only one interface that QCM has successfully characterized. Given the virtues of this technique and the vast number of possible combinations between biology and nanotechnology, more systems will doubtlessly be studied.

The prospects of biotechnology and nanomaterials science are most promising at their interface, where they overlap in the emerging field of bionanotechnology. This interfacial discipline further relies on analytical techniques that can probe the boundary where they meet. The quartz crystal microbalance is certain to be an integral tool in the exploration of this frontier. Specifically, QCM can expand its applicability through the design of new immobilization strategies for repeated, reversible interactions. An improved, commercially available, multichannel detection apparatus will improve throughput and multiplexing. In the realm of medical diagnostics and defense-based toxin detection, a blood sample, water-way, or gaseous area could be largely characterized through multi-analyte detection. This is possible because of the portability, low cost, and ease of use of existing QCM instruments and potential devices. Furthermore, advances in nanotechnology and improved understanding of biology will produce smart sensors and functional devices capable of carrying out an environmental analysis or capable of modulating an environment. Continued research on advanced nanomaterials in a biological paradigm using an effective QCM transducer can make this a reality.

CHAPTER II

QUARTZ CRYSTAL MICROBALANCE DETECTION OF GLUTATHIONE-PROTECTED NANOCLUSTERS USING ANTIBODY RECOGNITION

Introduction

Biosensors, particularly immunosensors, have received increasing attention in recent years due to the threat of bioterrorism,^{101, 110} the emergence and proliferation of disease,^{101, 111, 112} and the promise of biotechnology.^{5, 6, 21, 113} Enzyme-linked immunosorbant assay (ELISA) has become a standard detection method for its ability to amplify a spectroscopic signal from an enzyme reaction, but certain obstacles have limited its success. These limitations include a lack of simple quantitation and excessive time required to assemble the complex immunomolecular biosensor, as in the case of an indirect sandwich assay.¹² A case in point is the recent development and qualification of a quantitative ELISA assay for the detection of human IgG. The outlined procedure requires 19 hours from analyte immobilization to binding confirmation by chromophore detection.¹⁰¹ Furthermore, chromophore, fluorophore, or enzyme tags required for detection can affect the antigen/antibody (Ag/Ab) interaction and non-specific adsorption of analyte to a hydrophobic well-plate can lead to random orientation of binding sites and possible denaturation of substrate.¹² These issues present formidable challenges to accurate quantitation using ELISA.

Efforts to develop a label-free, time-efficient, quantitative assay format that allows for 3D substrates, multilayer adsorptions, and non-rigid biological recognition are an area of concentrated research interest.⁵² Two techniques that have emerged are surface

plasmon resonance spectroscopy (SPR) and the quartz crystal microbalance (QCM). Both techniques make use of wave-propagation phenomena: QCM uses acoustic waves and measures the frequency of acoustic impedance minimum, and SPR uses optical waves and measures the angle of reflection minimum. Similar performance is observed for both methods in detection limit, sensitivity, speed of real-time detection, and flow capabilities.^{106, 107} These benefits have allowed SPR to become a widely used technique,^{25, 114} but important advantages make QCM an attractive alternative for immunosensing. Advantages include the ease of setup and operation and the low cost of QCM as compared to the complicated and expensive optics of commercial SPR. Another advantage of QCM is the ability to work with 3D substrates and multilayer adsorptions. Due to evanescent shear waves, the sensitivity of both QCM and SPR exponentially decays with the thickness of substrate adlayer. Sensitivity depends on the depth at which these waves penetrate the contact liquid. Penetration depths have been calculated to be 150 nm in SPR and 250 nm in QCM (at 5 MHz), with a total decay length as large as one micron for QCM.^{52, 58, 68, 106} Experimentally, QCM showed no loss of sensitivity for layers as large as 400 nm,⁵⁸ where SPR showed significant peak broadening with layers less than 200 nm.⁶⁹ This peak broadening not only affects sensitivity, but can influence time-resolved measurements and limit information on structural effects.^{69, 70}

Examples of peak broadening in SPR come from the use of metal nanoclusters for signal amplification.^{16, 71, 72, 115} It was shown that binding of antigen-presenting nanoclusters to immobilized antibody increased the SPR shift as compared to free antigen binding.^{16, 71} This technique has been touted as a label-dependent amplification scheme for small molecules that are not readily detected by traditional SPR and compares to

amplification possibilities using antigen-nanoclusters, DNA-nanoclusters,¹¹⁶ or DNA-liposomes⁹⁸ with QCM. A result of this amplification is the increased broadening of the SPR curve with increased density of nanocluster or diameter of nanocluster.⁷² QCM has not suffered from this loss of sensitivity, even for extensive nanocluster adsorption (below).

Benefits of QCM have allowed a number of biological and non-biological systems to be studied. The development of an immunosensor for rapid detection of the food pathogen, *Listeria monocytogenes*, was reported¹¹⁷ and a study of stain formation as related to the large commercial market for tooth-whitening products was performed.¹¹⁸ More recently, a study between α -Gal oligosaccharide and anti-Gal antibody for therapeutics in xenotransplantation²⁴ and the development of an immunosensor for the detection of SARS-associated coronavirus⁸⁹ have been completed. An important non-biological system studied with QCM was the determination of adsorption kinetics of self-assembled monolayers (SAM) for materials and separations applications.⁸² A more complete review of QCM and its application to life sciences was recently reported.⁵²

This success does not imply that QCM is without challenge. Inherent complications include determination of a reliable relationship between frequency and adsorbed mass and the functionalization of a non-specific Au electrode surface.²⁴ Progress towards a reliable mass measurement has been facilitated by co-determination of oscillation frequency and damping resistance, but the mathematical relationship between the two terms remains complicated.^{56, 57} In 1959, Sauerbrey discovered a linear relationship between the frequency response of an oscillating piezoelectric crystal and mass deposited

onto that crystal. This is mathematically expressed by the Sauerbrey equation (Eq. 2),^{52, 57, 61}

$$\Delta f = -C_f \Delta m \quad (\text{Eq. 2})$$

where, Δf is the change in frequency, C_f is the sensitivity factor, and Δm is the change in mass. This relationship holds for mass loading that is rigid and strongly coupled, but has been shown to overestimate mass adsorption in liquid loading, viscoelastic samples, and in non-rigid recognition and binding of biological molecules.^{24, 52} Careful consideration of simultaneous mass and liquid loading has shown that Δf relates not only to adsorbed mass, but also to the density and viscosity of the contact liquid, as seen in Eq. 3,^{56, 57}

$$\Delta f \simeq -C_f \Delta m - C_f (\Delta \rho \eta / 4\pi f_0)^{1/2} \quad (\text{Eq. 3})$$

where, $\Delta \rho$ is the change in density, $\Delta \eta$ is the change in viscosity, and f_0 is frequency of the unperturbed crystal. As such, it is impossible to distinguish between mass adsorption and liquid loading by measurement of resonant frequency alone. Fortunately, the independent term of liquid loading resistance, R_L , depends solely on density and viscosity, according to Eq. 4.^{57, 59}

$$\Delta R_L \simeq (\eta_q / [c_{66} C_1]) + (N\pi C_1)^{-1} (\Delta \rho \eta / \pi f_s c_{66} \rho_q)^{1/2} \quad (\text{Eq. 4})$$

Measuring both changes in frequency and resistance permits decoupling of mass loading and density and viscosity effects.⁵⁷ A simple approach has been to create a calibration curve of change in frequency as a function of change in resistance for a system in which mass loading is minimal. This calibration allows for an *adjusted* frequency to be calculated, which is due to mass loading only. Adjusted frequency is then reliably converted to mass according to the sensitivity factor, C_f , which is known to be 56.6 Hz*cm²*μg⁻¹ for a 5 MHz crystal.^{52, 61}

Approaches to improve specificity in QCM have used self-assembled monolayers,^{24, 42, 73} ionic layering,^{74, 75} and electrochemical deposition.^{44, 78} Another route employs Protein A for immobilization of antibody in an accommodating conformation. Protein A is a cell wall protein that forms stable complexes with Au⁰ through van der Waal interactions ($K_a \sim 10^8 \text{ M}^{-1}$)⁸⁰ and contains five tandem domains that bind the Fc region of IgG with high affinity and selectivity. These properties optimize the presentation of antibodies such that both antigen binding regions are unobstructed.^{79, 80} With these improvements and previous advances, QCM continues to move forward as an effective analytical tool for immunosensing.

Monolayer-protected clusters (MPC) are nanoscale substrates whose unique properties of size and high ligand valency make them a potentially interesting platform for epitope presentation. MPCs consist of nanometer-sized metal cores that are completely passivated and protected by organic molecules through surface metal-sulfur bonds. They have received considerable attention for the unique consolidation of self-assembly techniques and metal materials chemistry, as well as for their chemical, electronic, and physical properties, a lack of air and water sensitivity, and convenient

characterization.^{31, 34, 39} Programmed specificity through the introduction of biologically relevant molecules is one of their most promising features and lends to the objective of creating functional nanodevices as protein mimics or to the assembly of nano-scale architectures. Progress towards these goals began with use of micron-sized immuno-latex beads, which had a small amount of antibody non-specifically adsorbed to the hydrophobic latex surface.¹⁵ Nam, et al. then created an immunoassay using micron diameter immuno-magnetic particles in conjunction with 13 nm diameter DNA/antibody derivatized gold clusters.¹⁷ Use of even smaller particles took further advantage of increased surface area and multivalency of biologically active ligand through the functionalization of various metal cores ranging from 3 to 12 nm diameter.²¹ A peptide epitope known to bind monoclonal antibody associated with the human malarial parasite, *Plasmodium falciparum*, was used and through a qualitative detection scheme it was shown that antigen-encapsulated nanoclusters could bind their target antibody.²¹ Through the development of a quantitative QCM binding assay, research presented here demonstrates the feasibility of accurate recapitulation of an epitope on a MPC. Furthermore, it provides a method for detecting nanocluster-antibody interactions, which will be important to future studies of the nanomaterials/immunology interface.

Experimental

Chemicals

Gold shot (99.99%) was purchased from precious metal vendors and was initially converted to $\text{HAuCl}_4 \cdot 3\text{H}_2\text{O}$ by boiling Au^0 in HCl/HNO_3 solution.¹¹⁹ N-(2-

mercaptopropionyl) glycine (tiopronin, reagent), Protein A (recombinant from *E. coli*, $\geq 95\%$), bovine serum albumin (BSA, fraction V, 96%), and sodium phosphate (monobasic, reagent) were purchased from Sigma. MUA (11-mercaptopundecanoic acid) (95%) was obtained from Aldrich. Glutathione (reduced, 98%) was purchased from Acros. Copper (II) perchlorate hydrate, iron (II) perchlorate hydrate, iron (III) perchlorate hydrate, zinc (II) perchlorate hydrate, and calcium chloride hydrate were obtained from Alfa Aesar company as reagent grade. Anti-glutathione rat polyclonal antibody was purchased from Abcam Ltd. NMR solvents were obtained from Cambridge Isotope Laboratories and water was purified using a Modulab Water Systems unit (~ 18 M Ω). Buffers were prepared according to standard laboratory procedure. Other chemicals were reagent grade and used as received.

MPC Synthesis and Characterization

Nanometer-sized gold MPCs were synthesized with glutathione (GSH) and tiopronin as passivating substrates, as previously described.^{30, 31} Briefly, GSH particles were synthesized by co-dissolving GSH and H₂AuCl₄•3H₂O in a 3:1 molar ratio in water, stirring for one-half an hour, and cooling in an ice bath. NaBH₄ was then added in a 10x molar excess of gold. Stirring proceeded one hour followed by removal of solvent under vacuum and lowering of pH to ~ 1 with HCl. Purification was achieved by dialysis with cellulose ester membranes (Spectra/Por CE, MWCO = 10,000). Tiopronin clusters were synthesized in a similar manner.³¹ Characterization techniques for all MPCs are described below:

Nuclear Magnetic Resonance. Proton NMR experiments were run at 300 MHz on a Bruker DPX-300 instrument with 5 sec relaxation times. Samples were dissolved in D₂O or D₂O with 10 mM sodium phosphate.

UV/vis Spectroscopy. Scans from 200-800 nm were taken of aqueous solutions in a 1 cm quartz cell and recorded with a Cary 100 BioSpectrophotometer.

Transmission Electron Microscopy. TEM images were taken on a Philips CM20 instrument after applying aqueous MPC samples to Formvar-coated 200 mesh copper grids (Ted Pella). The microscope operated at 200 keV with magnification in the range of 150 - 540000x.

Thermogravimetric Analysis. Percent organic by weight was determined by TGA on a TA Instruments TGA 2950 Module with Thermal Analyst 3100 using aluminum pans. Approximately 10 mg of MPC were dried, placed in a desiccator overnight, and analyzed under nitrogen from 0 to 550 °C.

Quartz Crystal Microbalance

Two separate Quartz Crystal Microbalance instruments were used in the detection of binding events. Initial experiments involving ionic layering with transition metal ions were completed on a battery-operated, QCM oscillator circuit of local design with a Fluke PM6681 Frequency Counter. The instrument was interfaced with a National Instruments GPIB card and was controlled with a LabVIEW 6i software program specifically designed for the instrument. The quartz crystal was held in a custom-designed glass cell between $\frac{3}{4}$ in. o-rings with a spring-loaded clamp and connections were made by attaching wires with silver epoxy (Epoxy Technology, EPO-TEK). The

glass cell was capped to prevent solvent evaporation and magnetic stirring was used when necessary. One inch, Ti/Au, AT-cut, polished, 5 MHz quartz crystals were purchased from Maxtek, Inc. This circuitry did not allow for ΔR_L measurements, making mass calculations suspect. As such, data (Figure 14) is plotted as Δf and approximate Δm is listed.

All other experiments were completed using a Research Quartz Crystal Microbalance (RQCM) with phase-lock oscillator, Kynar crystal holder, flow cell (100 μL cell volume), and 1 in., Ti/Au, AT-cut, polished, 5 MHz quartz crystals, all purchased from Maxtek, Inc. The holder was mounted with crystal face positioned 90° to ground to minimize gravity precipitation onto the surface.¹²⁰ A Variable Flow Mini-Pump (Ultra Low Flow) peristaltic pump with 1/16 in. silicon tubing was purchased from Fisher and used with the flow cell at rates in the range of 10 to 36 $\mu\text{L}/\text{min}$. Fresh tubing was cut before each run in order to keep contamination to a minimum and limit flow-rate deviations. The RQCM phase-lock oscillator provided loading resistance measurements and allowed for the examination of crystal damping resistance during frequency measurements. A calibration of resistance change as correlated to change in frequency and change in density and viscosity was completed using varying concentrations (0 to 40% w/w) of sucrose in water. All measurements were made at room temperature. Sensitivity is known to be $56.6 \text{ Hz}\cdot\text{cm}^2/\mu\text{g}$ for a 5 MHz crystal and a sensitive area of 1.28 cm^2 was used.^{61, 87}

Immunosensor Assembly

Detection of substrate binding was possible through the assembly of a sensitive and selective immunosensor. Two different sensor assemblies were used for the detection of

antibody. Initial experiments involved the immobilization of nanocluster on the surface of the quartz crystal gold electrode. This was achieved by first forming a self-assembled monolayer (SAM) on the gold electrode. Prior to formation, the gold electrode was cleaned with piranha (3:1 H₂SO₄/H₂O₂) and by electrochemical cycling for 15 min in 0.5 M H₂SO₄ from 0.1 to 1.3 V at 0.1 V/s. The SAM was assembled by soaking the Au in a 5 mM solution of 11-mercaptoundecanoic acid in ethanol for 24 hours. After rinsing with 1 mM aqueous NaOH and ethanol, excess metal perchlorate (Cu²⁺, Zn²⁺, Fe²⁺, Fe³⁺, Ca²⁺ [as chloride]) was added in ethanol or ethanol/water mixtures. Rinsing with ethanol continued, the gold was placed in ethanol, and excess GSH-MPC was added in a small amount of 1 mM aqueous NaOH.

The second immunosensor assembly consisted of the purchased quartz crystal with Au electrode, Protein A, and polyclonal antibody. In order to assemble the immunosensor, the Au electrode was first cleaned with piranha, a 3-to-1 mixture of concentrated H₂SO₄ and 30% H₂O₂, rinsed with ethanol, and cleaned in a Jelight UVO-42 ozone cleaner. The crystal was then mounted in the holder/flow cell, rinsed with 50 mM pH 7.2 phosphate buffer (PB), and brought to resonant frequency. Protein A was dissolved in equal parts PB and 0.1 M sodium acetate buffer (pH 4.5) to a concentration of 4.5 μM and pumped through the flow cell at 36 μL/min for 45 min. After a 10 min rinse with PB, BSA (76 μM) in PB was pumped for 10 to 20 min at 36 μL/min. Again, the crystal was rinsed with PB for 10 min. Polyclonal antibody in PB had a total protein concentration of 0.76 μM and was pumped through the flow cell at 28 μL/min until the saturation point was reached (usually 90 to 120 min). Total protein concentration was determined spectroscopically with a Bio-Rad Protein Assay kit, using BSA for

calibration, and a Bio-Tek Synergy HT spectrophotometer. Antibody binding was followed by 10 min of rinsing with PB, making the sensor ready for analyte binding.

Analyte Detection

In the case of immunosensor assembly by ionic layering, the structure was rinsed with 10 mM phosphate buffered (pH 7.4) saline (0.1 M NaCl) solution (PBS) and placed in PBS. Ten microliters of polyclonal antibody was then added directly into solution and stirred for a short period of time (~2 sec). Diffusion of antibody to the crystal was allowed over 2 - 6 hours.

In the case of antibody immobilization via Protein A, two nanocluster detection strategies were used. The first detection method involved constant flow of analyte in PB at various concentrations over extended periods of time. Concentrations of GSH-MPC ranged from 0 to 10 μ M, control analyte was 4.1 μ M Tiop-MPC or 1.0 mM free GSH. A flow rate of 36 μ L/min was used and adsorption values were recorded after 100 minutes or several hours of addition. Control experiments were conducted as above and newly prepared immunosensors were used for each sample.

In the second method, analyte was dissolved in PB at GSH-MPC concentrations between 0 and 10 μ M and pumped through the flow cell at 36 μ L/min for a set time 5.0 min, with each 5.0 min sample introduction being termed a “dose”. Flow dependent studies made use of 14 and 36 μ L/min rates. In all cases, adsorption values were recorded after unbound analyte was rinsed out of the flow cell. Newly prepared immunosensors were used for each dose.

Results and Discussion

Monolayer-Protected Cluster Synthesis and Characterization

Monolayer-protected clusters were synthesized as previously reported,^{30, 31} with GSH completely protecting the metal core. Though not a traditional antigen, GSH was used for its previous success with MPCs and the commercial availability of polyclonal anti-GSH. Control MPCs were also synthesized^{31, 44} with tiopronin, which is an effective truncate of the GSH tripeptide (Figure 10).

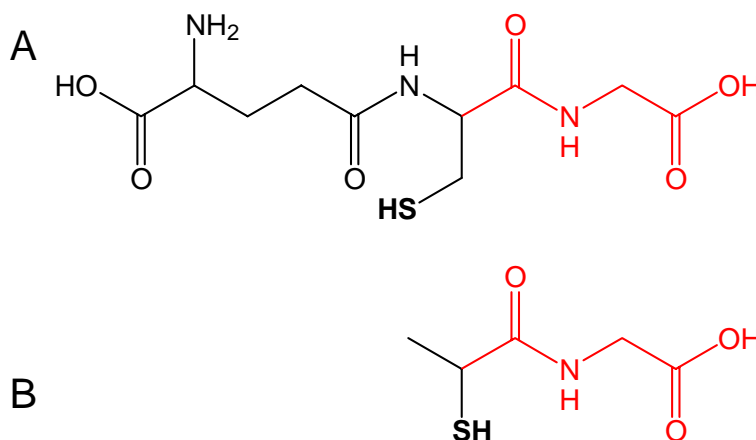


Figure 10. Structures of cluster-protecting ligands, with similarities in red. (A) Glutathione. (B) Tiopronin.

Although synthesis was slightly different for each of these nanoparticles (GSH-protected and tiopronin-protected), characterization was the same in all cases. Careful characterization was important for quantitative calculations and was completed via ^1H NMR, UV/visible spectroscopy, TEM, and TGA. Representative NMR, TEM, and TGA characterization data can be found in Figure 11. Organic molecules on MPCs yield characteristically broad peaks in ^1H NMR, which indicates cluster formation and purity.

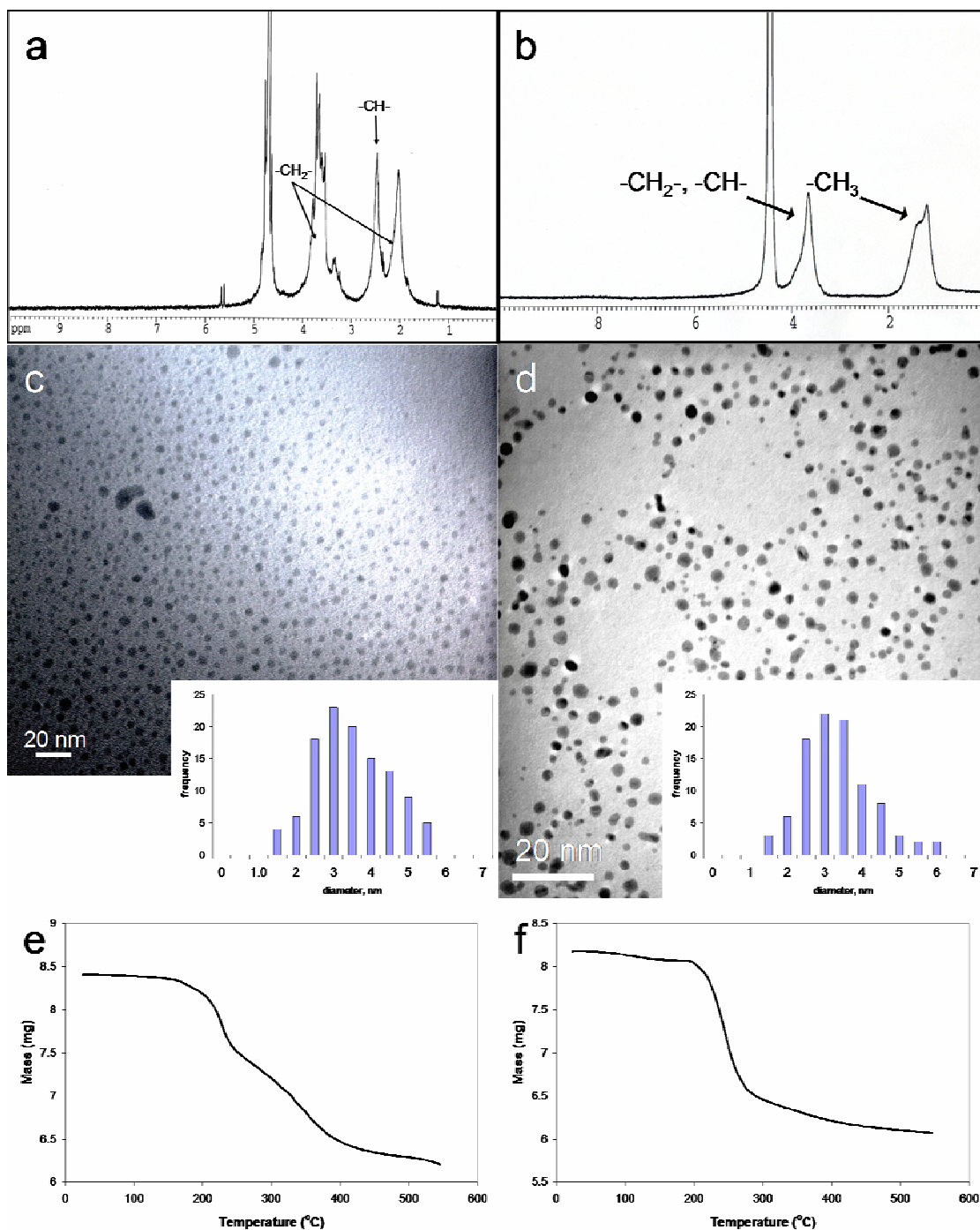


Figure 11. Characterization data for GSH-MPC and Tiop-MPC. (a) ^1H NMR of GSH-MPC in D_2O ; (b) ^1H NMR of Tiop-MPC in D_2O ; (c) TEM image of GSH-MPC, showing spherical clusters, (inset shows histogram with average near 3.7 nm); (d) TEM image of Tiop-MPC, showing spherical clusters, (inset shows histogram with average near 3.5 nm); (e) TGA of GSH-MPC showing loss of organic material between 200 and 400 $^\circ\text{C}$; (f) TGA of Tiop-MPC showing initial decrease in mass from water, followed by loss of organic material between 200 and 400 $^\circ\text{C}$.

Broadening has been proposed to be a result of large size distributions, fast spin relaxation associated with the very large molecules, and chemical shift distribution associated with different Au-SR binding sites (terrace, edge, vertex). It has been suggested that protons closest to the core of the MPC will experience the most broadening and the protons furthest from the core will experience the least, as those protons are most like a dissolved species.³⁹ The presence of sharp peaks in a ¹H NMR spectrum indicates unreacted starting material in the sample. In the ¹H NMR of tiopronin-MPC (Figure 11b), taken in D₂O, the large peak at ~4.6 ppm is the water peak, the peak at ~3.7 ppm is due to -CH₂- and -CH- protons, and the peak at ~1.2 ppm is due to the -CH₃- protons.

UV spectroscopy is used to confirm the presence and estimate size of MPC by the plasmon resonance band. This band is characteristic of nanoparticles due to the collective dipole associated with aggregation, but is absent in the bulk product. Experimental evidence has pointed to a decrease in energy and increase in line width associated with decreasing size of particle.³²

Transmission electron microscopy (TEM) is a valuable characterization technique in estimating size and shape of MPCs. Other important features such as core population (from “magic numbers”),³⁹ aggregation, and molecular bridging¹²¹ have been elucidated with the aid of TEM. Representative TEM images and histograms for GSH-MPC and Tiop-MPC can be found in Figures 11c,d.

Thermogravimetric analysis (TGA) is a simple technique that provides an MPC percent weight organic that is consistent with elemental analysis.³⁹ The sample is generally dried to remove adsorbed water and heated to the point at which all organic

material burns away, leaving only elemental gold. From the recorded change in mass, the percent organic composition can be calculated. Representative TGA data can be found in Figures 11e,f.

Estimation of the total MPC composition can then be made based on cluster diameter, percent organic composition, and certain assumptions: (1) the MPC is spherical with volume equaling $4/3\pi r^3$, (2) the Au packs in a face-centered cubic formation with packing efficiency of 74.05%, and (3) the van der Waal radius of Au is 0.170 nm.¹²² These data and assumptions allow an average estimation of the total number of Au atoms and total number of ligands in an MPC, allowing complete characterization.

Table 1. Results of calculations from MPC characterization.

MPC	Diameter, d_{avg}, (nm)	Avg. Composition	Avg. MW (kDa)
GSH	3.7 ± 1.2	Au ₉₅₃ GS ₁₉₉	220
Tiop	3.5 ± 1.0	Au ₈₀₇ Tiop ₂₄₆	199

Results for nanoclusters used in these experiments (Table 1) suggest that there is high ligand valency with 199 GSH epitopes per cluster.^{30, 31, 39} Control Tiop-MPC showed a ligand valency of 246, consistent with previously published data.^{31, 44}

Quartz Crystal Microbalance

A substantial difficulty in QCM has been ensuring an accurate measurement of mass loading. While resonant frequency is directly related to mass adsorption, frequency can also be altered by changes in density and viscosity of the contact solution. In traditional,

gas-phase experiments this was rarely a problem, but in biosensor applications where solutions of varying composition are continuously delivered to the sensor, density and viscosity become very important considerations. The effects of density and viscosity can be monitored and accounted for by measuring the changes in loading resistance of the QCM. Practical decoupling of viscous loading from mass loading was completed using simple experimental calibration. Sucrose was assumed to have no affinity for the QCM substrate, but affected the properties of the contact liquid. Increasing concentration of sucrose (changes in density and viscosity) caused decreases in frequency and increases in loading resistance that mirrored each other. Plotting Δf against ΔR_L gave a straight line with slope of -2.095 for a 5 MHz crystal and -15.27 for a 9 MHz crystal (Figure 12).

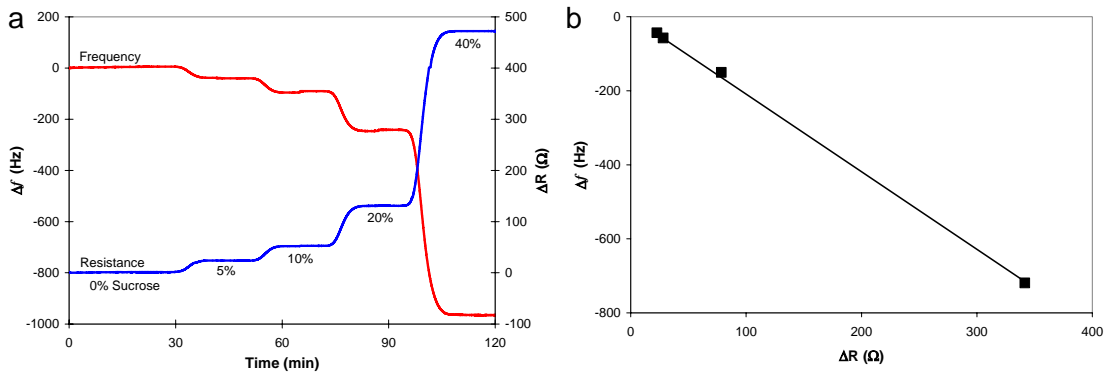


Figure 12. (a) QCM mass calibration for a 5 MHz crystal using different concentrations of sucrose to show the relationship between frequency and resistance in a non-mass loading system; (b) linear relationship between Δf and ΔR_L with slope = 2.095 and $R^2 = 0.999$.

This is the calibration factor and is the effect that a change in resistance (viscous loading) has on the frequency measurement. A measured ΔR_L can then be adjusted by the calibration factor and added or subtracted to Δf to provide an *adjusted* Δf that is due only

to mass loading. Sucrose concentrations of 0.00%, 5.02%, 10.0%, 20.0%, and 40.0% (w/w) were used in the representative example shown in Figure 12.

Immunosensor Assembly

The initial immunosensor used in the study of antibody binding to GSH-MPC involved the immobilization of the nanocluster and subsequent antibody detection. Immobilization of the MPCs on the gold QCM electrode proceeded by ionic layering using transition metals. This method was first examined as both GSH- and Tiop-MPCs were already functionalized with carboxylic acid groups. The protocol for this metal-carboxylate chemistry was adapted from literature⁷⁴ and is summarized in a cartoon schematic (Figure 13a). Cu^{2+} ion was initially used, as literature suggested,⁷⁴ and binding of Cu^{2+} to carboxylate, MPC to Cu^{2+} , and antibody to MPC was recorded. The addition of the carboxylic acid-terminated thiol (MUA) to the gold in the form of a SAM could not be followed in real time as the kinetics of the reaction appeared to be very slow.

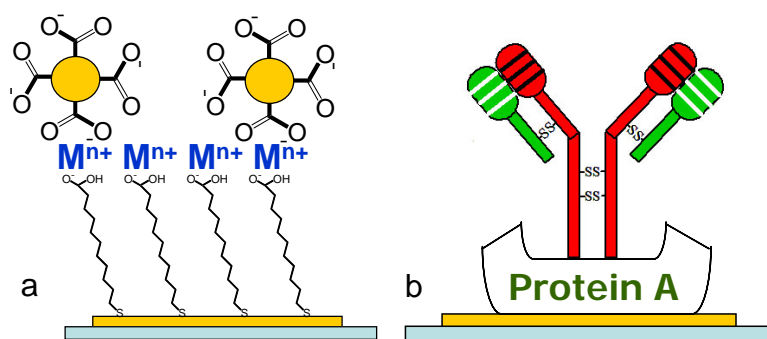


Figure 13. Cartoon of immunosensor assembly (not to scale). (a) Ionic layering, presenting MPC to solution for antibody binding ($\text{M}^{n+} = \text{Cu}^{2+}$, Fe^{2+} , Fe^{3+} , Zn^{2+} , or Ca^{2+}); (b) Protein A presentation of antibody for MPC binding.

Formation of the monolayer was confirmed by observing a discrete change in frequency of -19.1 Hz over 12+ hours and by cyclic voltammetry of the bare gold vs. SAM covered gold (data not shown). Sequential addition of Cu^{2+} , GSH-MPC, and anti-glutathione polyclonal antibody was completed and provided encouraging results (Figure 14).

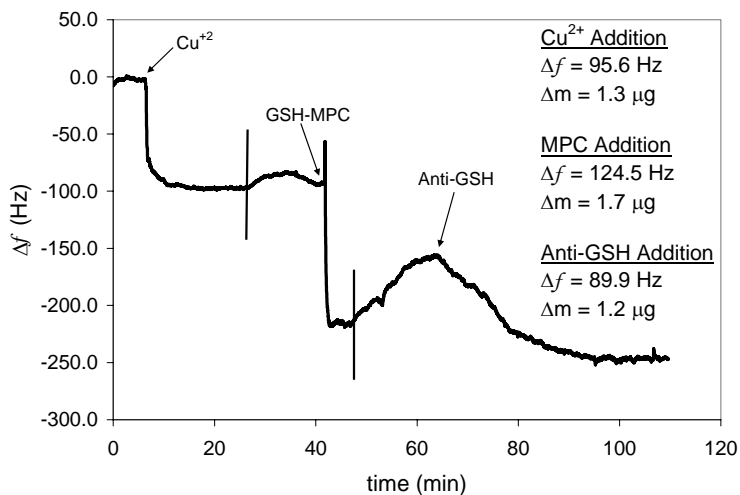


Figure 14. Detection of Cu^{2+} , GSH-MPC, and antibody binding via QCM (solid lines indicate rinsing and a change of solution).

Changes in frequency for the Cu^{2+} and MPC additions were both sharp and apparently rigid, but upon rinsing and change of solution from 87.5% ethanol to phosphate buffered saline the frequency began to slowly rise. This is suspected to be from the slow solvation of MPC and its removal from the QCM surface. This lack of stability in the complex led to an examination of other cations (*e.g.*, Fe^{2+} , Fe^{3+} , Zn^{2+} , and Ca^{2+}). The stability of these complexes should depend on strength of coordination (Irving-Williams series) and the solubility product (K_{sp}) of the complex. According to these parameters, it was thought that either Fe^{2+} or Ca^{2+} would provide the most stable complex, but acceptable stability

was not observed in either case when aqueous solutions of moderate ionic strength were used. Nonetheless, GSH-MPC was immobilized, at least briefly, on the surface of the QCM, forming a moderately viable immunosensor.

Assembly of a more stable, selective, and sensitive immunosensor proceeded by layering of Protein A, BSA, and anti-GSH polyclonal antibody onto the gold QCM electrode (Figure 13b). These steps led to the immobilization of antibody in an appropriate conformation and the detection of antigen-protected clusters. Construction began with rigorous cleaning of the Au electrode with piranha and ozone and continued with immobilization of Protein A. Recombinant Protein A from *E. coli* was used at a pH consistent with its isoelectric point (pH 5.5) in order to provide the tightest binding, while the non-specificity of the interaction led to rapid association. Binding was also relatively consistent, as six discrete experiments showed an average Δm of $1.83 \pm 0.08 \mu\text{g}$ and a relative percent deviation of 4%. The magnitude of this signal allows easy measurement, but does not correlate to an ordered monolayer of protein. If Protein A (45 kDa) is assumed to be 5 nm in diameter (from crystallographic data¹²³ of a protein of similar size), its adsorption footprint would have an approximate area of 20 nm^2 . The area of the Au electrode is $1.28 \times 10^{14} \text{ nm}^2$, which would allow 6.4×10^{12} proteins or $0.48 \mu\text{g}$ in a perfectly packed monolayer. Our data indicates a multilayer of protein bound to the surface, ensuring complete coverage of the Au electrode. A representative case of Protein A binding can be seen in the first 60 minutes of adsorption in Figure 15.

After thorough rinsing, the sensor surface was blocked with BSA to limit non-specific adsorption of antibody and analyte and to ensure that no Au remained exposed. Repeated independent measurements of BSA adsorption yielded an average Δm of $0.1 \pm 0.1 \mu\text{g}$

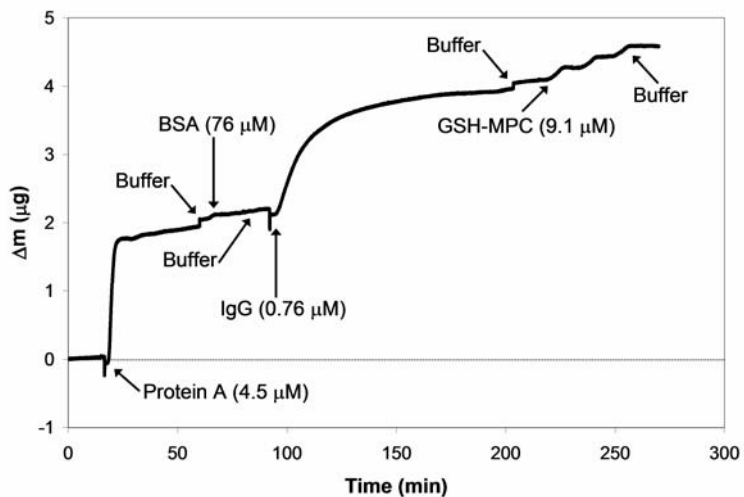


Figure 15. Representative Protein A, BSA, IgG, and MPC binding.

(Figure 15), consistent with complete Protein A coverage in the previous step. Unbound BSA was removed by rinsing with PB.

Immobilization of polyclonal anti-glutathione antibody by Protein A completed the immunosensor preparation. Due to the use of a slower flow rate and the nature of protein/protein recognition, saturation of binding sites took significantly longer (90 to 120 minutes). Considering the multilayer of Protein A on the electrode, antibody binding was reasonably stable and consistent with an average Δm of $1.8 \pm 0.3 \mu\text{g}$, and relative percent deviation of 20%. This equates to $9.4 \times 10^{-12} \text{ mol/cm}^2$, but due to accessibility, sterics, and the size of IgG as compared to Protein A (150 kDa vs 45 kDa), the stoichiometry of multilayer binding is unclear. Representative antibody binding data is presented in the 90 to 200 min block of Figure 15.

Analyte Detection

Following the completion of the immunosensor, analyte was detected. In the case of the preliminary immunosensor design (ionic immobilization of GSH-MPC), the analyte was polyclonal anti-GSH antibody. Due to the instability of the immunosensor architecture, GSH-MPC was likely separating from the QCM surface, giving rise to a slow increase in frequency (Figure 14, 45-60 min). This is suspected to be from the slow solvation of MPC and its removal from the QCM surface. Upon antibody addition, the frequency began to decrease. This is due to the antibody slowly recognizing and binding to MPC still on the crystal, thereby ceasing MPC solvation and decreasing frequency. The effect of non-specific binding was also considered by building the same ionic layers, but introducing monoclonal anti-HA antibody instead of polyclonal anti-glutathione. Anti-HA antibody recognizes an epitope with amino acid sequence YPYDVPDYA, which is vastly different than glutathione. As expected, anti-HA did not bind as well or as specifically as anti-GSH. There was some amount of non-specific binding though, as a change in frequency of ~25 Hz was observed. Further progress with the use of ionic layering has since ceased as the complexes are not stable in aqueous solutions of moderate ionic strength.

Following completion of the more stable, Protein A-based immunosensor, analyte was detected by two different approaches. In this case, the analyte was the nanocluster, rather than the antibody. The first method involved analyte addition over extended periods of time, which provided large, easily observable Δm values, but adsorption was not exclusive to antibody recognition. It is hypothesized that the nanocluster was

recognized by the antibody, causing binding and nucleation that led to random aggregation of MPCs. This precludes the application of a Langmuir isotherm as analyte

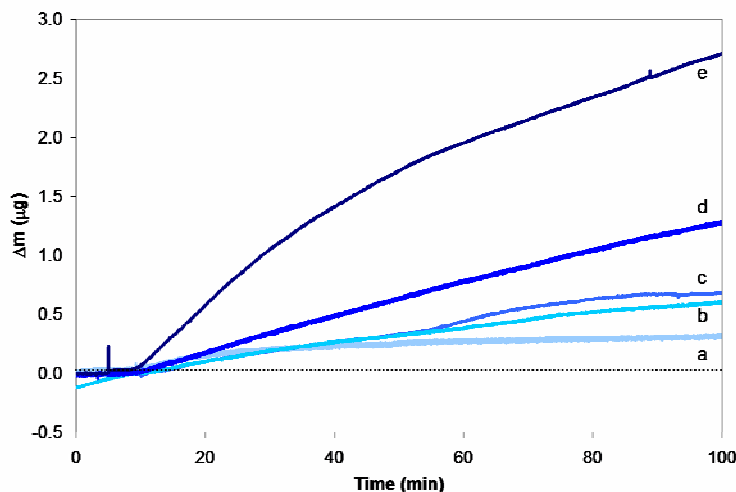


Figure 16. Antibody recognition and binding of GSH-MPC, followed by non-specific aggregation over an extended period of time, showing no saturation point. (a) 2.8 μM GSH-MPC; (b) 5.1 μM ; (c) 5.1 μM ; (d) 6.8 μM ; (e) 9.1 μM .

molecules are clearly interacting with each other. Data from these experiments are available in Figure 16.

The second approach introduced analyte by small “dose” amounts. This used smaller total amounts of cluster and biased stronger antibody recognition over weaker non-specific binding, but produced smaller Δm values. Additionally, this method was more time and material efficient than multi-hour experiments. Detection was ultimately achieved by introducing MPC for a set time of 5.0 minutes, with each sample introduction being termed a “dose.” Six doses, ranging in MPC concentration from 0.45 to 9.1 μM , provided Δm values that fit a logarithmic curve, showing saturation of the immunosensor (Figure 17a). Altering the flow rate used in dose delivery affects Δm , as expected, with an increased flow rate yielding an increased Δm (Table 2).

Table 2. Data for Δm dependence on flow rate for two doses of equal [GSH-MPC].

	Dose A	Dose B	Ratio B/A
[GSH-MPC] (μM)	4.5	4.5	1.0
Flow Rate ($\mu\text{L}/\text{min}$)	14	36	2.6
Total mol/dose	1.6×10^{-12}	4.1×10^{-12}	2.5
Δm (ng)	71	150	2.1

The significance of these results is supported by control experiments using tiopronin-MPC and free GSH. Tiop-MPC displayed minimal binding ($\Delta m \simeq 0.01 \mu\text{g}$) and was not recognized by the antibody, highlighting its specificity. Free glutathione showed an unexpected result of a negative Δm or mass removal. It is suspected that GSH, with its free thiol from Cys, is small enough to penetrate the IgG and Protein A layers to form Au-S bonds. This partial self-assembly of a monolayer of GSH displaces Protein A and IgG causing a rise in frequency or a negative Δm and masks free GSH recognition. Binding curves for three doses as compared to these control experiments are available in Figure 18.

Equilibrium parameters, association constant (K_a) and dissociation constant (K_d), were determined by fitting to a Langmuir adsorption isotherm (Eq. 7).^{24, 52, 87}

$$\Delta m = \Delta m_m(K_a C / (1 + K_a C)) \quad (\text{Eq. 7})$$

Eq. 7 can be rearranged such that Δm is plotted versus $\Delta m/C$ to obtain a straight line with slope $1/K_a$ and a y-intercept of Δm_m (Eq. 8).

$$\Delta m = -(K_a)^{-1}(\Delta m/C) + \Delta m_m \quad (\text{Eq. 8})$$

Plotting the data in this fashion provides a maximum binding value for saturation (Δm_m) of $0.25 \pm 0.01 \mu\text{g}$, a K_a of $3.6 \pm 0.2 \times 10^5 \text{ M}^{-1}$ and a K_d of $2.8 \pm 0.2 \times 10^{-6} \text{ M}$ (Figure 17b). The steady-state fractional coverage, Θ_i , can then be found for various concentrations of analyte using K_a and Eq. 10.⁸²

$$\Theta_i = C/(C + K_a^{-1}) \quad (\text{Eq. 10})$$

Values for steady-state fractional coverage are plotted parallel to Δm in Figure 17a and agree with immunosensor saturation and the calculated Δm_m . The affinity ($K_a = 3.6 \pm 0.2 \times 10^5 \text{ M}^{-1}$) of these antibodies for an antigen-protected cluster is similar to reported K_a values for some monoclonal antibodies. Several studies of anti-Gal monoclonal antibody binding to a variety of substrates²⁴ have described K_d measurements in the range of 10^{-6} to 10^{-12} M and monoclonal anti-FLAG M2 antibody²⁵ has been shown to bind peptide epitope arrays with a K_a of $1.5 \times 10^8 \text{ M}^{-1}$. Equilibrium constants for anti-GSH antibodies determined by QCM are comparable to literature, though indicate a lower affinity. This is reasonable as the antibodies are polyclonal, with only a subset recognizing the antigen presented.

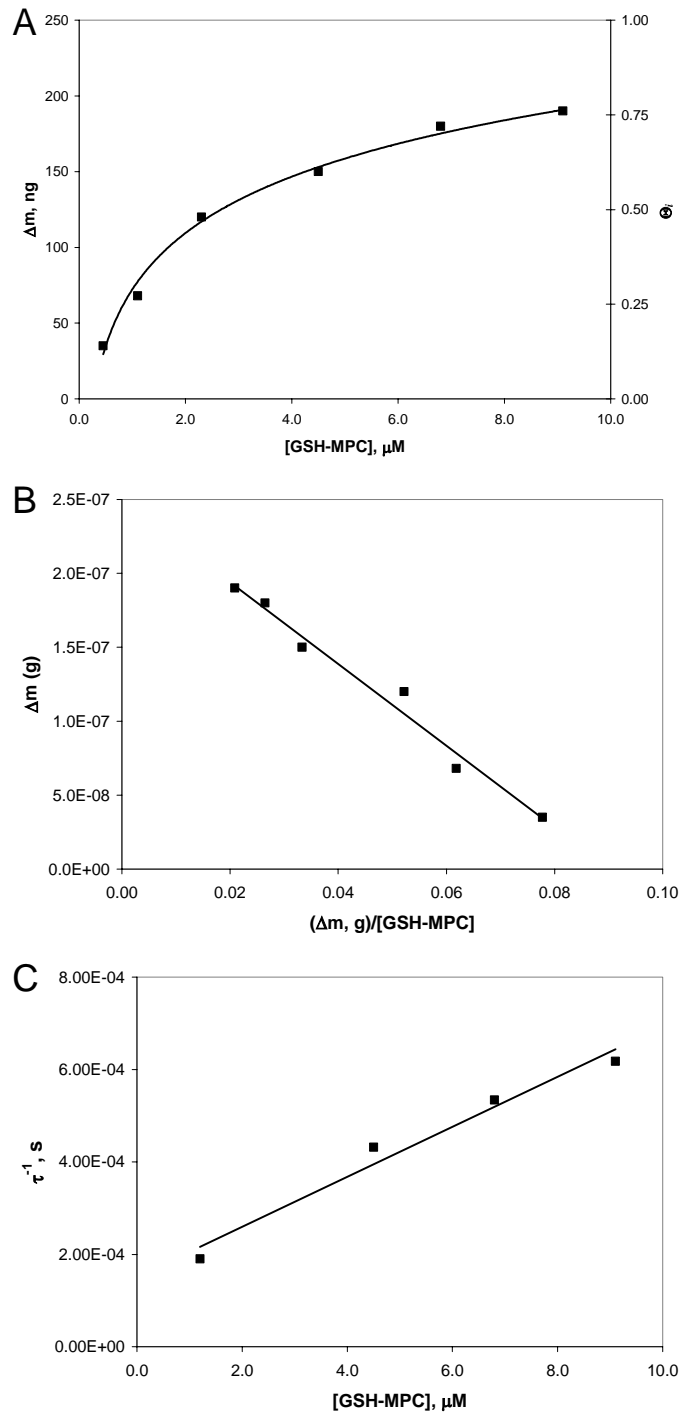


Figure 17. (A) Plot of Δm against the [GSH-MPC] for six doses, fit to a logarithmic curve with equation $y = 54\ln(x) + 72.3$ and $R^2 = 0.99$. Θ_i is included for these concentrations and Δm values. (B) Linear langmuir adsorption isotherm fit with equation $y = -2.8 \times 10^{-6}x + 2.5 \times 10^{-7}$ and $R^2 = 0.98$. (C) Adsorption kinetics using four doses, according to Eqs. 15 and 16, with equation $y = 54x + 0.00015$ and $R^2 = 0.98$.

Kinetic information can also be calculated from the time-dependant binding curves, like those in Figure 18, through fitting to the exponential expression (Eq. 15) and plotting τ^{-1} vs. C (Eq. 16),

$$\ln(1 - m_t/m_i) = -(\tau^{-1}) t \quad (\text{Eq. 15})$$

$$\tau^{-1} = k_f C + k_r \quad (\text{Eq. 16})$$

where, m_t is the mass at time (t), m_i is the mass at an infinite time, τ^{-1} is the time constant for a dose, k_f is the forward rate constant, and k_r is the reverse rate constant.^{82, 84, 85}

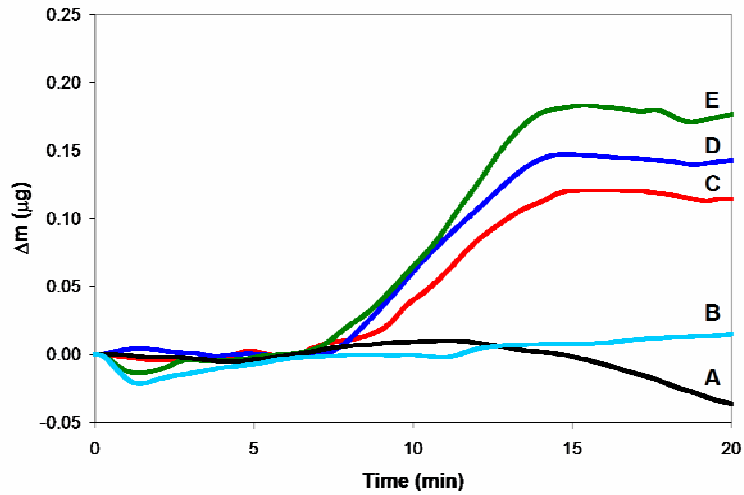


Figure 18. Binding curves for three of six GSH-MPC doses, Tiop-MPC, and free GSH. (A) 1.0 mM free GSH; (B) 4.1 μM Tiop-MPC; (C) 2.3 μM GSH-MPC; (D) 4.5 μM GSH-MPC; (E) 9.1 μM GSH-MPC.

Binding curves for four different [GSH-MPC] were used to obtain τ^{-1} values by fitting to Eq. 15 and determining the slope of the linear portion after forcing the y-intercept

through zero. Time constants were plotted against concentration, according to Eq. 16, to obtain rate constants, as seen in Figure 17c, where k_f is $5.4 \pm 0.7 \times 10^1 \text{ M}^{-1}\text{s}^{-1}$ and k_r is $1.5 \pm 0.4 \times 10^{-4} \text{ s}^{-1}$. The equilibrium adsorption constant, K_a , is equal to the ratio of k_f/k_r and was calculated to be $3.6 \times 10^5 \text{ M}^{-1}$, which correlates very well with the K_a found in the previous method (Figure 17b). As with the equilibrium constants, calculated kinetic constants are generally consistent with reported values for monoclonal antibody binding, protein receptor binding, and self-assembled monolayer (SAM) formation. Monoclonal anti-fluorescyl antibody has been reported⁸⁵ to bind to fluorescein-conjugated lipids with k_f of $1.99 \times 10^5 \text{ M}^{-1}\text{s}^{-1}$ and k_r of $2.18 \times 10^{-3} \text{ s}^{-1}$. It is reasonable for this forward rate constant to be larger than the rate constant for polyclonal anti-GSH due to the heterogeneity of a polyclonal sample and the lower effective concentration of active antibody. As such, the k_r values, which do not depend on concentration of active antibody, correlate very well. Deviations from rate constants for protein receptors, which also make use of molecular recognition, occur for similar reasons. Bracci, et al.¹¹⁴ have reported k_f in the range of 10^1 to $10^4 \text{ M}^{-1}\text{s}^{-1}$ and k_r in the range of 10^{-3} to 10^{-4} s^{-1} for binding of snake neurotoxin α -bungarotoxin to synthetic peptide mimitopes. SAMs have been described⁸² with k_f ranging from 10^2 to $10^3 \text{ M}^{-1}\text{s}^{-1}$, which falls between the rate of formation constants for monoclonal anti-fluorescyl antibody⁸⁵ and polyclonal anti-GSH antibody.

Equilibrium and kinetic constants calculated above indicate that recognition and strong association of polyclonal antibody with glutathione-protected cluster occurs, while important control experiments suggest where the recognition occurs. Tiopronin, which is an effective truncate of GSH (Figure 10), lacked recognition, suggesting that either the

non-natural, γ -glutamic amino acid or the tripeptide structure is essential for antibody recognition. This agrees with observations that non-natural amino acids are often important to biological structure, in the case of hydroxyproline, hydroxylysine, and crosslinked amino acids in collagen.⁹ Furthermore, presentation of the epitope through thiolate coordination to the MPC surface precludes possible antibody recognition of the cysteine thiol. This suggests that efficient antibody recognition depends on recapitulation of the peptide epitope through MPC presentation.

Conclusions

The QCM immunoassay presented has been shown to provide quantitative binding information concerning the detection of antigen-protected nanometer-sized cluster with immobilized antibody. This type of assay has several advantages over ELISA and SPR techniques, including the cost, ease of operation, and ability to detect multilayer adsorptions. Benefits of this particular method involve calibration for density and viscosity effects in frequency measurements, reliable response for multilayer adsorption, continuous sample introduction, and dose dependent antigen recognition and signal response. Signal amplification by coupling of antigen molecules to MPCs is an inherent benefit of this system, but was not considered a goal in immunosensor design. Using this technique we report K_a and K_d values of $3.6 \pm 0.2 \times 10^5 \text{ M}^{-1}$ and $2.8 \pm 0.2 \times 10^{-6} \text{ M}$ and k_f and k_r values of $5.4 \pm 0.7 \times 10^1 \text{ M}^{-1}\text{s}^{-1}$ and $1.5 \pm 0.4 \times 10^{-4} \text{ s}^{-1}$ for the binding of a multivalent antigen-protected MPC to its polyclonal antibody. These findings confirm the usefulness of this QCM method as a quantitative immunoassay and support previous observations²¹ that presentation of biologically-active antigen epitopes on nanocluster

surfaces produces robust immunoreactive materials with potential for nanoscale materials assembly and as diagnostic agents.

CHAPTER III

HEMAGGLUTININ LINEAR EPITOPE PRESENTATION ON MONOLAYER-PROTECTED CLUSTERS ELICITS STRONG ANTIBODY BINDING

Introduction

Biologically functional nanostructures rely on a solid support scaffold to provide a tunable surface for the presentation of functional units. Many materials scaffolds, such as two-dimensional surfaces,^{42, 124} carbon nanotubes,^{125, 126} dendrimers,^{127, 128} and semiconductor nanoparticles²⁶ exist and have been outfitted for different purposes. Monolayer protected clusters (MPCs) of nanometer dimensions have supported many functional units, in part due to the physical, optical, and electronic handles they offer.^{37, 39} Early examples of chemical functionalization of MPCs comes from the Murray group where they were successful in attaching spin labels, chromophores, fluorophores, electroactive species and other units to the surface of nanoclusters using traditional coupling reactions and place exchange reactions.^{28, 35, 44} This showed the ease with which nanoclusters can be functionalized and provided additional chemical reactivity.

Biological recognition units, in contrast to chemically and spectroscopically active units, can provide means for modulating biological systems or for nanostructure assembly through agglutination. These recognition units are often inspired by biological components or encompass a complete biological entity. This approach has been used in the assembly of DNA-functionalized nanoclusters,⁵ in the assembly of vancomycin-presenting antimicrobial nanoclusters,⁴⁵ and in many other areas of biology.

A particular biological system that has received considerable attention in nanoscale assembly is the immune system. There are numerous examples of covalent and non-covalent attachment of antibodies to latex beads,¹³ large colloidal gold clusters,^{16, 17} and large magnetic clusters.¹⁹ These nanoassemblies have been successfully used in advanced immunoassays and biodiagnostics but have limited potential as variable multifunctional structures. Due to the large size (150 kDa) of antibodies, packing density and ligand valency are low. Furthermore, their size and currently used attachment methods make it difficult to control antibody presentation or achieve the presentation of several different antibodies. While these antibody-presenting nanoclusters, or antibody-mimics, are useful, an alternative way to assemble immunoreactive nanostructures is through antigen presentation. Antigens are generally large proteins, viruses, or bacteria, but are known to interact with antibodies through discrete contact points, known as epitopes.⁴⁸ Epitopes can be continuous or discontinuous through the protein's amino acid sequence. Continuous epitopes have been routinely synthesized and are commonly used in epitope arrays for biodiagnostics,^{25, 114} but there are relatively few examples of peptide epitope functionalized nanoclusters.

The first example of a peptide epitope encapsulated nanocluster assembling with an antibody through the antibody/epitope interface was reported by Slocik, et al.²¹ A histidine-rich epitope from the histidine-rich proteins (HRP II and III) of the malarial parasite *Plasmodium falciparum* was used to stabilize the surfaces of a variety of metal and semiconductor nanoclusters. This produced a nanostructure with a single component monolayer that was immunoreactive with monoclonal anti-HRP II antibodies. The ability to assemble antigenic nanoclusters was further confirmed by the construction of a

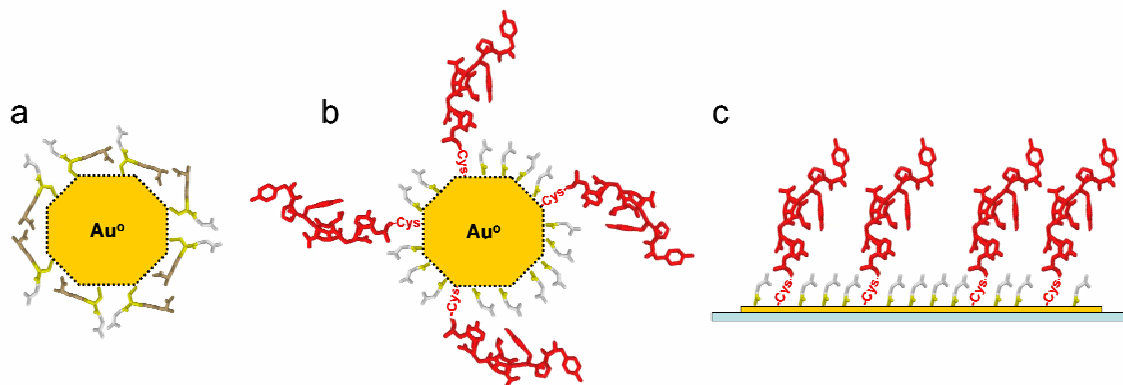


Figure 19. Cartoon representations of functional nanostructures: (a) GSH-MPC with a single component (3-amino acid peptide) three dimensional monolayer; (b) HA/Tiopronin-MPC with a dual component (10-amino acid peptide) three dimensional monolayer; (c) HA/Tiopronin-SAM with a dual component (10-amino acid peptide) two dimensional monolayer. (not drawn to scale)

glutathione-protected gold cluster and the development of a quantitative, real-time, quartz crystal microbalance (QCM) immunoassay.² This nanostructure consisted of a three amino acid peptide in a single component monolayer (Figure 19a) and was shown quantitatively to recognize polyclonal anti-glutathione antibody with an affinity constant of $3.6 \times 10^5 \text{ M}^{-1}$.

The next step in peptide epitope presentation, or antigen mimic design, is to control epitope presentation and epitope density in a dual component monolayer nanocluster. This can be completed through well-established place exchange reactions that have been previously used in MPC functionalization.^{28, 34} In these reactions, a thiolate-coated nanocluster is reacted with free thiolate in solution to promote one-to-one exchange, possibly through an associative, S_N2 mechanism (Figure 20).^{34, 41} Reaction conditions can greatly affect the extent of place exchange, allowing exquisite control of the functionalization procedure.

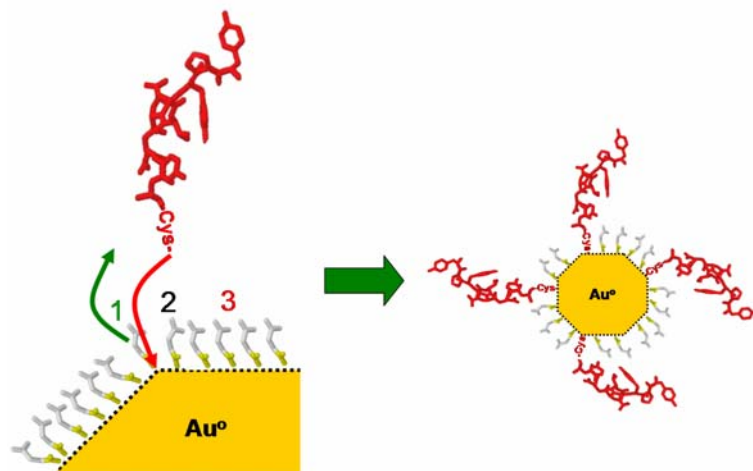


Figure 20. Cartoon schematic showing one-to-one place exchange between peptide thiolate in solution and thiolate on the surface of an MPC. Numbers indicate (1) fast exchange at vertex site, (2) moderate exchange at edge site, and (3) slow exchange at terrace site. Condition optimization allows for the presentation of multiple ligands.

Research herein demonstrates the assembly of a dual-component immunoreactive nanostructure through the place exchange of a peptide epitope from the hemagglutinin protein of influenza onto the surface of a tiopronin-protected nanocluster. Immunological evaluation of this functional nanostructure was completed using a QCM immunoassay and was compared to traditionally used peptide epitope arrays. Preparation and evaluation of these antigen-mimic nanostructures have important implications in the responsible handling of threatening toxins, in medical diagnostics, and in the development of anti-viral vaccines.

Experimental

Chemicals

Gold shot (99.99%) was purchased from precious metal vendors and was initially converted to $\text{HAuCl}_4 \cdot 3\text{H}_2\text{O}$ by boiling Au^0 in HCl/HNO_3 solution.¹¹⁹ N-(2-Mercaptopropionyl)-glycine (tiopronin, reagent), bovine serum albumin (BSA, fraction V, 96%), α -cyano-4-hydroxycinnamic acid (α -CHCA, matrix grade), and sodium phosphate (monobasic, reagent) were purchased from Sigma. Poly(diallyldimethylammonium chloride) (400,000-500,000 MW) (polyelectrolyte), bromoethylamine hydrobromide (99%), potassium hexafluorophosphate (98%), and tetrabutylammonium nitrate (97%) were obtained from Aldrich. Thioacetic acid (98%), 4,4'-dipyridyl anhydrous (98%), 1-[3-dimethylamino)propyl]-3-ethylcarbodiimide (98+%), and 4-(2-hydroxyethyl)piperazine-1-ethanesulfonic acid (99%) were obtained from ACROS Chemicals. Tetraoctylammonium bromide (98%) and N-hydroxysuccinimide sodium salt (98.5%) were obtained from Fluka, Inc. Anti-HA mouse monoclonal antibody (12CA5M5) was purchased from Vanderbilt Molecular Recognition Core Facility. NMR solvents were obtained from Cambridge Isotope Laboratories and water was purified using a Modulab Water Systems unit (~18 M Ω). Buffers were prepared according to standard laboratory procedure. Other chemicals were reagent grade and used as received.

MPC Synthesis and Characterization

Nanometer-sized gold MPCs were synthesized with tiopronin as the passivating substrate, as previously described.^{2, 31, 44} Characterization of MPCs was completed using nuclear magnetic resonance spectroscopy, UV/visible spectroscopy, transmission electron microscopy, and thermogravimetric analysis, as previously described.² MPCs used in the following experiments had a diameter of 3.5 ± 1.0 nm and an estimated composition of $\text{Au}_{807}\text{Tiop}_{246}$ (199 kDa).^{2, 39}

Peptide Synthesis and Characterization

Peptide epitopes were synthesized according to standard continuous flow fmoc solid-phase peptide-synthesis methods on an Advanced ChemTech Model 90 or Advanced ChemTech Apex 396 system using Wang resins. Deprotection of the fmoc-amino acids occurred in 20% piperidine for 15 min. Activated amino acids were in four-fold excess of resin loading capacity and in a 1:1:1:2 ratio (amino acid:HBTU:HOBt:DIPEA) with coupling reagents. The coupling step lasted 2 hours and was followed by a final fmoc deprotecting step. Cleavage from the resin and sidechain deprotection was completed in a one hour reaction with Reagent K (82.5% trifluoroacetic acid [TFA], 5% phenol, 5% DI water, 5% thioanisole, 2.5% ethanedithiol) or Reagent R (for Boc deprotecting, 90% TFA, 5% thioanisole, 3% ethanedithiol, 2% anisole). The peptide was then precipitated with diethyl ether, dissolved in water with a minimal amount of acetonitrile, and lyophilized on a Labconco Freezone 4.5 system. Purification was completed via reversed-phase HPLC on a Waters Prep LC 4000 with a 2487 Dual λ Absorbance

Detector (210 and 254 or 280 nm) and a Waters Delta Pak C18 (30 x 300 mm) column. Purity and composition were assessed by HPLC and MALDI mass spectrometry.

Place Exchange

Place exchange reactions between tiopronin-MPCs and thiolate-containing peptides were performed according to Hostetler, et al.^{28, 34} In exchange reactions, nanoclusters were co-dissolved in DI water (final concentration of 3.0 mg/mL MPC) with free thiolated peptides in varying ligand/peptide ratios (Table 3). Solutions were stirred at room temperature for approximately 3 days, collected, and purified by dialysis as previously described.^{2, 31} Extent of exchange was determined by ¹H NMR and by iodine reaction.³⁵ In the case of the iodine reaction, ~20 mg of mixed monolayer MPC was co-dissolved with 10 mg I₂ in 10 mL DI water and stirred for several hours. After removal of the iodine-passivated nanoclusters by centrifugation the supernatant was lyophilized and examined via ¹H NMR. The number of peptides per cluster was determined through NMR integration values and the following equation:

$$\frac{[\text{Normalized Peak Area}]_{\text{Tiop}}/[\text{H per Ligand}]_{\text{Tiop}}}{[\text{Normalized Peak Area}]_{\text{peptide}}/[\text{H per ligand}]_{\text{peptide}}} \quad (\text{Eq. 17})$$

Immunosensor Assembly

Detection of substrate binding occurred through the assembly of a sensitive and selective biosensor. Biosensor assembly proceeded according to three different immobilization techniques: electrodeposition, monolayer formation, and polymer ionic

layering. In all cases, the biosensor began with the quartz crystal gold electrode, which was cleaned with piranha, a 3-to-1 mixture of concentrated H_2SO_4 and 30% H_2O_2 , rinsed with ethanol, and cleaned in a Jelight UVO-42 ozone cleaner. In some cases, cleaning continued electrochemically in 0.1 M H_2SO_4 by scanning from 0.0 to 1.3 V against a silver wire reference electrode and platinum wire counter electrode at 50 mV/sec.

Electrodeposition of MPCs required the functionalization of tiopronin-protected MPCs. The redox couple, N-(methyl)-N'-(ethylamine)-viologen dinitrate (MEAV), was synthesized as previously reported.^{44, 78} Briefly, 4,4'-dipyridyl, was refluxed with 0.9 eq. of iodomethane in acetone to yield the monomethyl-viologen species. This product then refluxed with 4 eq. of bromoethylamine hydrobromide in acetonitrile under nitrogen. MEAV was collected as the monoiodide, monobromide salt and converted to the dinitrate salt according to Tang et al.¹²⁹ Coupling of the free amine on MEAV to the free carboxylic acid group on tiopronin proceeded according to standard amide coupling techniques^{44, 78} and tiopronin/MEAV complex was place exchanged onto MPC as above. Proton NMR was used to follow the steps of the reaction and determine purity. Electroactivity was followed by cyclic voltammetry using a CH Instruments potentiostat, gold working electrode (1.6 mm diameter), Pt wire counter, and Ag/AgCl reference. The working electrode was polished between each use with 0.050 micron alumina powder (Buehler Micropolish II), rinsed, and sonicated in water and ethanol. Redox couples were dissolved in borate buffer (pH 9.2, 100 mM) and CVs were recorded at a scan rate of 50 mV/sec from 0.0 to -0.75 V. Cluster was further functionalized with peptide as above. Biosensor assembly began with mounting a clean crystal in the QCM flow cell, rinsing with borate buffer, and bringing to resonant frequency. All solvents and solutions

were purged with N₂ for 10+ min and capped before introduction to the QCM. The electrochemical setup consisted of the Au QCM electrode as the working electrode, Pt wire counter electrode, and Ag/AgCl reference electrode connected to a BAS CV-27 potentiostat. The counter and reference electrode were placed in solution at the outlet stream of the flow cell. MPC (100 nM) was dissolved in borate buffer and introduced to the QCM at 36 μL/min for 8 minutes. Flow rate was then decreased to 28 μL/min and the potential stepped from 0.0 V to -0.8 V for 30 sec, stepped back to 0.0 V for 30 sec, and set to standby (no voltage) for 30 sec. This was repeated 4 to 5 times for reproducibility. This was also repeated in borate buffer with no MPC present.

Single and dual component monolayers were self-assembled on the gold QCM electrode. Typically, thiolate molecules were dissolved in ethanol at 1 mM concentration and reacted with a clean electrode overnight (~ 16 hours). In the case of a mixed monolayer, tiopronin and peptide were co-dissolved at final concentrations of 0.75 mM and 0.25 mM, respectively. After reaction, the QCM crystal was rinsed in ethanol and dried for use.

The mixed monolayer (tiopronin/peptide) was evaluated to approximate the amount of peptide in a typical monolayer. This was completed by forming a monolayer overnight and then removing the monolayer with portions of piranha (3:1 H₂SO₄/H₂O₂; CAUTION: handle piranha solutions with care). The freed ligands were collected, the piranha neutralized with NaOH, and the sample was desalted using a Sep-Pak C-18 filter prior to lyophilization. ¹H NMR was used to determine the ratio of peptide to tiopronin and this ratio was compared to the ligand density on a nanocluster to estimate the moles of peptide in the SAM.

The polymer ionic layering immobilization technique involved sequential layering of polyelectrolyte, MPC, and BSA on the surface of the QCM crystal's gold electrode. Before assembly the gold electrode was cleaned in piranha and ozone,² mounted in a holder with flow cell, rinsed with PB, and brought to resonant frequency (~5 MHz). A constant flow of 28 $\mu\text{L}/\text{min}$ was used throughout this assembly procedure. Polyelectrolyte (0.05%) in PB was pumped through the flow cell for 15 min. After a 10-min rinse with PB, MPC (2.4 μM) in PB was pumped for 30 minutes. Again the crystal was rinsed with PB for 10 min and was followed by BSA (16 μM) for 25 min. After a 10 min rinse with PB, the sensor was ready for antibody binding.

Analyte Detection

Antibody at various concentrations in PB was incubated with 100 nM MPC for 30+ minutes and purged with N_2 for 10+ minutes. Ab/MPC complex deposition was completed as above and compared to MPC deposition. Clean electrodes were used for each deposition.

Antibody binding to the SAM was completed by flowing antibody solutions for 17 min at 28 $\mu\text{L}/\text{min}$ and following with a PB rinse. A new SAM was assembled for each concentration of antibody studied.

Antibody binding to immobilized MPC consisted of flowing antibody solutions for 15 min at 28 $\mu\text{L}/\text{min}$ and following with a PB rinse. A new immunosensor was assembled for each concentration of antibody studied.

Results and Discussion

Nanostructure Assembly

Water-soluble, nanometer-sized monolayer-protected clusters were synthesized with tiopronin, a glycine derivative, as the protecting monolayer. Synthesis and characterization followed established procedure^{2, 31} and provided a cluster with the following properties: an average diameter of 3.5 ± 1.0 nm, an average composition of $\text{Au}_{807}\text{Tiop}_{246}$, and an average molecular weight of 199 kDa. Representative TEM image and proton NMR spectrum are available in Figures 21a and 21b, respectively.

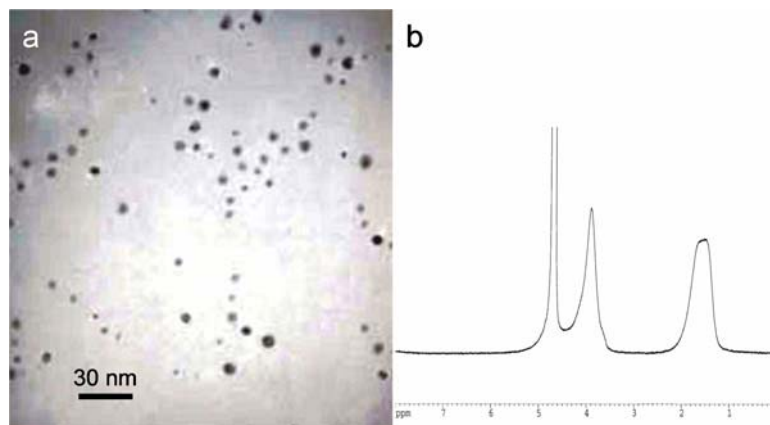


Figure 21. Nanocluster characterization. (a) TEM image of Tiop-MPC, showing spherical cluster. (b) ^1H NMR of Tiop-MPC. Broad peaks are indicative of nanocluster formation. A lack of sharp peaks indicates purity.

This synthesis provided a robust, water-soluble nanocluster with a single-component monolayer that acted as a scaffold on which to impart biological specificity. Such specificity was introduced via synthetic peptide epitopes.

The HA peptide epitope was identified from literature as an immuno-tag and a target for antibody neutralization.^{130, 131} The peptide sequence comes from the hemagglutinin

protein, which is one of two viral membrane glycoproteins of the influenza virus, and spans amino acids 98-106.¹³² The peptide was synthesized with an extra Cys residue at the C-terminus to facilitate place exchange and yield the sequence YPYDVDPDYAC (1205 Da, pI = 3.56). Representative HPLC chromatogram and mass spectrum are available in Figures 22a and 22b, respectively. This synthesis provided a linear peptide epitope that is known to be immunoreactive with a commercially available monoclonal antibody.

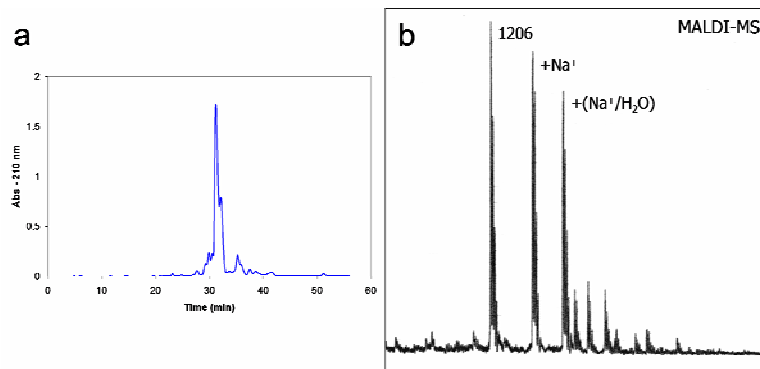


Figure 22. Peptide epitope characterization. (a) Chromatogram from the purification of the crude HA peptide using semi-preparative HPLC. The relatively sharp peak and lack of other major peaks indicates a homogenous sample. (b) MALDI-MS of HA peptide collected from the major peak of HPLC (a). Major peak (1206 m/z) is indicative of the pure peptide + H⁺. Other peaks are listed according to their adducts.

Assembly of the antigenic nanocluster was completed through place exchange reaction, where free thiolated peptides exchanged with tiopronin thiolates on the MPC. Reaction conditions can greatly affect the extent of exchange and have allowed the successful presentation of the HA peptide at varying degrees of peptide density.

Table 3. Ratio of nanocluster thiolate to exchanging thiolate alters the extent of peptide exchange. ^aInitial ratio of moles of nanocluster ligand to moles of free thiolated peptide. ^bFinal ratio of moles of ligand to moles of peptide on the surface of the nanocluster.

#	Feed Ratio L/P ^a	Resulting Ratio L/P ^b	Peptide Density (Peptides/MPC)
1	52	61	4
2	27	48	5
3	5.2	21	11
4	2.6	6.5	33

Altering feed ratios produced MPC samples with densities ranging from 4 to 33 peptides per cluster (Table 3), according to characterization by ¹H NMR (Figure 23). This array of functionalized nanoclusters was used to determine the optimal amount of peptide displayed for this particular antibody. The QCM immunosensor (discussed below) was used to ascertain the extent of antibody binding to each nanocluster and provided results

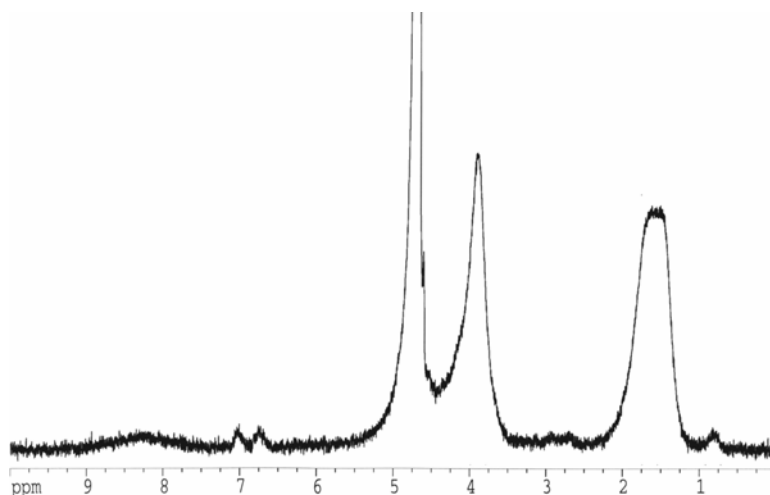


Figure 23. ¹H NMR of Tiop-MPC after peptide exchange with HA peptide epitope. Tiopronin peaks are still present. Peptide peaks are visible at approximately 0.8, 2.8, 6.8, and 7.0 ppm.

suggesting that a low density of peptide provided the most efficient antibody/epitope interaction (Figure 24). Accordingly, a nanocluster with 4 peptides per cluster ($\text{Au}_{807}\text{Tiop}_{242}\text{HA}_4$) was assembled for further study. A representation of this functional nanostructure is available in Figure 19b.

Three-dimensional, functionalized MPCs were compared to two-dimensional self-assembled monolayers in terms of antibody binding. The SAMs were assembled directly on the QCM gold electrode as dual-component monolayers consisting of tiopronin and

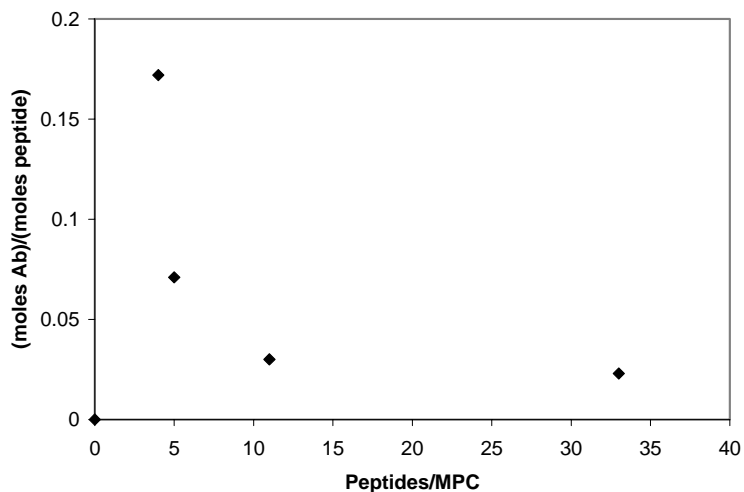


Figure 24. Antibody to functionalized nanocluster binding efficiency increases with decreasing density of peptide (peptides/nanocluster).

the HA peptide. A mixed monolayer of this type was assembled in order to mimic the surface of a functionalized nanocluster. Monolayers were assembled over ~16 hours using a 3:1 mole ratio of tiopronin to HA peptide and were initially probed by cyclic voltammetry to ensure insulation of the electrode, suggesting complete monolayer formation (data not shown). Further characterization provided an indication of the ratio of tiopronin to peptide in an assembled SAM. Piranha (3:1 $\text{H}_2\text{SO}_4/\text{H}_2\text{O}_2$) is generally

used to clean the QCM electrode after use. In this case, piranha solution liberated thiols from the SAM, which were collected, purified, and examined by ^1H NMR. This data indicated that the peptide represented 28 mole percent of the monolayer, which is 19 times more than the 1.5 mole percent of peptide on the nanocluster. A representation of the dual-component SAM is available in Figure 19c.

Quartz Crystal Microbalance Immunosensor

A QCM immunosensor was used to detect antibody binding to both 2D monolayers and 3D functional nanostructures. Details of the QCM instrument, setup, and operation have been previously reported.² Electrodeposition of MPC was completed by MPC-functionalization with both N-(methyl)-N'-(ethylamine)viologen and the HA peptide. The average cluster composition in these experiments was $\text{Au}_{807}\text{Tiop}_{219}\text{MEAV}_{17}\text{HA}_{10}$. Deposition and detection of MEAV-HA-MPC was conducted in the absence of antibody in order to obtain a baseline Δm for cluster only. This was achieved through the constant flow of MPC and sequential deposition and release for set time periods. A low concentration of 100 nM MPC was used in order to maximize the possible interaction between antibody and MPC and increase the signal from antibody detection. Unfortunately, this also decreased the amount of MPC electrodeposited onto the QCM. Each experiment was completed on a clean Au electrode and deposition was repeated four times to obtain an average Δm of $0.022 \mu\text{g} \pm 0.002 \mu\text{g}$ and percent deviation of 8.9%. The complete experiment can be seen in Figure 25. Initial mass adsorption is attributed to non-specific binding of the viologen or peptide portion of the MPC to the bare gold electrode. Stepping the voltage from 0.0 to -0.8 V caused a sharp increase in

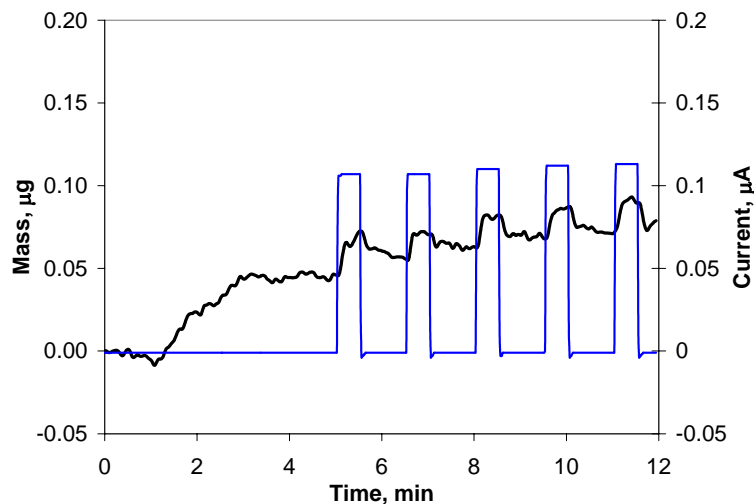


Figure 25. Electrodeposition of MEAV-HA-MPC. Mass adsorption is plotted in black, while current is plotted in blue.

current that is followed by mass adsorption that appears to near saturation in the 30 sec timeframe. Returning the voltage to 0.0 V causes a drop in current and subsequent mass stripping. Electrochemical stripping only removed approximately 70% of the adsorbed MPC, suggesting that some viologen reached the second oxidation step and bound irreversibly to the electrode. This changed the effective electrode surface area and accounts for a portion of the error.

In the case of the SAM, monolayer formation was the extent of immunosensor assembly and antibody binding to the monolayer was observed (Figure 26, below). Nanocluster, on the other hand, required immobilization on the surface of the QCM in order to detect antibody binding. This was completed using a highly charged polymer, or polyelectrolyte. After cleaning the QCM electrode, polyelectrolyte was introduced and bound non-specifically with an average Δm of $0.15 \pm 0.04 \mu\text{g}$. This provided a thin layer of positive charge for the ionic immobilization of functionalized nanocluster. MPC

bound non-specifically with a density of $1.7 \times 10^{-12} \text{ mol/cm}^2$ ($\Delta m = 0.44 \pm 0.06 \mu\text{g}$). Exposed polyelectrolyte was subsequently blocked with BSA ($\Delta m = 0.20 \pm 0.04 \mu\text{g}$) to limit antibody non-specific adsorption, completing the immunosensor assembly. Representative QCM data for immunosensor assembly is available in Figure 26.

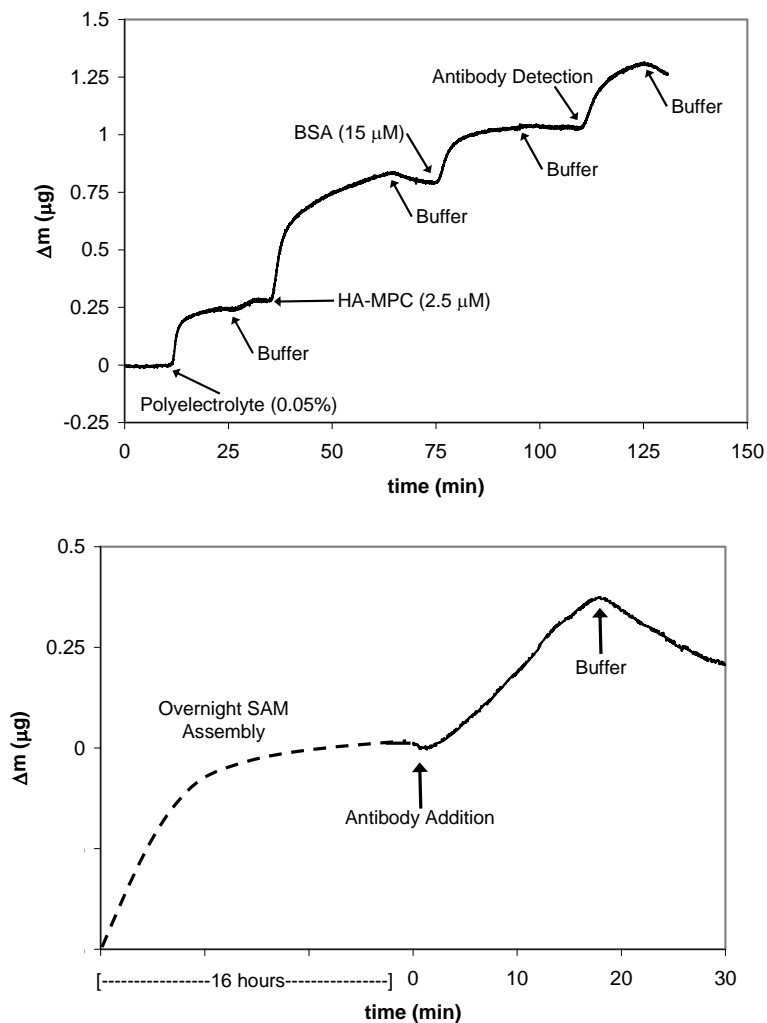


Figure 26. Representative polyelectrolyte, HA-MPC, BSA, and anti-HA antibody binding (top). Representative antibody binding to a mixed, two-dimensional monolayer, which was preassembled overnight (bottom).

Antibody Detection

Preliminary results for the detection of anti-HA via electrodeposition suggested the need for an improved detection scheme. Antibody was incubated with MEAV-HA-MPC before introduction to the EQCM. Unfortunately, exposure of protein antibody to a hydrophobic Au electrode caused strong non-specific binding. Antibody unassociated with MPC stuck to the QCM surface, blocking the electrode, before complex deposition could occur. Further work might require passivation of the Au electrode to inhibit IgG binding, while allowing electrochemical activity of the MEAV-MPC.

Monoclonal anti-HA antibodies were introduced to both SAM and MPC-based immunosensors in discrete dose amounts (Figure 26). Antibodies recognized and bound to the HA peptide epitope presented either in a 2D monolayer or on a 3D MPC. Due to the equilibrium process associated with biological recognition, buffer rinse that followed the binding event initiated antibody desorption for both 2D monolayers and 3D nanostructures. Increasing concentrations of antibody provided increasing adsorption to the point of saturation, following a Langmuir adsorption isotherm (Figure 27).

The mass adsorption for antibody to HA-MPC (Figure 27, solid square) is significantly lower than the mass adsorption for antibody to HA-SAM (Figure 27, solid triangle). This is due to the large amount of peptide in a densely packed 2D monolayer. In this case, peptide composes 28 mole percent of the SAM monolayer, which is 19 times greater than the 1.5 mole percent of peptide in the MPC monolayer. While this allows more antibody adsorption on the 2D surface, it does not necessarily increase the efficiency of adsorption.

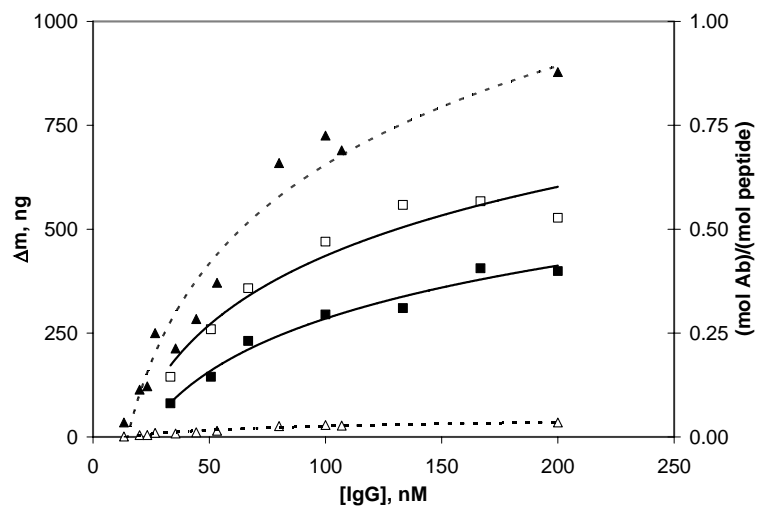


Figure 27. Antibody binding to immobilized HA-MPC (square, solid line fit) and HA-SAM (triangle, dashed line fit) is represented as total adsorbed mass (solid) and as the ratio of moles of antibody bound to moles of peptide available (outline). Lines indicate a non-linear fit.

When these adsorption values are plotted in terms of moles of antibody bound versus the moles of peptide presented, an estimation of antibody binding efficiency can be made. For these estimations every peptide in a SAM is considered to be available for binding. HA-MPC, on the other hand, is immobilized in such a way that approximately half its peptides are buried in polyelectrolyte and half are presented to solution. At saturation antibody binding to HA-MPC is near a ratio of 0.5, which correlates to one antibody to every two peptides or one antibody to every nanocluster. This is reasonable as each antibody has two antigen binding regions and suggests a high binding efficiency. The HA-SAM, on the other hand, is far below a ratio of 0.5 at saturation. There is more peptide in the monolayer than antibody can successfully bind to, indicating limited antibody binding efficiency. This poor binding efficiency results from steric effects and monolayer packing density in a 2D surface.

Antibody binding efficiency is relevant in terms of designing an economical nanostructure, but does not relate to antibody binding affinity. The affinity of the antibody for the epitope is determined by the equilibrium association constant (K_a), which can be calculated from fitting data to Langmuir isotherms or from kinetic rate constant information ($k_f/k_r = K_a$).^{2,3} Three methods provided three different K_a values for both HA-MPC and HA-SAM, ranging from $0.41 \times 10^7 \text{ M}^{-1}$ to $1.8 \times 10^7 \text{ M}^{-1}$ (Table 4). Statistics (t-test) reveal that these two sets of association constants are not significantly

Table 4. Equilibrium association constants and kinetic rate constants for antibody binding to HA-MPC and HA-SAM. ^a K_a determined through Langmuir isotherm plot of Δm vs $\Delta m/[\text{anti-HA}]$. ^b K_a determined through Langmuir isotherm plot of $[\text{anti-HA}]/\Delta m$ vs Δm . ^c K_a determined through ratio of kinetic constants ($k_f/k_r = K_a$).

	HA-MPC	HA-SAM
^a K_a ($\times 10^7 \text{ M}^{-1}$)	0.9 ± 0.3	1.8 ± 0.5
^b K_a ($\times 10^7 \text{ M}^{-1}$)	0.8 ± 0.2	1.6 ± 0.3
^c K_a ($\times 10^7 \text{ M}^{-1}$)	0.57 ± 0.07	0.41 ± 0.07
	HA-MPC	HA-SAM
k_f ($\times 10^5 \text{ M}^{-1} \text{ s}^{-1}$)	5.2 ± 0.4	1.4 ± 0.2
k_r ($\times 10^{-2} \text{ s}^{-1}$)	9.2 ± 0.5	3.5 ± 0.2

different from each other. This suggests that while the nanocluster may present the peptide epitope in a more efficient manner, the antibody recognizes and binds to the peptide epitope regardless of presentation style. This is reasonable for a relatively short chain, linear peptide epitope, though it may not hold for a more complex peptide epitope or nanostructure. Furthermore, affinities for the MPC and SAM correlate well with previously reported association constants. An early study¹³³ of a similar peptide (acetyl-YPYDVDPDYASLRS-NH₂) determined an association constant of $5.0 \times 10^7 \text{ M}^{-1}$ for an

anti-HA antibody. A K_a of $0.32 \times 10^7 \text{ M}^{-1}$ was more recently reported¹³⁴ for the anti-HA recognition of a similar peptide (fluorescein-GYPYDVPDYA) in a fluorescence-based assay.

Conclusions

Two functional nanostructures have been assembled and evaluated for their ability to interface with antibodies. The first, a 3D peptide epitope-presenting nanocluster, was optimized for efficient antibody interface and had a low peptide density of 4 peptides per nanocluster. Immobilization of this nanocluster in the assembly of a QCM immunosensor was attempted by viologen electrodeposition and by ionic layering, which proved to be more successful. This produced an average association constant of $(0.7 \pm 0.2) \times 10^7 \text{ M}^{-1}$. The second was a traditionally-used mixed 2D monolayer that showed antibody binding limited by steric effects and an average association constant of $(1.3 \pm 0.8) \times 10^7 \text{ M}^{-1}$. The MPC compared well with the SAM and, in fact, had no significant difference in terms of equilibrium association constant. We have synthetically assembled nanoparticle antigen mimics that are immuno-functional complements to this monoclonal antibody and we did so without the use of the intact protein. This curtailed the handling of delicate, possibly dangerous, protein antigens and has implications for the study of more threatening agents. This design and assembly process has, therefore, produced multi-component, antigenic nanoclusters with tremendous potential. Water-soluble nanoparticles that present known neutralizing peptide epitopes from protein antigens of the influenza virus could potentially be used in anti-viral influenza vaccines.

CHAPTER IV

ENHANCED ANTIGENICITY OF NANOCCLUSERS PRESENTING CONFORMATIONAL PEPTIDE EPITOPES FROM THE PROTECTIVE ANTIGEN OF B. ANTHRACIS

Introduction

Research at the interface between biology and nanomaterials is of recent interest and has produced a number of exciting and successful examples of structurally well-defined interfaces.^{3,4} Progress towards specifically interfacing immunology with nanoparticles is highlighted by an important approach that made use of a peptide epitope known to bind monoclonal antibody associated with the human malarial parasite, *P. falciparum*. This was the first example of antigen encapsulated nanoclusters assembling with antibodies through the antibody/epitope interface.²¹ A more recent example used glutathione-encapsulated nanoclusters and polyclonal anti-glutathione antibodies. This approach confirmed the ability to assemble single-component monolayer nanoclusters with antibodies and provided an analytical technique for rigorous evaluation of interface assembly using the quartz crystal microbalance.²

More complex nanostructures, specifically presenting peptide epitopes in a dual-component monolayer, require scaffold properties that are common to monolayer protected clusters (MPCs). MPCs capped with tiopronin ligand are water soluble; their average diameter, ranging from approximately 2 to 5 nm, is on the order of small proteins;^{2, 31, 44} they are easily characterized by conventional techniques, and have convenient optical and electronic properties.³⁹ The tiopronin ligand, a thiolated

derivative of glycine, is relevant to biological systems and provides the cluster with an overall negative charge.⁴⁴ Well-studied ligand coupling or place exchange reactions³⁴ have allowed for further functionalization of the cluster and the development of more complex antigen mimics. Specifically, Tiop-MPC presenting a linear decapeptide from the hemagglutinin protein of influenza was shown to specifically interface with monoclonal anti-hemagglutinin antibody.⁴⁹ This recognition relied solely on primary structure or amino acid sequence as this was a linear epitope, tethered to the MPC at one point.

While linear peptide epitopes are useful under simple conditions, the introduction of secondary structure or local conformation, relevant to physiological conditions, could increase antibody affinity, producing a more potent, efficient antigen mimic. To achieve this, we have emphasized loop secondary structures for several reasons: (1) surface accessible loops are abundant in many protein antigens; (2) previous epitope mapping experiments have revealed loops as common antibody binding sites;^{10, 48, 110, 135} (3) loops are more amenable to nanocluster recapitulation when compared to other types of secondary structure. Surface accessible loops also lack steric interference and are highly solvated. Previously, cyclization of peptides has approximated loop structures with limited success,⁵⁰ but developing and presenting a peptide that reconstitutes a physiological conformation is paramount (Figure 28).¹³⁵ To this end, we have presented a conformational loop structure from the protective antigen of *B. Anthracis* in a bidentate fashion on the surface of Tiop-MPCs.

An example of a loop-rich protein is the protective antigen (PA) of *B. Anthracis*, which is one of three protein precursors to the anthrax toxin. Edema factor (EF) and

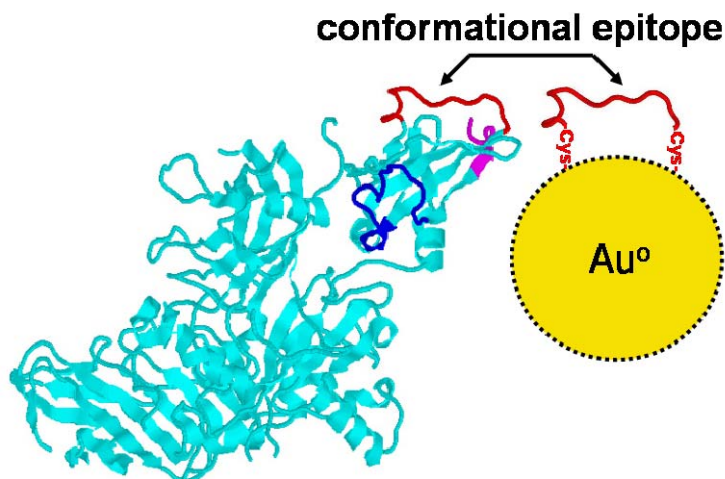


Figure 28. Crystal structure¹³⁵ of the protective antigen of *B. Anthracis* and cartoon of corresponding antigen mimic displaying a conformational loop structure that reconstitutes physiological conformation. Linear and loop epitopes are highlighted in red, blue, and magenta in the crystal structure.

lethal factor (LF) depend on PA for membrane transport and activation, making PA binding to the cell membrane crucial for toxicity.¹³⁵ PA has been a target for immunological studies, which have shown that levels of anti-PA antibodies correlate well with immunity to anthrax.¹¹⁰ Further examination has identified two loops and the c-terminus as cell receptor binding sites, and therefore, possible sites for toxin neutralization by IgG (Figure 28).^{110, 135-139} Recent studies¹⁴⁰ using denatured and non-denatured PA confirm the necessity of conformation in loop structures, but also suggest the presence of a linear epitope, such as the c-terminus. The identification of these loops and the high priority that anthrax has received due to its potential as a bioterrorism agent make PA an excellent model for the design of complex, conformational nanostructures that mimic an antigen and have the ability to interface with biological systems.

Antigen mimic design, by faithfully reconstituting the physiologically-relevant conformation of a peptide epitope on the surface of a monolayer-protected cluster, is

aided by intrinsic properties of the MPCs and their functionalization. One important feature of place exchange reactions and the presentation of conformational peptide epitopes is the idea that fast-exchange sites are not static. Evidence for this has come from the exchange of several different ligands onto the same MPC^{35, 141} and from an inability to completely remove ligands that had been previously exchanged onto a cluster.^{34, 35} A significant implication of these results is the ability of thiolates to migrate across the monolayer of an MPC. This migration might allow for the faithful reconstitution of a peptide epitope if the two ends of a bidentate ligand are able to move and position themselves at a distance similar to that in their physiological conformation. Appropriate reconstitution may also be limited by the nanoparticle diameter. Fortunately, the typical size of water soluble MPCs (2 – 6 nm diameter) is an excellent fit for the bidentate exchange of many peptide loops.

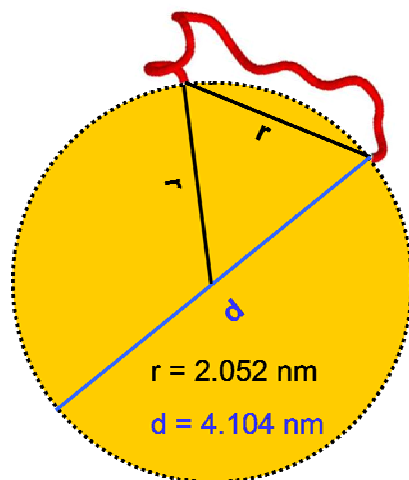


Figure 29. Calculation and cartoon suggesting that the optimal size of MPC for bidentate place exchange of an epitope loop (amino acids 679-693) from PA is 4.104 nm diameter, which is in the typical size range for water soluble clusters (2 – 6 nm).

For example, according to crystal structure measurements,^{123, 135} the anthrax PA680B epitope has a through space distance (from amino acid 679-693) of 2.052 nm in its native conformation. Calculations, assuming an equilateral triangle from points of attachment to the center of the cluster, suggest that an MPC with diameter of 4.104 nm would be optimal (Figure 29). Working in this size regime can help to ensure proper bidentate exchange and appropriate conformation. In this way, conformational, physiologically-relevant antigen mimics can be produced and compared to their linear counterparts (same primary sequence, different local conformation) in order to examine differences in antigenicity or immunogenicity using polyclonal antibodies or monoclonal antibodies.

One important application of high-affinity conformational antigen mimics may be in the area of epitope mapping. Epitope mapping is the process of determining the major antibody binding sites on an antigen and can provide valuable information to one who is attempting to understand an antigen's mode of action or produce an antiviral vaccine. There are established techniques for mapping an antigen, including Western Blot analysis, X-ray crystallography, NMR, antibody competition assays, site-specific mutagenesis, and flow cytometry.^{10, 138-140} Each of these techniques present their own advantages and disadvantages and tend to excel in one particular aspect of epitope mapping. Many of these experiments place emphasis on distinguishing between discontinuous epitopes, where contact points are far apart in amino acid sequence but proximal through space, and continuous epitopes that involve a sequential amino acid sequence.⁴⁸ Unfortunately, they often ignore the conformations intrinsic to sequential epitopes. Consequently, many mapping techniques lack the ability to maintain antigen secondary structure (local conformation) or ignore it entirely despite the tremendous

impact secondary structure can have on the location of contact points and, ultimately, antigenicity. Peptide epitopes are another tool for mapping sequential epitopes and have traditionally been used in the creation of synthetic peptide libraries and in phage display methods.^{6, 10} Again, these methods preclude the study of secondary structure, though they offer the best potential to incorporate conformation. Research herein has established a method for the study of secondary structure conformational effects on monoclonal antibody binding to peptide epitopes. According to this method we have effectively mapped monoclonal anti-protective antigen (anti-PA) antibodies to a protein conformational loop region through the assembly of a conformational loop epitope on a nanoparticle.

Epitope mapping using conformational antigen mimics requires the development of a sensitive, selective, quantitative assay that allows for 3D nanocluster substrates, multilayer adsorptions, and non-rigid biological recognition. The quartz crystal microbalance (QCM) has recently been demonstrated to be well-suited for this type of assay,^{2, 3, 49} has been used in the study of a variety of biological and non-biological systems,^{2, 52} and has numerous benefits over competing techniques for the study of nanoscale assembly.³ Through a quantitative QCM binding assay, this research demonstrates the accurate reconstitution of epitopes on a nanocluster and the effective conformational and linear epitope mapping of PA. Furthermore, it suggests these nanostructures as antigen mimics that have the potential to interact with specific immunological systems.

Other important factors in the study of linear and conformational antigen mimics are the immune response they illicit in an animal model (immunogenicity) as well as any

deleterious effects they may have (toxicology). This requires the use of an active immune system in living organisms, such as mice, and an antibody production assay. These types of assays are commonly used in monoclonal antibody production or vaccine development and typically use a range of different antigens, including killed organisms, live attenuated organisms, proteins, protein subunits, genes, and peptide epitopes.¹⁴² For example, several studies attempting to produce neutralizing anti-protective antigen antibodies have used recombinant PA protein,^{136, 138, 140, 143-145} subunits from the PA protein conjugated to glutathione-S transferase,¹³⁷ and DNA encoding for the PA protein.¹⁴⁶ Peptide epitopes, on the other hand, have not been used in anti-PA antibody production, though they have tremendous potential in vaccine development: they can be chemically synthesized and characterized, allowing for molecular definition; they are extremely stable as compared to their protein counterparts, due to limited conformation or folding; no infectious material is used in their assembly, causing limited toxicity problems; they can be easily coupled with other peptide epitopes or adjuvants to increase potency; they are highly programmable and can be easily configured to a specific epitope.¹⁴⁷ Due to their small size, intrinsic immunogenicity can be lacking,¹⁴⁸ though coupling the peptide epitope to a scaffold, typically a protein carrier such as KLH or BSA, can increase activity and, simultaneously, introduce an adjuvant.¹⁴⁷ While this conjugation technique has worked well for continuous, linear epitopes, it provides no means for introducing secondary structure or local conformation into the epitope, which has been suggested to be very important in many protein antigens.^{48, 142} An alternative scaffold would be MPCs, which have potential for the conformational presentation of peptide epitopes. These conformational nanoparticle antigen mimics could increasingly

stimulate the body's immune system into producing protective immunity against specific types of bacterial and viral infections.

One important consideration when introducing a novel material, such as nanoparticles, into a living organism would be that material's toxicological effects. Toxicity and the means for biological processing can be very important for the material's dose response, retention, and overall efficacy. There are relatively few examples in the literature of nanomaterial toxicology studies or even gold nanoparticle injection into mice. Existing studies use a variety of different gold nanomaterials, including citrate-reduced colloidal gold,¹⁴⁹⁻¹⁵¹ purchased Nanogold,^{152, 153} silica/gold nanoshells,¹⁵⁴ and nanorods.^{155, 156} These materials have sizes ranging from 1.9 to 130 nm in diameter and a variety of different surface functionalities. The majority of these studies are for the purpose of cancer treatment^{151, 152, 154} or *in vivo* imaging,^{153, 155, 156} but often include some information on toxicological effects. Paciotti, et al¹⁴⁹ injected 5 to 24 μg of citrate-reduced colloidal gold presenting PEG and TNF α intravenously into C57/BL6 mice with no ill effects. They were able to visualize cluster retention in the liver, spleen, and a colon carcinoma tumor over 5+ hours. Likewise, Hainfeld, et al¹⁵³ introduced 1.9 nm Nanogold at relatively high concentrations intravenously into BALB/c mice without morbidity. The LD₅₀ for this material was determined to be as high as 3.2 g Au kg⁻¹ body weight (67 mg Au for a typical 21 g mouse). Complete blood chemistry and hematology showed no abnormalities and pharmacokinetic information showed clearing of the blood in ~10 hr, though significant retention in the liver, kidneys, and tumor over 24 hr. While this is important and useful information for specific types of nanomaterials, it is likely to only loosely correlate to different materials of different sizes. There are no examples, to

my knowledge, of toxicology studies or antibody production assays using monolayer-protected nanoclusters. The difference in synthetic route, size, and composition for these nanomaterials may have a profound effect on toxicity and immunogenicity, suggesting the need for preliminary examination. This will elucidate the potential of conformational peptide epitope functionalized nanocluster antigen mimics as immunological materials or vaccines.

Experimental

Chemicals

Gold shot (99.99%) was purchased from precious metal vendors and was initially converted to $\text{HAuCl}_4 \cdot 3\text{H}_2\text{O}$ by boiling Au^0 in HCl/HNO_3 solution.¹¹⁹ N-(2-Mercaptopropionyl)-glycine (tiopronin, reagent), protein A (recombinant from *Escherichia coli*, >95%), bovine serum albumin (BSA, fraction V, 96%), and α -cyano-4-hydroxycinnamic acid (matrix grade, α -CHCA) were purchased from Sigma. Poly(diallyldimethylammonium chloride) (400,000-500,000 MW) (polyelectrolyte) was obtained from Aldrich. Ellman's reagent was purchased from Pierce Biotechnology. Anti-PA mouse monoclonal antibodies were purchased from Biodesign International. Anti-HA antibodies were purchased from Vanderbilt Molecular Recognition Core Facility. Protective Antigen protein (83 kDa, recombinant) was purchased from Alpha Diagnostic International. Pooled Normal Human Serum (male) was purchased from Innovative Research, Inc. NMR solvents were obtained from Cambridge Isotope Laboratories and water was purified using a Modulab Water Systems unit (~18 M Ω).

Buffers were prepared according to standard laboratory procedure. Other chemicals were reagent grade and used as received.

Antigen Mimic Synthesis and Characterization

Peptide epitopes were synthesized according to standard continuous flow fmoc solid-phase peptide synthesis methods on an Advanced Chemtech peptide synthesizer, purified by reversed-phase HPLC, and lyophilized as previously described.^{49, 157} Identity of peptides was confirmed by MALDI mass spectrometry.

Nanometer-sized gold MPCs were synthesized with tiopronin as the passivating substrate, as previously described.^{31, 39, 49} Characterization of MPCs was completed using nuclear magnetic resonance spectroscopy, UV/visible spectroscopy, transmission electron microscopy, and thermogravimetric analysis, as previously described.^{2, 49}

Equilibrium place exchange reactions between tiopronin-MPCs and solution thiols were performed according to Hostetler, et al.³⁴ For initial epitope mapping experiments, nanocluster was co-dissolved in DI water (final concentration of 3.0 mg/mL MPC) with free thiolated peptide in a 25:1 (mol/mol) ligand/peptide ratio. Solutions were stirred at room temperature for approximately 4 days, collected, and purified by dialysis.^{2, 49} In preparing conformational antigen mimics for mouse immunization, exchange was upscaled to produce large amounts of functionalized cluster. In this case, nanocluster was co-dissolved in DI water (final concentration of 1 or 2 mg/mL MPC) with free thiolated peptide in a 15-25:1 (mol/mol) ligand/peptide ratio. Solutions were stirred at room temperature for approximately 3 days, collected, and purified by dialysis. Extent of place exchange was determined by ¹H NMR⁴⁹ and by iodine reaction.³⁵ In the case of the

iodine reaction, ~20 mg of mixed monolayer MPC were co-dissolved with 10 mg I₂ in 10 mL DI water and stirred for several hours. After centrifugation of the iodine-passivated nanoclusters, the supernatant was removed, lyophilized, and examined via ¹H NMR. In order to determine the extent of exchange, in either case, peak assignments had to be made in the free and MPC-bound peptide. To facilitate this, total coherence spectra (TOCSY) of 1 mM peptide in D₂O and 90% H₂O/D₂O were taken of one peptide using a DPX-400 instrument at 400 MHz.

Characterization of Epitope Conformation

Bidentate place exchange reactions were attempted using peptides with Cys residues at both ends in order to reproduce a conformational loop structure. Evaluation of the attachment, to determine if a bidentate structure was achieved, was performed according to several analytical techniques.

Nuclear Magnetic Resonance. ¹H NMR was completed as above to obtain integration values and peak widths.

Circular Dichroism. AVIV Circular Dichroism Spectrometer Model 215 was used to collect CD spectra of monodentate and bidentate free peptide and MPC-associated peptide. Peptides were dissolved in 10 mM pH 6.0 phosphate buffer and in equal parts phosphate buffer and trifluoroethanol. Monodentate peptide was 21.6 μM and bidentate was 19.7 μM. Free tiopronin was 68 μM in phosphate buffer. Monodentate (1.56 mg/mL) and bidentate (0.78 mg/mL) peptide-MPC were diluted to have the same concentration of peptide displayed to solution. All samples were scanned from 260 to 190 nm.

MALDI-TOF Mass Spectrometry. Mass spectra were taken on a PerSeptive BioSystems Voyager-DE STR instrument run in reflector mode with low mass gate, grid voltage of 74.5%, and laser intensity between 2200 and 2450. Peptide was dissolved in aqueous 0.05% TFA, spotted on a gold MALDI plate, and let dry. α -cyano-4-hydroxycinnamic acid matrix was then spotted on top of the peptide and allowed to crystallize.

Derivatization with Ellman's Reagent. Ellman's Reagent (ER) is a dithiol that becomes a strong chromophore upon reduction of the disulfide bond. If one end of the bidentate peptide were not attached to the MPC, its thiol would be available to react with ER, thus derivatizing and marking the lack of bidentate exchange. ER was reacted with both free peptide and peptide-MPC and analyzed by ^1H NMR and MALDI-MS as above. Free, monodentate peptide was reacted with excess ER in 100 mM pH 8.0 phosphate buffer for 15 min. Peptide was then purified via preparative HPLC as above and analyzed. Peptide-MPC was reacted with excess ER in phosphate buffer for 15 min. Unreacted ER was removed by dialysis (above) and peptide-MPC was analyzed. Peptide-MPC then underwent reaction with iodine (above) and the organic components were collected. Excess iodine and tiopronin were separated from peptide with a Sep-Pak Cartridge Light C18 column. The cartridge was rinsed with methanol and aqueous 0.05% TFA before sample loading. Iodine and tiopronin were eluted with excess aqueous 0.05% TFA. Peptide was then eluted with small amounts of a 50/50 mixture of water and acetonitrile (both 0.05% TFA) and 100% acetonitrile (0.05% TFA). Collected fractions were inspected spectroscopically and fractions containing peptide were lyophilized and analyzed via ^1H NMR and MALDI-MS.

Quartz Crystal Microbalance

Binding events were followed with QCM as previously detailed.^{2, 3} Three different immunosensor assemblies were studied and used for the detection of antibody. The first assembly consisted of a purchased 5 MHz QCM crystal with Au electrode, polyelectrolyte, and MPC antigen mimic. To assemble this immunosensor, the Au electrode was first cleaned with piranha and ozone as previously described (CAUTION: handle piranha solutions with care).² The crystal was then mounted in the holder/flow cell, rinsed with 50 mM pH 7.2 phosphate buffer (PB), and brought to resonant frequency. A constant flow of 28 $\mu\text{L}/\text{min}$ was used through this assembly procedure. Polyelectrolyte (0.05%) in PB was then pumped through the flow cell for 15 min. After a 10-min rinse with PB, MPC (2.4 μM) in PB was pumped for 30 minutes. Again the crystal was rinsed with PB for 10 min and was followed by BSA (16 μM) for 20 min. After a 10 min rinse with PB, the sensor was ready for antibody binding. Antibody binding to antigen mimics was completed by introducing antibody for a set time of 10 min at a constant flow of 28 $\mu\text{L}/\text{min}$. Maximum adsorption values were recorded after unbound antibody was rinsed out of the flow cell. Initial antigen mimic screening assays used one immunosensor for the binding of no more than two different antibodies, each at a concentration of 124 nM in PB. If the first Ab showed adsorption, a new immunosensor was assembled before further Ab addition. If the first Ab showed no adsorption, a second Ab was introduced. In this case, Ab was thoroughly rinsed out of the flow cell before the second antibody was introduced. Concentration dependent studies for both the antigen mimic and the intact protein antigen used a range of concentrations and a newly prepared immunosensor for each concentration. Control

experiments were conducted as above and newly prepared immunosensors were used for each sample. Later experiments used optimized fluidic systems (Cole-Parmer Masterflex 4 channel peristaltic pump with 0.25 mm ID santoprene tubing), allowing for faster flow rates and shorter flow times (detection times). Pooled human sera were also used as a blocking agent in mouse sera studies in an attempt to limit non-specific adsorption.

Antibody binding to nanocluster was also attempted using a covalent strategy for MPC immobilization. SAMs were formed out of dithiol ligands and MPCs were place exchanged onto the SAM surface. Two different SAMs were studied: a single monolayer of 1,6-hexanedithiol (HDT) and a mixed monolayer of 50/50 (mol/mol) HDT and β -mercaptoethanol (BME). SAMs were formed in ethanol overnight then rinsed in ethanol and DI water. In initial experiments, Tiop-MPC was then reacted with the surface at 0.1 mg/mL in DI water for 2-3 days. QCM crystals with SAMs only and with SAM-MPC structures were initially characterized by Atomic Force Microscopy (Veeco Digital Instruments, Nanoscope IIIa using a monolithic Si tip with 300 kHz resonant frequency and 40 N/m force constant). Further experiments using Tiop-MPC (0.5 mg/mL) involved place exchange onto HDT/BME SAMs and subsequent examination of non-specific binding using PBS and purchased pooled normal human serum (CAUTION: Biohazard). Similar sensors were then assembled using Tiop-MPC presenting conformational PA peptides. PA-MPC was place exchanged onto SAMs for 1-11 days and sensors were examined for antibody binding, reusability (regeneration), and for non-specific binding (using anti-HA and anti-RSV antibodies).

Antibody binding to the intact protein, protective antigen (PA), was achieved through the assembly of an immunosensor consisting of a 5 MHz QCM crystal with Au electrode,

PA, and BSA. After cleaning, mounting, and rinsing the crystal it was brought to resonant frequency. A constant flow of 28 $\mu\text{L}/\text{min}$ was used through the assembly. PA (96 nM) in PB was introduced for 15 min and was followed by PB rinse for 10 min. BSA (16 μM) was then introduced for 15 min. After a 15-min rinse with PB, the sensor was ready for antibody binding. Antibody binding to the intact protein antigen was completed by introducing antibody for a set time of 10 min at a constant flow of 28 $\mu\text{L}/\text{min}$. Maximum adsorption values were recorded after unbound antibody was rinsed out of the flow cell.

Surface Plasmon Resonance Spectroscopy

SPR measurements were made using a Biacore 3000 instrument. Bare Au sensor chips were used in antibody detection strategies and were cleaned with piranha (as above) before use. A custom program was written for the detection of antibody binding to antigen mimic and was repeated sequentially to obtain binding data at several antibody concentrations. Flow was set at 50 $\mu\text{L}/\text{min}$ through all channels, consecutively, and the detection mode was set to all four channels with no reference. The following sequence was then begun: 50 mM NaOH 2 min; wait 1 min; 2.5 M NaCl 2 min; wait 1 min; 50 mM HCl 2 min; wait 1 min; change flow to 30 $\mu\text{L}/\text{min}$; wait 1 min; 0.05% polyelectrolyte in PBS 3 min; wait 1 min; 1 mg/mL MPC in PBS 3 min; wait 2 min; 1 mg/mL BSA in PBS 2 min; wait 2 min; antibody in PBS 2 min; wait 2 min. Both MPC and antibody were potentially varied with each cycle.

CM-5 sensor chips were used for the detection of antigen mimic. Antibody was amide coupled to the dextran-coated chip using standard EDC/NHS techniques. For

coupling experiments the flow rate was set at 10 $\mu\text{L}/\text{min}$. EDC (0.4 M) and NHS (0.1 M) were mixed prior to injection. Activation lasted for 7 min and was followed by washing with PBS. Antibodies were dissolved at 40 $\mu\text{g}/\text{mL}$ in 10 mM acetate buffer at pH 4.5 and injected for 5 or 10 min. Flow cell 1 was exposed to no antibody, flow cell 2 to antibody 110 (10 min), flow cell 3 to anti-ebola glycoprotein 6D11 (5 min), and flow cell 4 to antibody 110 (5 min). After rinsing with PBS, excess ethanolamine was injected for 7 min to quench any remaining activated carboxylic acid groups. Nanocluster was then analyzed by setting the flow rate to 30 $\mu\text{L}/\text{min}$ and using the following references: FC2-FC1 and FC4-FC3. Antigen mimic was then injected for 2 min and was followed by regeneration with 2.5 M NaCl for 30 s at 60 $\mu\text{L}/\text{min}$. A different mimic or concentration of mimic was injected with each cycle. Concentrations ranging from 0.001 to 1.0 mg/mL were used.

Mouse Antibody Production

Antibody production using conformational peptide epitope functionalized nanoclusters required 34 Balb/c, female, 6 week old mice (Harlan, Indianapolis). Mice were injected on three days, each day separated by two weeks. On the injection day, each mouse was injected twice: 200 μL intraperitoneal (peritoneal cavity) and 200 μL subcutaneous (skin on back of neck). A summary of injection groups and concentrations is available in Table 9. All experimental protocols using animals were approved by Vanderbilt University Institutional Animal Care and Use Committee (M/05/235). Nanoparticles were prepared as described above and had compositions as listed in Table 6 (A2, E, G). All solutions were sterile filtered before injection. Control injections

involved the introduction of the linear PA peptide (PA680M) via a keyhole limpet hemocyanin (KLH, Pierce Biotechnology) carrier. KLH (1.2 nmol) was co-dissolved with sulfo-SMCC (108 nmols, Pierce Biotechnology) in PBS, vortexed, and reacted for 30 min at room temperature. Purification of unbound sulfo-SMCC was achieved by Centricon 5000 MWCO spin filter (three washes, centrifuged at 4000 rpm). PA680M peptide (180 nmols) was added to the purified KLH-sulfo-SMCC, vortexed and reacted for 30 min at room temperature. Purification was completed as above. The washes, containing unbound PA peptides, were collected and concentration was determined by absorbance at 280 nm (using a standard curve). Four weeks after the last injection, blood was collected via the saphenous vein. Approximately 100 μ L of whole blood was collected per mouse. After waiting for coagulation to occur, samples were centrifuged at 10000 rpm for 15 min. The supernatant was collected and stored at either 4 °C (short term) or -80 °C (long term). Sera samples were analyzed by ELISA (below) or QCM, as previously described.

Mice that expired after the initial injection were dissected for examination and collection of heart, lungs, spleen, and liver tissue. Tissue was briefly examined for pathological abnormalities (H. Mok) and examined for gold content. Tissue from one mouse was homogenized in a ground glass apparatus using minimal amounts of aqueous NaOH (20 mM). Samples were centrifuged at 4500 rpm and supernatants were collected. Samples were analyzed by energy dispersive x-ray spectroscopy (EDAX) using a Philips CM-20 TEM operating at 200 keV and 30,000 x magnification. Blank grids were used as a control and the same volume of sample was spotted onto clean grids for each experiment.

Enzyme-linked Immunosorbant Assay

ELISA was used to initially screen mouse sera samples versus the PA protein, HA protein, or antigen mimics. Checkerboard experiments using the PA protein and anti-PA antibody (antibody 110) were conducted to determine optimal conditions. Immulon well-plates were used in all cases. Experiments against the PA protein used 400 or 500 ng of antigen per well (in PBS), blocking with 1 mg/mL BSA, sera diluted to 1:10, 1:100, or 1:1000 in PBS, secondary antibody (goat anti-mouse HRP conjugate) diluted 1:5000 in PBS, and washing with PBS/T (50 mM PB, 150 mM NaCl, 0.01% tween-20) between each step. The HRP substrate TMB (3,3',5,5'-tetramethylbenzidine) was then introduced and followed by 0.5 M H₂SO₄. Absorbance was read at 450 nm. Experiments against the HA protein used similar conditions except for the use of 100 ng of protein per well and 1:100 dilution of sera. Experiments against the PA680B-MPC antigen mimic used similar conditions, except for the use of 1 µg of nanocluster per well and 1:100 dilution of sera.

Results and Discussion

Antigen Mimic Synthesis and Characterization

The results of this study demonstrate an ability to assemble conformationally relevant antigen mimics and use them in the epitope mapping of a potential bioterrorism agent. Traditional mapping techniques place emphasis on discontinuous conformational or continuous linear epitopes but have overlooked the local conformation or secondary structure present in peptides longer than eight amino acids. Continuous conformational

peptide epitopes offer a potential for enhanced antigenicity, as well as immunogenicity, and deserve the attention of those mapping antigens and designing vaccines. This research shows reconstitution of loop structures from the protective antigen of *B. Anthracis* on the surface of monolayer protected clusters to produce linear and conformational antigen mimics.

Peptide epitopes found in Table 5 were synthesized for presentation on MPCs. Cys residues were added at the N- and/or C-terminus to promote bidentate or monodentate exchange and Ala residues were similarly added for a lack of reactivity or presentation. Concurrently, water-soluble, nanometer-sized, monolayer-protected clusters were synthesized with tiopronin, a glycine derivative, as the passivating ligand, as previously reported.^{2, 44} Careful characterization allowed for the calculation of an average diameter, compositions, and molecular weight (Table 6, according to established methods, see Chapters II and III). The epitope and MPC scaffold were then brought together through place exchange reactions to produce functional nanostructures.^{34, 35}

Table 5. Amino acid sequences for peptides used in antigen mimic design. Highlighted Cys and Ala (red) were not part of the epitope, but added for functionalization and immobilization purposes.

Peptide	Sequence	MW, Da	Reference
PA680B	C KYNDK LPLYI SNP C	1771	110, 135-138, 140
PA680M	KYNDK LPLYI SNP C	1668	110, 135-138, 140
PA680A	AA KYNDK LPLYI SNP A	1778	110, 135-138, 140
PA703B	C KENTI INPSE NGDTS TNGIK C	2339	110, 135-137
PA730M	C KGYEI G	769	138

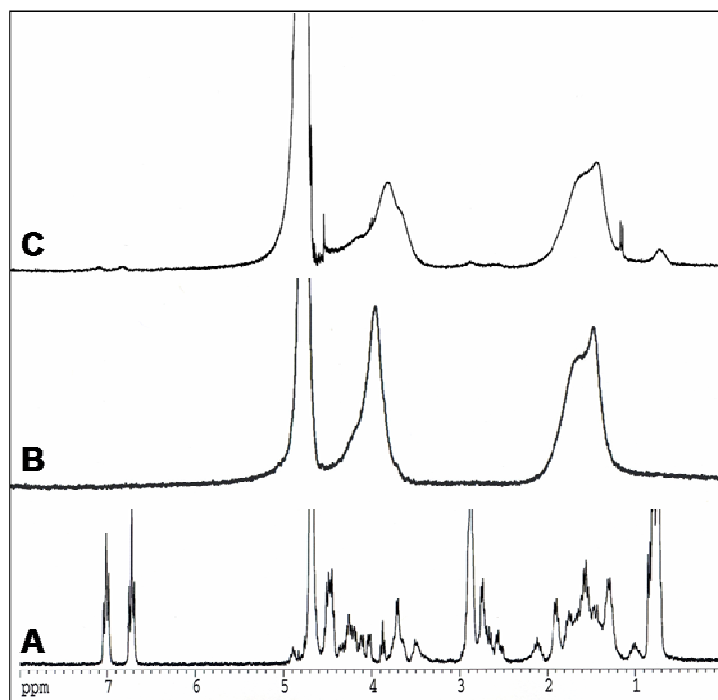


Figure 30. ^1H NMR of (c) free PA680B peptide, (b) pure Tiop-MPC, and (a) peptide presenting MPC, showing successful peptide presentation.

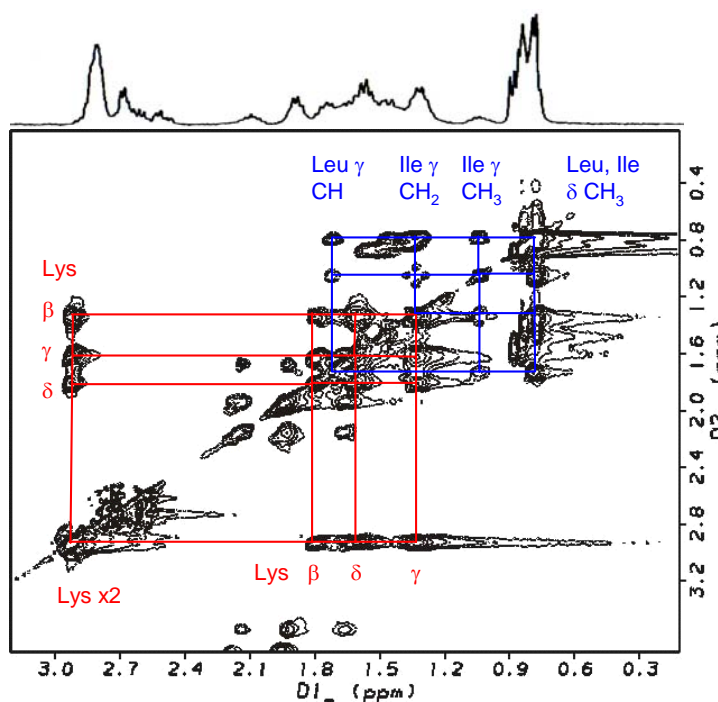


Figure 31. 2D TOCSY of synthetic peptide (PA680M) and corresponding proton 1D spectra (above), highlighting peak assignments.

Following each exchange, the extent of presentation was determined by ^1H NMR, as previously described (Chapter III).⁴⁹ Representative ^1H NMR for the free peptide PA680B, Tiop-MPC, and peptide-presenting MPC (PA680B-MPC) are available in Figure 30. Quantitative determination of peptides on an MPC is obtained through the ratio of integration values of peaks indicative of tiopronin and of peptide. Knowledge of the number of protons that are associated with an individual peak is, therefore, essential to a correct ratio. In order to facilitate peak assignment in the peptide PA680M, total coherence spectroscopy (TOCSY) was performed (Figure 31). TOCSY is a 2D NMR experiment that transfers magnetization between ^1H spins that are connected by any number of scalar couplings. The strength of the coupling decreases as the number of transfers increases, but strong cross peaks do arise through as many as three or four bonds.¹⁵⁸ Through these cross peak correlations it is possible to make peak assignments and obtain values of 15 protons for the peak at ~ 0.8 ppm, 4 protons for the peak at ~ 2.9 ppm, 4 protons for the peak at ~ 6.7 ppm, and 4 protons for the peak at ~ 7.0 ppm. This has allowed accurate determination of peptide presentation, which in most cases has been confirmed by an iodine kill reaction. A cartoon schematic and final composition of all antigen mimics used in the following studies are available in Figure 32 and Table 6, respectively.

Table 6. Final composition of antigen mimics used in the following experiments. A₂ was used in mice experiments only, while A₁ was used in all other studies. ⁴HA peptide comes from the hemagglutinin protein of influenza (see Chapter III).

Peptide	MPC Diameter, nm	Attachment	Composition
(A ₁) PA680B	3.5 ± 1.0	Conformational	Au ₈₀₇ Tiop ₂₉₀ Pep ₄
(A ₂) PA680B	3.1 ± 1.0	Conformational	Au ₅₆₁ Tiop ₁₅₀ Pep ₇
(B) PA680M	3.5 ± 1.0	Linear	Au ₈₀₇ Tiop ₂₉₄ Pep ₄
(C) PA703B	3.5 ± 1.0	Conformational	Au ₈₀₇ Tiop ₂₈₂ Pep ₈
(D) PA730M	3.5 ± 1.0	Linear	Au ₈₀₇ Tiop ₂₈₈ Pep ₁₀
(E) ⁴ HA	3.1 ± 1.0	Linear	Au ₅₆₁ Tiop ₁₅₆ Pep ₈
(F) none	3.5 ± 1.0	Control	Au ₈₀₇ Tiop ₂₉₈
(G) none	3.1 ± 1.0	Control	Au ₅₆₁ Tiop ₁₆₄

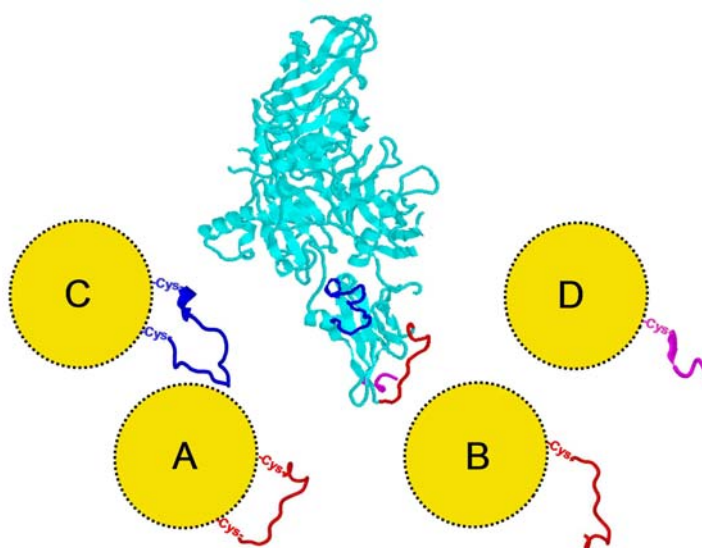


Figure 32. X-ray crystal structure¹³⁵ of the protective antigen of *B. anthracis* (middle) and cartoons of PA mimics highlighting the conformational and linear epitopes. Three known epitopes are highlighted in the crystal structure: amino acids 680-692 (red), 703-722 (blue), 730-735 (magenta).^{110, 135-138, 140}

Characterization of Epitope Conformation

The faithful reconstruction of epitope loops in a physiologically-relevant conformation is predicated on the ability to assemble loop peptides in a bidentate fashion.

A linear epitope, such as the c-terminus of PA (PA730M), can easily be attached to the

MPC in a monodentate fashion, which will afford the peptide a good chance of maintaining its correct conformation. On the other hand, peptide epitopes that come from flexible loop regions of proteins cannot suffer monodentate attachment and be expected to adopt the correct conformation. Immobilizing both ends of the peptide in a bidentate, bivalent mode restrains the peptide and promotes a conformation comparable to its native form. This is not an attempt to “fold” a peptide, only an attempt at placing the peptide in an environment similar to that of the intact protein. One challenge was in the characterization of the mode of attachment. The diversity of particle size can affect loop attachment, creating a large combinatorial set of epitope conformations. Techniques like circular dichroism and two-dimensional NMR have been successful in evaluating peptide conformation. Using CD spectroscopy, free peptide was determined to be in a random coil conformation, with peak at ~197 nm, and was shifted to higher wavelength upon the addition of trifluoroethanol, which promotes helicity. Peptide-MPCs did not exhibit random coil characteristics, suggesting some sort of associated conformation. Unfortunately, low concentration of peptide on the surface of the MPC, cluster absorbance, and characteristically broad NMR peaks limit CD and NMR applicability to this study.

Instead, the mode of peptide attachment to the nanocluster was probed with a free thiol labeling molecule, Ellman’s Reagent (ER).¹⁵⁹ Incubation of PA680B-MPC (**A₁**) with Ellman’s Reagent would cause thiol labeling if one end of the peptide loop was attached to the MPC and the other thiol was otherwise free. Reacting ER with free peptide PA680M produced a characteristic yellow color and, after purification, showed

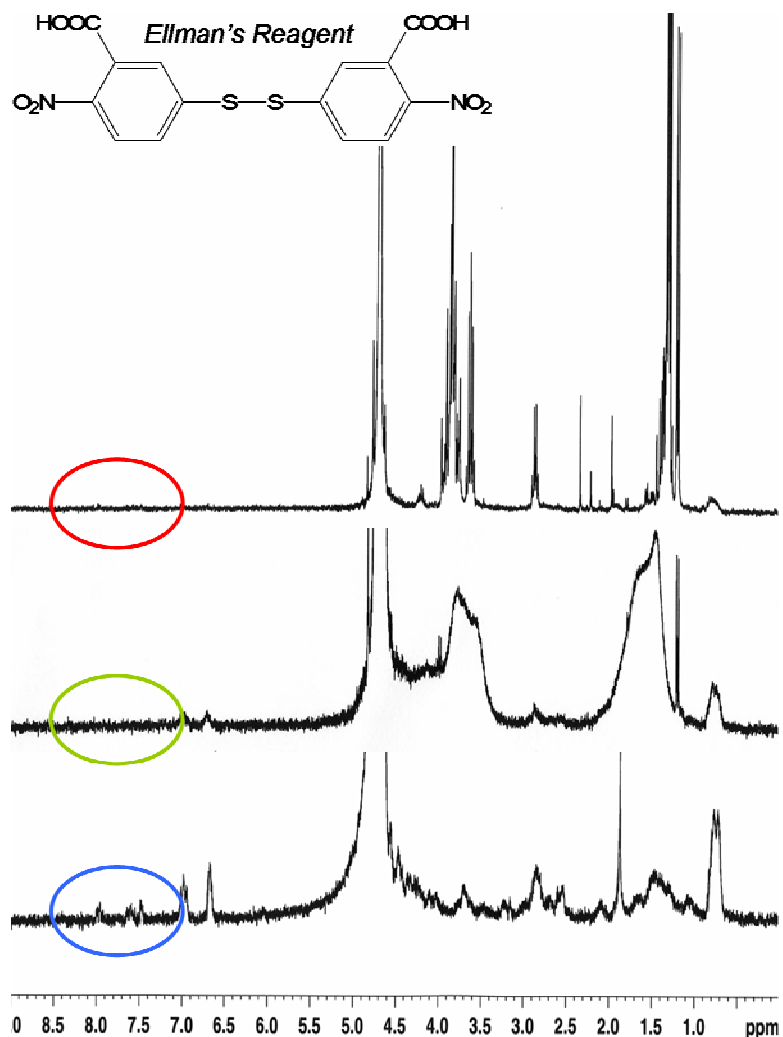


Figure 33. ^1H NMR of Ellman's Reagent derivatized free peptide (PA680M), showing aromatic peaks (circled blue). Similar derivatization of PA680B-MPC (circled green) and PA680B-MPC after isolation of ligands only (circled red) show no peaks in that region.

thiol derivatization in ^1H NMR and MALDI-MS. Conversely, reacting ER with PA680B-nanocluster complex (A_1) resulted in no indication of derivatization, as seen in Figure 33. Labeling experiment with Ellman's Reagent have supported bidentate attachment by indicating a lack of free, unattached thiol in an MPC solution, but provide no information on conformation. A further test of epitope conformation was to show a difference in antibody binding to linear versus conformational antigen mimics.

Epitope Mapping

A sensitive and selective immunosensor involving a QCM quartz crystal with gold electrode and the sequential layering of a polyelectrolyte,^{75, 76} MPC, and blocking with BSA, leading to the immobilization of antigen mimics, provided a foundation for antibody screening. Representative adsorption and average binding results of polyelectrolyte (0-30 min), MPC (30-60 min), and BSA (80-100 min) can be seen in Figure 34 and Table 7, respectively.

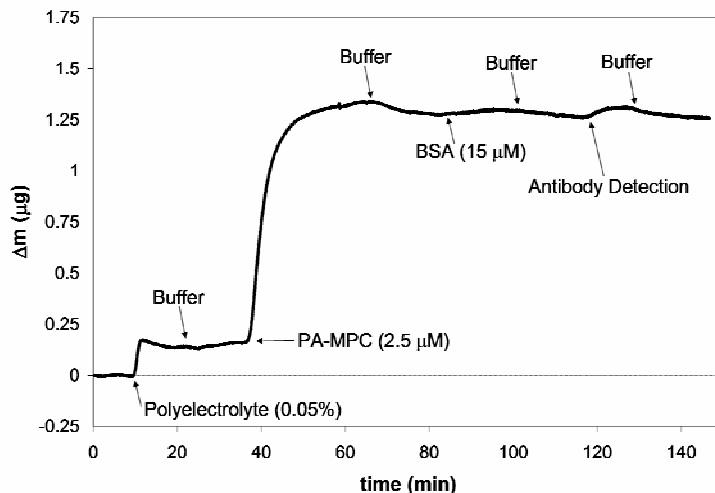


Figure 34. Representative polyelectrolyte, PA680B-MPC, BSA, and antibody 110 binding in phosphate buffer.

Binding studies involved seven mouse monoclonal anti-PA antibodies obtained from Biodesign International that were known to bind both the full-sized PA (83 kDa) and the furin-cleaved PA (63 kDa) (according to Western Blot), but had not been tested for ability to neutralize the toxin.¹⁶⁰ These antibodies were screened at constant concentration against the four PA mimics in order to map the antibodies to different

Table 7. Results of immunosensor assembly (in μg) and for screening monoclonal anti-PA antibodies (124 nM) against four antigen mimics (in ng). Screening was completed using QCM and all values represent changes in mass. Data suggests antibody 110 as having strong and specific interaction with PA680B-MPC (**A**₁).

	(A)	(B)	(C)	(D)
<i>Ave</i> PolyE	0.16 ± 0.03	0.16 ± 0.03	0.16 ± 0.03	0.16 ± 0.03
<i>Ave</i> MPC	1.12 ± 0.06	0.80 ± 0.07	0.73 ± 0.06	0.68 ± 0.07
<i>Ave</i> BSA	0.06 ± 0.05	0.13 ± 0.05	0.14 ± 0.02	0.21 ± 0.02
mAb 110	20	10	0	0
mAb 201	15	0	10	14
mAb 301	0	10	0	0
mAb 410	10	0	10	16
mAb 501	10	10	0	11
mAb 601	10	10	0	10
mAb 613	13	0	10	10

conformational and linear regions of the antigen. At a relatively low concentration (124 nM) of antibody, screening experiments provided qualitative information on recognition or lack of recognition and guided further studies (Table 7). The results of the screening experiments suggest cross reactivity for several antibodies, though antibody 110 was identified as being potentially selective for the conformational epitope spanning amino acids 680-692.

Monoclonal Antibody Binding

Monoclonal antibody 110 was studied in more detail using a QCM immunosensor similar to that used in the epitope mapping experiments and by varying the concentration of antibody and the ionic strength of buffers. Seven experiments for each of two antigen mimics (PA680B-MPC **A**₁ and PA680M-MPC **B**) differing only in mode of peptide attachment (bidentate vs monodentate) showed saturation of the immunosensor. The four highest concentrations for each mimic were fit to a logarithmic curve (Figure 35).

Table 8. Results from equilibrium calculations for two antigen mimics and the protective antigen protein. Experiments were conducted in phosphate buffer (no added NaCl) or in phosphate buffered saline (150 mM NaCl). ^aEquilibrium constant calculated from kinetic constants, where $K_a = k_f/k_r$. ^bCalculated from SPR experiments. ^cUnable to calculate due to a lack of binding.

Antigen	[NaCl], mM	Equilibrium Constants K_a ($\times 10^6 \text{ M}^{-1}$)
MPC-PA680B (A₁)	0	5.9 ± 0.7
	0	^a 4.0 ± 0.8
	150	2 ± 1
	150	^b 1.1 ± 0.2
MPC-PA680M (B)	0	2.6 ± 0.9
	150	^c --
Protective Antigen	0	12 ± 6

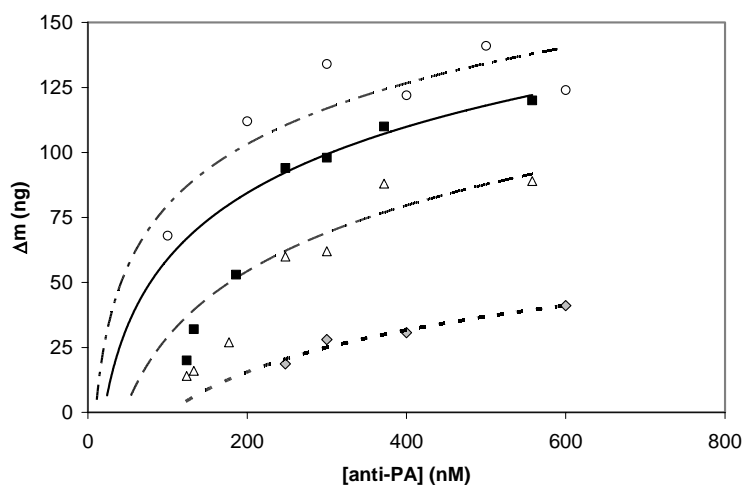


Figure 35. Plot of Δm against [anti-PA 110] for PA protein antigen (circle) with non-linear (long/short dashed line), MPC-PA680B (square) with non-linear fit to the four highest concentrations (solid line), MPC-PA680M (triangle) with non-linear fit to the four highest concentrations (long dashed line), and MPC-PA680B (diamond) in PBS with logarithmic fit (short dashed line) showing saturation of the immunosensor in all cases.

Equilibrium association constants (K_a) were determined for each mimic by fitting the four highest concentrations to a Langmuir adsorption isotherm (Table 8).^{2, 3} PA680B-

MPC (**A**₁) had a K_a of $(5.9 \pm 0.7) \times 10^6 \text{ M}^{-1}$, which falls within a general range for immuno-affinity of $10^6 - 10^{10} \text{ M}^{-1}$ and shows an increased affinity over a previously reported glutathione-presenting nanocluster with polyclonal antibody ($K_a = 3.6 \times 10^5 \text{ M}^{-1}$).² Antibody 110 had a decreased affinity for the linear epitope-presenting nanocluster (PA680M-MPC (**B**), $K_a = (2.6 \pm 0.9) \times 10^6 \text{ M}^{-1}$) suggesting a real difference between peptide epitopes of identical primary structure but different secondary structure.

These results were validated by control experiments using Tiop-MPC (**F**) and buffer of increasing ionic strength (Figure 36).

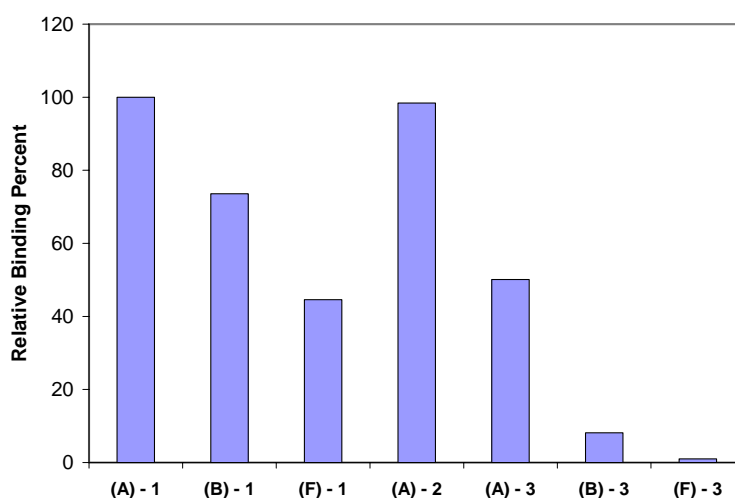


Figure 36. Relative binding percent for 300 nM 110 antibody to seven different nanocluster systems, normalized to density of nanocluster displayed on immunosensor surface. All samples were run in 50 mM phosphate buffer with varying concentrations of NaCl (1 = 0 mM, 2 = 50 mM, 3 = 150 mM).

Salt gradients are typically used in affinity chromatography and are known to decrease weak non-covalent interactions.¹⁶¹ In initial studies, the background antibody binding to Tiop-MPC (**F**) and PA680M-MPC (**B**) in 50 mM phosphate buffer was relatively high.

The addition of 150 mM NaCl decreased weak, non-specific adsorption seen in Tiop-MPC (**F**) and PA680M-MPC (**B**), but had a significantly lower effect on PA680B-MPC (**A₁**). Furthermore, the addition of only 50 mM NaCl had essentially no effect on antibody binding to PA680B-MPC (**A₁**). This allowed for the study of concentration dependence of antibody 110 binding to PA680B-MPC (**A₁**) in high ionic strength buffer. Here the association constant ($K_a = (2 \pm 1) \times 10^6 \text{ M}^{-1}$) was only slightly less than that calculated in low ionic strength (Figure 35, Table 8), confirming strong recognition and limited non-specific adsorption.

Kinetic information calculated for PA680B-MPC (**A₁**) ($k_f = (9 \pm 2) \times 10^3 \text{ M}^{-1}\text{s}^{-1}$ and $k_r = (2.3 \pm 0.5) \times 10^{-3} \text{ s}^{-1}$) from the time-dependent binding curves supports the equilibrium data and the immunorecognition of conformational mimics by antibodies. The equilibrium adsorption constant, K_a , is equal to the ratio of k_f/k_r and was calculated to be $(4.0 \pm 0.8) \times 10^6 \text{ M}^{-1}$, which correlates well with the K_a found in the previous method (Figure 35, Table 8). Kinetic constants relate to the kinetics of polyclonal antibody binding to glutathione-MPC, where $k_f = 5.4 \times 10^1 \text{ M}^{-1}\text{s}^{-1}$ and $k_r = 1.5 \times 10^{-4} \text{ s}^{-1}$.² It is reasonable that this forward rate constant is less than the forward rate constant for monoclonal anti-PA antibody due to the heterogeneity of the polyclonal anti-GSH sample. The binding kinetics for snake neurotoxin α -bungarotoxin to synthetic peptide mimitopes have been reported¹¹⁴ with k_f in the range of $10^1 - 10^4 \text{ M}^{-1}\text{s}^{-1}$ and k_r in the range of $10^{-3} - 10^{-4} \text{ s}^{-1}$. The kinetic rate constants for monoclonal antibody 110 binding to PA680B-MPC (**A₁**) also fall within these ranges.

Antibody binding to intact protein antigen was studied for comparison with the antigen mimics. Antibody was shown to specifically bind the protein in PB with a K_a

value slightly larger than that calculated for the nanocluster antigen mimic (Figure 35, Table 8). The antibody did display high background adsorption to BSA in 50 mM phosphate buffer, but decreased in high ionic strength buffer, while antibody binding to PA was only slightly affected by an increase in ionic strength. Antibody binding at one concentration (300 nM) in PBS showed binding at a level consistent with a possible K_a of approximately $6 \times 10^6 \text{ M}^{-1}$ (rough extrapolation), which is only three times greater than that reported for PA680B-MPC in PBS. Furthermore, anti-HA antibody, which is not specific for PA, showed no binding to the PA protein in low ionic strength buffer. The similarity of antigen and antigen mimic K_a values points to the exceptional reconstitution of the conformational peptide epitope on the surface of the nanocluster.

Antibody 110 binding to a second, separate batch of PA680B-MPC (composition essentially identical to that of **A₁**) was examined using a covalent, rather than ionic, MPC immobilization strategy. A robust, covalent, synthetic sensor would allow for sensor regeneration and reusability as well as long term stability and storage. Immunosensor assembly involved the place exchange of soluble antigen mimics onto the QCM surface via dithiol intermediates. An HDT (1,6-hexanedithiol) SAM was self-assembled and Tiop-MPC (**F**) was place exchanged onto the surface in initial experiments. AFM was used to confirm attachment and suggested successful exchange according to variations in surface roughness (Figure 37). These Tiop-MPC presenting crystals were then used to study non-specific binding characteristics using pooled human sera at various dilutions in PBS. Results suggested that dilutions between 1/500 and 1/1000 gave acceptably low non-specific binding under these conditions. The next step was to immobilize PA680B-MPCs (**A₁**) that had been confirmed to be able to bind antibody 110 under standard

conditions (ionic, non-covalent immobilization procedure). Five crystals were functionalized with HDT and allowed to react with PA680B-MPC (A_1) for 3, 5, 7, 10, or 11 days in order to study the effect of place exchange time on sensor sensitivity.

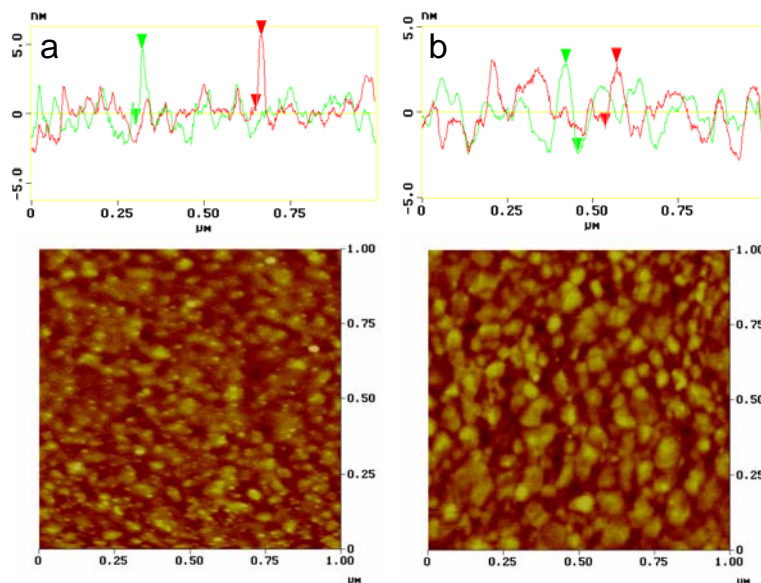


Figure 37. AFM measurement of (a) HDT SAM on gold QCM electrode, showing smooth surface with small features; (b) HDT SAM after place exchange with Tiop-MPC (F) on gold QCM electrode, showing roughened surface with larger, 3-5 nm height features.

Unfortunately, antibody 110 binding to all the sensors was minimal or similar to binding by non-specific antibodies (anti-HA or anti-RSV). Due to the length of time required for place exchange, it is difficult to know the actual amount of mimic presented on the QCM surface. It is thought that the slow kinetics of place exchange at a heterogeneous interface resulted in an unacceptable level of MPC density and an elevated limit of detection. Further progress in the area of covalent MPC immobilization is needed and may require a kinetically-favorable reaction, possibly involving amide coupling or a biotin/avidin interaction.

Surface plasmon resonance spectroscopy is a surface optical wave technique that is widely used in immunosensing. It has recently been compared to QCM in a number of different settings.^{2, 3} In order to further confirm the affinity of anti-PA antibody 110 for PA680B-MPC (**A**₁), SPR binding measurement were carried out on a Biacore 3000 instrument. Two binding methods were pursued. First, the standard polyelectrolyte immobilization of MPC was used to detect antibody binding. Since optical techniques can often be sensitive to molecules with high molar absorptivities, the MPC immobilization and antibody detection strategy was intended to limit these effects. At the beginning of each binding cycle the bare gold chip was rinsed with 50 mM NaOH, 2.5 M NaCl, and 50 mM HCl to remove any previously bound antibody or MPC. The

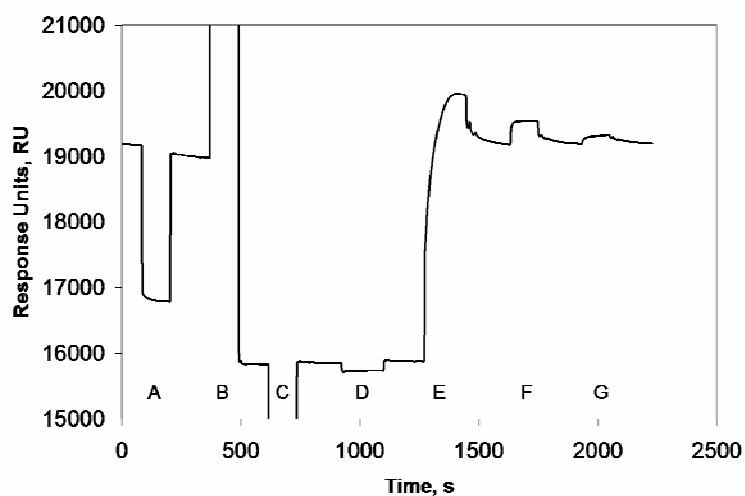


Figure 38. Representative SPR experiment involving chip washing, PA680B-MPC (**A**₁) immobilization, and antibody detection. (A) Washing with 50 mM NaOH; (B) washing with 2.5 M NaCl; (C) washing with 50 mM HCl; (D) polyelectrolyte adsorption; (E) PA680B-MPC adsorption; (F) BSA blocking of non-specific adsorption sites; (G) antibody binding and detection. Washing with PBS occurred between each step.

polyelectrolyte, MPC, and BSA layers were then assembled before introduction of the antibody. A representative sensogram for the assembly and detection is available in Figure 38. Various MPCs and antibody concentrations were used in each binding cycle. The results are available in Figure 39 and show significant binding of antibody 110 to PA680B-MPC in PBS, as expected. Binding appears to approach saturation at high concentrations and a detection limit of approximately 100 nM is observed, which is similar to QCM detection limits.

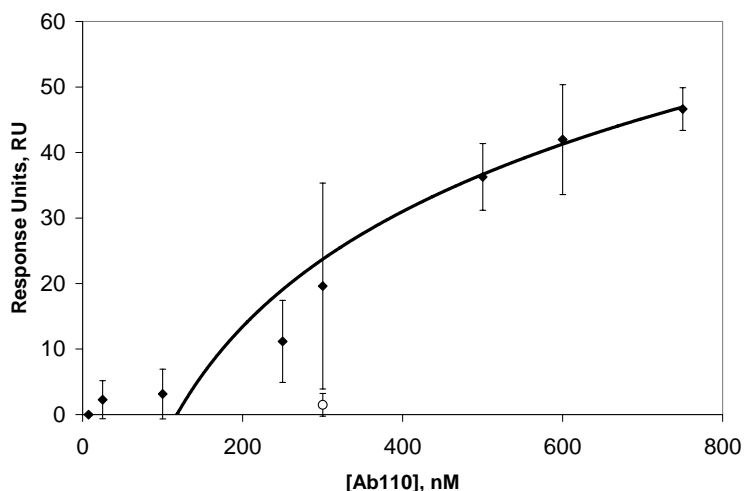


Figure 39. Plot of [Ab110] versus RU for binding to PA680B-MPC (**A1**) with a non-linear fit to the three highest concentrations. A control experiment (**○**) at 300 nM shows lack of binding to underivatized tiopronin MPC (**F**).

This data was used in the calculation of the equilibrium binding constant, where $K_a = (1.1 \pm 0.1) \times 10^6 \text{ M}^{-1}$ (Table 8). This agrees very well with the K_a calculated in QCM experiments, previously detailed ($2 \times 10^6 \text{ M}^{-1}$).⁵¹ Control experiments confirm specificity of this interaction as antibody 110 did not bind to underivatized Tiop-MPCs (**F**). The error bars on the graph (Figure 39) are relatively large and come from the average of the

four SPR flow cells. This might be indicative of intrinsic differences in each flow cell, differences in the layer assembly for each flow cell, or may result from MPC interference with optical detection.

The second SPR binding method involved the coupling of antibody to a CM-5 dextran chip and the attempted detection of nanocluster. Antibody was successfully amide coupled to the chip with final Response Units of 247 for FC1 (control), 5989 for FC2 (antibody 110), 2533 for FC3 (anti-ebola glycoprotein antibody), and 3937 for FC4 (antibody 110). Initial injection of MPCs showed refractive index changes of 20 to 100 RUs, suggesting possible interference with the optical measurements. While the Biacore 3000 instrument uses a light source at 760 nm, where nanoclusters have relatively low absorbance, a large refractive index change is not unlikely. Previous examples of nanocluster detection in SPR instruments plotted percent reflectance versus time,^{16, 72} rather than the angle of minimal reflectance versus time, which is common in Biacore instruments and may result in poor detection. Nanocluster detection made use of FC1 and FC3 as reference cells, allowing for the subtraction of non-specific refractive index changes. While subtraction seemed to work well, binding was only minimally detected (S/N ~ 2) at the highest concentrations of antigen mimic (1 mg/mL), resulting in a high detection limit and a lack of data for the calculation of an equilibrium association constant. While SPR was useful in confirming antibody binding to PA680B-MPC (A₁) under certain circumstances, it was ineffective in other cases.

These results highlight the antigenicity of conformational peptide epitope functionalized nanoclusters and confirm the importance of secondary structure in addition to primary sequence for antibody recognition. A monoclonal antibody (110) was

effectively mapped to the amino acids spanning 680-692 in the protein sequence of the protective antigen of *B. Anthracis* and we have shown there to be a significant difference between linear and conformational antigen mimics.

Antigen Mimic Immunogenicity

Linear and conformational peptide epitope functionalized nanoclusters or antigen mimics have been shown to be antigenic (interface effectively with antibodies) in several cases.^{2, 21, 49, 51} Conformational antigen mimics have also been shown to interface more effectively with antibodies as compared to their linear counterparts.⁵¹ The next step in characterizing these antigen mimics would be to evaluate their immunogenicity (ability to interface with an immune system and illicit an immune response) using a mouse model system. Thirty four mice were used in these experiments and were divided into 8 groups (Table 9). Each mouse was injected with 200 μ L of material both subcutaneous and intraperitoneal for a total of 400 μ L.

Table 9. Summary of injection groups and concentrations of antigens used in antibody production assay. ^aPA680M peptide conjugated to KLH carrier protein. ^bGroup inadvertently injected with one dose of PA-KLH on Day 1 and (A₂) at 9.5 μ M on Day 14. This group was not used in further experiments.

Antigen	[Antigen], μ M	[Effective Epitope], μ M	Material/Dose, mg	# of Mice
PA680B-MPC (A ₂)	9.5	66	0.52	5
	73.7	516	4.04	5
HA-MPC (E)	8.0	64	0.44	3
	64	510	3.5	3
Tiop-MPC (G)	40	0	2.2	5
^a PA-KLH	0.30	9.0	1.0	4
^b KLH/MPC	N/A	N/A	N/A	5
No Injection	0	0	0	4

This injection was repeated on two additional days as booster shots. While this study was intended as an antibody production assay, toxicology issues also became a priority. Upon injection of high concentrations of nanocluster (73.7 μM PA680B-MPC **A₂** and 64 μM HA-MPC **E**), mice experienced visible distress, ruffled fur, and lethargy in less than 72 hr. By this time two mice had expired and the rest were euthanized by CO₂ inhalation (Figure 40).

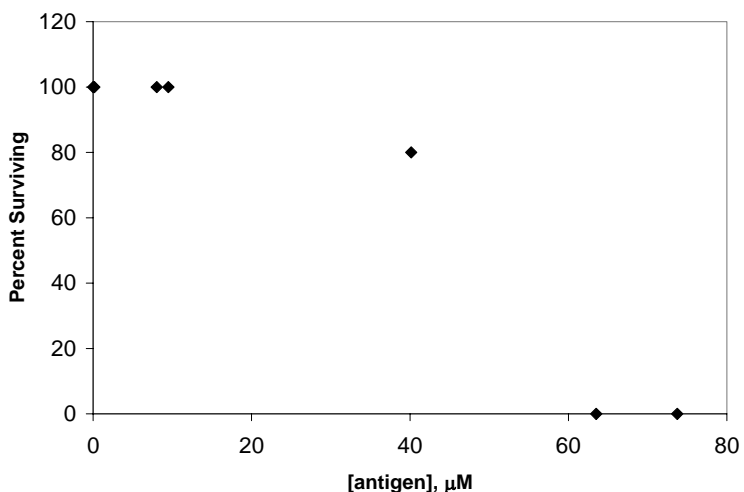


Figure 40. Percent of mice surviving 72 hr after injection with various concentrations of antigen. Concentrations are normalized to moles of nanoparticle injected, not to the moles of peptide epitope presented. LD₅₀ may be approximated at 50 μM .

After euthanization, the mice were dissected and initially inspected visually for misinjection, pooled precipitated nanocluster, or darkened organs. None of these occurrences were observed, indicating that the nanoclusters were soluble and were distributed throughout the body via the blood stream. Heart, lungs, liver, and spleen organs were collected from at least three mice and fixed in formalin. The organs from

Table 10. Qualitative Au detection in organ tissue extraction using EDAX.

Tissue	Presence of Au
none	-
Heart	++
Lungs	+
Liver	+
Spleen	+++

one mouse were collected for analysis of gold content, while the organs from other mice were analyzed for pathological abnormalities by Hoyin Mok. No abnormalities were reported. Organs collected for gold analysis were homogenized and extracted with 20 mM NaOH. The samples were centrifuged and the supernatant was collected and further filtered. Qualitative gold analysis was completed via energy dispersive x-ray spectroscopy using an EDAX-equipped TEM and showed significant levels of gold in the spleen and heart and reduced levels in the lungs and liver (as compared to a blank grid, Table 10). While quantitative analysis may be possible using EDAX, a second method of analysis may be elemental analysis. Future toxicology studies should focus on these quantitative techniques as well as blood and urine analysis. While this impromptu study provided no conclusive explanation for the toxicity of these nanoparticles, the relatively high retention of gold in the spleen and heart after 72 hrs may be important. Studies involving similar gold clusters show clearance from the blood in approximately 24 hrs and stable/increasing retention in the liver and kidneys at 72 hrs post-injection.^{153, 156} This suggests good retention, which is important for extended interaction with the immune system and the production of antibodies. On the other hand, related studies report no significant toxic effects,^{149, 152-154, 156} while these peptide-presenting nanoclusters show significant toxicity at high concentrations. A possible explanation for

this may involve excessive stimulation of the immune system or a form of hypersensitivity or immunopotentiality.^{162, 163} It is possible that this size and composition of gold nanoparticle act as a potent adjuvant in stimulating an immune response. Over stimulation could then result in a number of different deleterious effects.^{162, 163} These toxicological effects certainly require further attention before more progress is made in immunogenicity studies.

All other mice, injected with low concentrations (8-40 μ M) of nanoparticle or KLH, experienced slight discomfort (slightly ruffled fur), but were generally active and unaffected by nanoparticle toxicity. An exception to this would be one mouse in the Tiop-MPC (**G**) group that received a moderate dose of nanoparticle (40 μ M) and expired 6 days post-injection. These remaining mice received injections on two more days, spaced two weeks apart. Four weeks after the final injection, blood was drawn via the saphenous vein and a second collection of blood was completed two weeks after the first blood draw to obtain more samples. Mice were euthanized shortly thereafter. Whole blood samples were allowed to coagulate and then centrifuged in order to collect the sera. Sera samples were screened against the PA protein, the HA protein, and the PA680B-MPC antigen mimic (**A₂**), initially using ELISA and later confirming results using QCM. ELISA experimental parameters were first optimized using a checkerboard assay with PA protein and anti-PA antibody (antibody 110) as well as HA protein and anti-HA antibody. This same positive control was repeated in all subsequent experiments. An initial experiment using mouse sera and PA protein showed that the best signal to noise ratio was achieved using a 1:10 dilution of sera in PBS, though a 1:100 dilution would also work. Therefore, due to limits in sample availability, all subsequent ELISA experiments

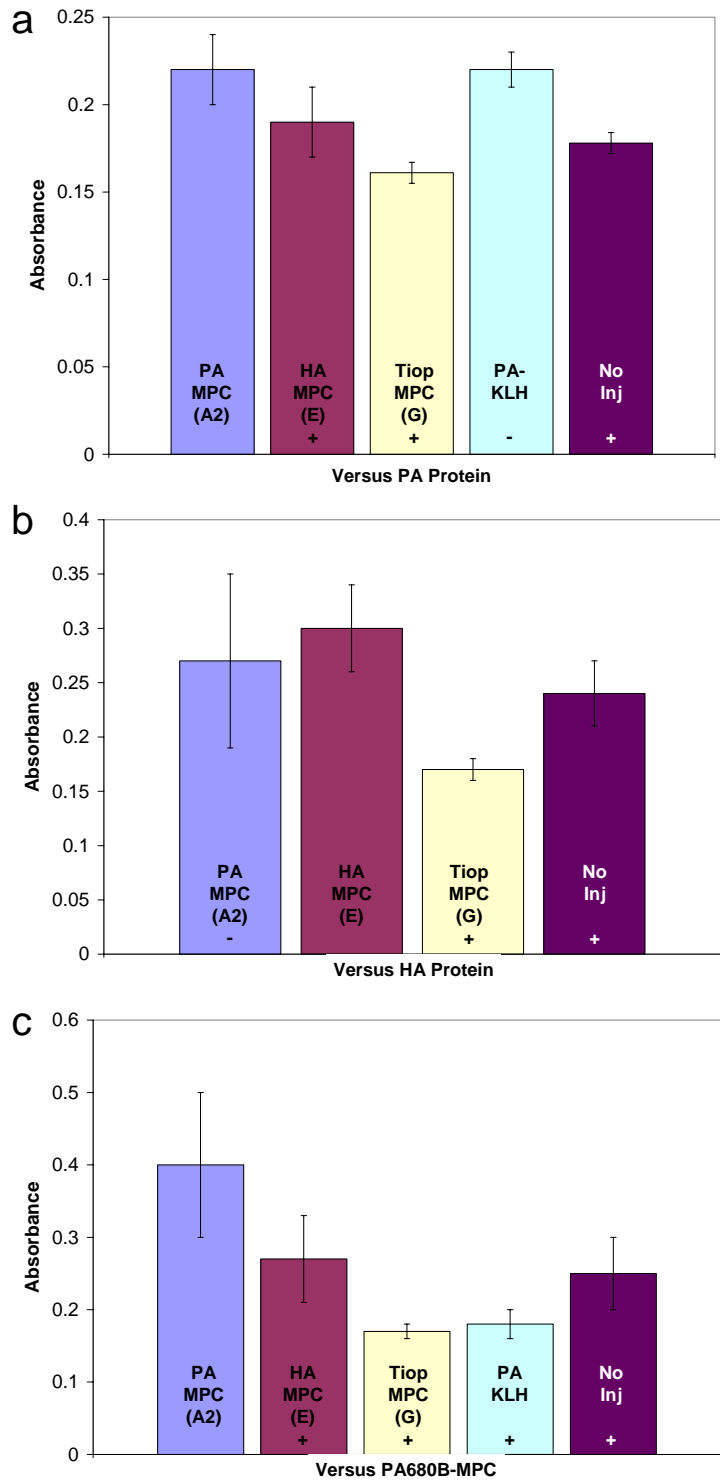


Figure 41. Results of ELISA experiments for immunized mice sera binding to (a) PA protein, (b) HA protein, (c) PA680B-MPC. Results of t-test (99% confidence) comparing sera binding from mice immunized with (A₂) or (E) to all other antigens are listed as + (significant difference) or - (no significant difference).

were run using a 1:100 dilution. Sera from each mouse were then run in triplicate at 1:100 dilutions against the PA protein. The results are available in Figure 41a and show a slight increase in binding from sera coming from mice immunized with the PA680B-MPC antigen mimic (**A₂**). Sera from mice injected with HA-MPC mimic (**E**) bound slightly less, followed by sera from mice injected with Tiop-MPC (**G**), which was similar to the unexposed mice. Similar binding was observed for PA680B-MPC (**A₂**) immunized mice as compared to those mice immunized with the PA-KLH conjugate, which indicates a possible lack of conformational control. Though the differences are small in these cases, statistics (t-test) show that there is a significant difference between binding from PA680B-MPC (**A₂**) sera versus HA-MPC (**E**), Tiop-MPC (**G**), and no injection sera. In general, absorbance values for this ELISA are low as compared to the positive control, indicating less than stellar binding overall. These results were generally confirmed by a standard QCM immunosensor experiment (as above), where binding of sera diluted 1:500 from PA680B-MPC (**A₂**) was significantly different from binding of sera from no injection as well as PA-KLH mice (Figure 42a). This QCM data, as opposed to the ELISA, suggests that there is a difference between immunization with the conformational antigen mimic and the linear PA-KLH.

Similar results were obtained for binding to the HA protein (Figure 41b). Sera from mice immunized with HA-MPC (**E**) bound slightly better than sera from PA680B-MPC (**A₂**), Tiop-MPC (**G**), and no injection. Again there are statistically significant differences, but overall binding is low as compared to the positive control of monoclonal anti-HA antibody binding to the HA protein.

More promising and perhaps relevant results were obtained from sera binding to the PA680B-MPC antigen mimic (A₂) (Figure 41c). Absorbance was higher in these cases, indicating stronger overall binding, and there were more pronounced statistically

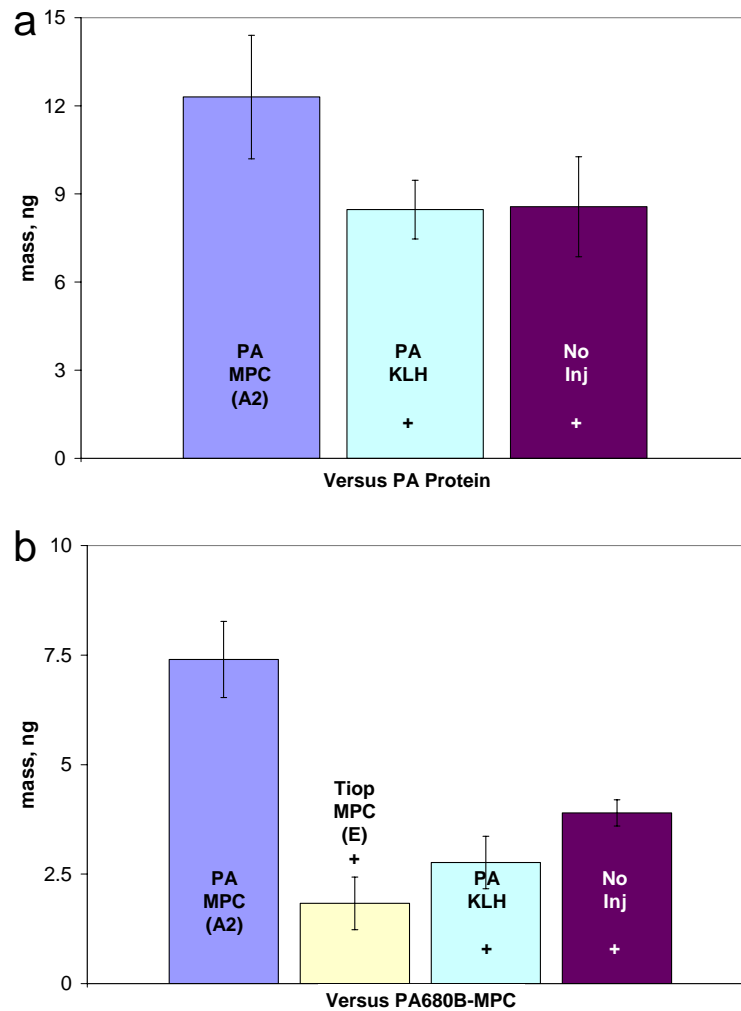


Figure 42. Results of QCM experiments for immunized mice sera binding to (a) PA protein, (b) PA680B-MPC. Results of t-test (99% confidence) comparing sera binding from mice immunized with (A₂) to all other antigens are listed as + (significant difference) or – (no significant difference).

significant differences between sera from PA680B-MPC (**A₂**) immunization as compared to sera from all others. Absorbance for sera from PA680B-MPC (**A₂**) was over double than that for sera from Tiop-MPC (**G**) and PA-KLH. Again, this data was supported by QCM experiments using polyelectrolyte to immobilize the PA680B-MPC (**A₂**) antigen mimic and pooled human sera to block non-specific sites (Figure 42b). Sera diluted 1:500 from mice immunized with PA680B-MPC (**A₂**) showed substantially more binding than any other samples. This data indicates several things about the induced immune response: 1) the response is predicated on peptide epitope presentation and not the Tiop-MPC scaffold; 2) there is a significant difference in the presentation style of peptide on the MPC as opposed to peptide conjugated to KLH; 3) nanoparticle antigen mimics are immunogenic to themselves. Peptide-presenting gold MPCs are immunogenic in the sense that they can illicit an immune response and spur the production of antibodies that bind specifically to the antigen mimic. Further success of sera binding to the intact protein is therefore dominated by an ability to faithfully reconstitute the physiological conformation of the epitope. While antigenicity experiments (above) have suggested the conformational antigen mimic's proximity to physiological conformation, there are advances to be made. Due to the large variation in cluster size within a batch of MPCs, it is likely that only a subset of nanoparticles is able to mimic the true protein conformation. Control over nanoparticle size is a need in future experiments and is already an area of intense research focus.¹⁶⁴

Conclusions

The sum of these results suggests several things about the efficacy of these complex antigen mimics. First, it is apparent that we are able to successfully assemble peptides on nanoclusters to produce functional, immunoreactive nanoscale components. Second, we are able to employ functionalized nanoclusters in the screening of available monoclonal antibodies and effectively map an antibody to a peptide epitope. Third, we were able to differentiate between conformational and linear epitopes and include that degree of complexity into mapping experiments. Antibody 110 has an apparent increased affinity (>2x) for the conformational antigen mimic over the linear antigen mimic and an even greater affinity difference in isotonic ionic strength buffers. Control experiments confirmed the enhanced affinity and place the antigen mimic in the same affinity range as the intact protein. These monoclonal antibodies could be used in the selection and isolation of tight binding, conformationally-relevant antigen mimics, providing information which could guide future mimic assembly. Finally, we showed these conformational epitope-presenting nanoclusters to be immunogenic in eliciting an immune response and prompting the production of antibodies that specifically bind to the antigen mimic. While produced antibodies bound only minimally to intact protein antigens, there is potential to enhance binding by optimizing nanocluster size and peptide presentation. The placement of artificial conformational epitopes on a nanoparticle framework represents a significant early advance in our ability to control immunomodulation at the nanoscale.

CHAPTER V

COUPLED MONOLAYER-PROTECTED CLUSTERS EXHIBIT ENHANCED NEAR IR FLUORESCENCE

Introduction

Nanometer-sized monolayer-protected metal clusters (MPCs) have received considerable attention for their intense optical properties, including broad fluorescence emission in the visible and near infrared spectrum,^{33, 165-168} which makes them potential candidates for chemical and biological sensing applications. Important experiments^{165, 166} have helped to elucidate the mechanism of fluorescence as well as dependence on metal core composition, metal core size, and passivating ligand composition. Generally, nanoparticles with gold or silver cores of diameter less than 5 nm with organic or water soluble passivating ligands have shown the most promising results.¹⁶⁵ Specifically, small (1.8 nm diameter) tiopronin-protected gold nanoparticles were shown to have high efficiency (~ 0.3%) visible luminescence.¹⁶⁶ The mechanism of visible luminescence has been suggested to involve a size-dependent opening of the HOMO-LUMO energy gap and interband emission from 6sp to 5d energy levels.^{33, 166} It has also been postulated that near-IR luminescence is generated from a transition at an energy lower than the sp to d interband model and rather originates from an sp to sp-like transition.¹⁶⁵

In addition to their intrinsic visible and near-infrared fluorescence, nanoparticles offer convenient size, stability, solubility, and reactivity as molecular scaffolds.^{35, 169} Specifically, nanoparticles have supported various fluorescent probes and have been shown to efficiently quench fluorescent emission.¹⁷⁰⁻¹⁷⁴ This fluorescent quenching has

not only been used to study the phenomenon of energy transfer, but has also been used in a variety of chemical and biological sensors. Recently, the Murray group has examined the different settings for quenching by soluble MPCs, including static, reversible, and collisional interactions. Experiments were carried out using several different fluorophores and a variety of MPCs with different sizes (1-4 nm diameter) and solubilities and point to a clear relationship between cluster size and quenching efficiency.¹⁷¹ Quenching efficiency has also been related to the distance from fluorophore to gold nanoparticle in work recently completed in the Decher labs.¹⁷² Layer-by-layer addition of oppositely charge polyelectrolyte created polymer encapsulated nanoparticles and provided exquisite control over the distance between the metal and fluorophore. In this way, dye fluorescence was shown to increase with additional polymer layers (i.e. increasing distance from the metal) and also increased upon slow chemical removal of the metal core.¹⁷² Nanoparticle quenching ability has also been used in sensor design. In 2001, single mismatches were detected in DNA using a self-complimentary single strand that hybridizes to a hairpin-shaped structure, thereby placing a 1.4 nm gold cluster in proximity to a fluorescent dye. Fluorescence quenching is then alleviated by introducing free complimentary ssDNA.¹⁷⁴ These examples point to the interest in nanoparticle quenching efficiency and their potential in sensor applications.

Conversely, the phenomenon of nanoparticle fluorescence enhancement has been minimally reported. Initially, luminescence enhancement was studied with organic dyes near surface-deposited silver islands and later through the aggregation of silver nanoparticles decorated with fluorescent dyes.^{175, 176} Enhancement using gold has been reported when fluorescent dyes are attached with the molecular dipole parallel to the

nanoparticle surface¹⁷⁷ and when nanoparticles suppress the non-radiative decay of attached dyes.¹⁷⁸ These few examples report on the ability of gold and silver nanoparticles to augment the fluorescence intensity or lifetime of common organic dyes. The intrinsic fluorescence of water-soluble Au-MPCs and fluorescence enhancement is the focus of this research. To our knowledge, we make the first report on Pt-MPCs lack of near-infrared fluorescence and, importantly, on their ability to increase the fluorescent intensity of Au-MPCs when covalently attached or decrease fluorescence intensity when non-covalently mixed.

Experimental

Chemicals

Gold shot (99.99%) was purchased from precious metal vendors and was initially converted to $\text{HAuCl}_4 \cdot 3\text{H}_2\text{O}$ by boiling Au^0 in HCl/HNO_3 solution.¹¹⁹ TMA ligand (N,N,N-trimethyl-10-undecenylammonium) was synthesized as previously described.¹⁷⁹ $\text{H}_2\text{PtCl}_6 \cdot 6\text{H}_2\text{O}$ was purchased from Strem Chemical. The peptide $\text{NH}_2\text{-C}_6\text{H}_{12}\text{-AVRWLLTA-C}_6\text{H}_{12}\text{-Cys-COOH}$ was obtained from Dr. Oliver McIntyre and the peptide $\text{NH}_2\text{-YPYDVDPDYAC-COOH}$ was obtained from Dr. David Wright. All other chemicals were reagent grade and used as received.

Monolayer-Protected Cluster Synthesis and Characterization

Au-MPCs were synthesized with N,N,N-trimethyl(11-mercaptoundecyl)ammonium ligand (TMA) as previously described.¹⁷⁹ Briefly, 2.5 mmol of HAuCl_4 and 3.5 mmol of

TMA ligand were co-dissolved in 18 M Ω water and stirred for 30 min. An excess of aqueous sodium borohydride (25 mmol) was then added rapidly to initiate vigorous reduction (*caution!*) of the metal salt to the metal MPC. After one hour of stirring, nanoparticles were loaded into cellulose ester membrane tubing (Spectra/Por CE, MWCO = 10,000 daltons) and impurities were dialyzed into water over several days. Pt-MPCs were synthesized in a similar fashion¹⁸⁰ with tiopronin (N-(2-mercaptopropionyl)-glycine) ligand. Equimolar H₂PtCl₆ and tiopronin were co-dissolved in 6:1 (v/v) methanol/glacial acetic acid, chilled to 0 °C, and reduced with excess NaBH₄. Purification was achieved by dialysis, as above. Characterization of MPCs was completed using nuclear magnetic resonance spectroscopy, UV/visible spectroscopy, transmission electron microscopy, and thermogravimetric analysis, as previously described.⁴⁹ UV-visible absorbance and near-IR fluorescence of Au-MPCs and Pt-MPCs was obtained at 100 nM concentration in 0.1 M MES buffer, pH 6.0, 0.5 M NaCl. Fluorescence spectra were recorded on a Horiba Jobin Yvon Fluorolog spectrofluorometer. Typical experiments involved excitation at 400 or 680 nm with emission recorded from 750 to 1250 nm. A standard Au-MPC sample at known concentration was used as a reference sample throughout the experiments.

Place Exchange and Coupling

Peptide linkers (Figure 45) were place exchanged onto Au-MPCs for the purpose of nanoparticle coupling, as previously described.^{49, 51} Briefly, 3.1 mg of linker in 10 mL methanol was added to 10 mg of Au-MPCs in 10 mL of water and stirred for 7 days. The methanol was removed by rotary evaporation and the linker-presenting Au-MPCs (**D**)

were purified by dialysis, as above. The approximate number of peptides per nanocluster was determined to be 30 by ^1H NMR, as previously described (Figure 44b).⁴⁹ Coupling experiments used equimolar amounts of **D** and Pt-MPCs. A six-fold molar excess of EDC and sulfo-NHS were added to Pt-MPCs in 0.1 M MES/0.5 M NaCl and stirred for 15 minutes to allow activation of the carboxylic acid groups. **D** was subsequently added, stirred for two hours, at which time 10 mM hydroxylamine was added to quench the reaction. The reaction mixture was purified by size exclusion chromatography (Sephadex G50, Sigma), similar to previous experiments.¹⁸¹

Enzymatic Linker Cleavage

Reaction of coupled MPCs with trypsin protease was carried out in 0.1 M borate buffer pH 9.0 at approximately 0.4 μM (**D**) and a 50:1 molar ratio of Au-MPC peptides (12 μM) to trypsin (240 nM). Fluorescence spectra were recorded every 10-15 min, following manual mixing of the solution. Samples were held at 37 °C with a water bath or allowed to remain at room temperature.

Results and Discussion

Monolayer-Protected Cluster Synthesis and Characterization

Au-MPCs were synthesized with TMA as the passivating ligand, while Pt-MPCs were synthesized with tiopronin, according to established procedure.^{179, 180} Careful

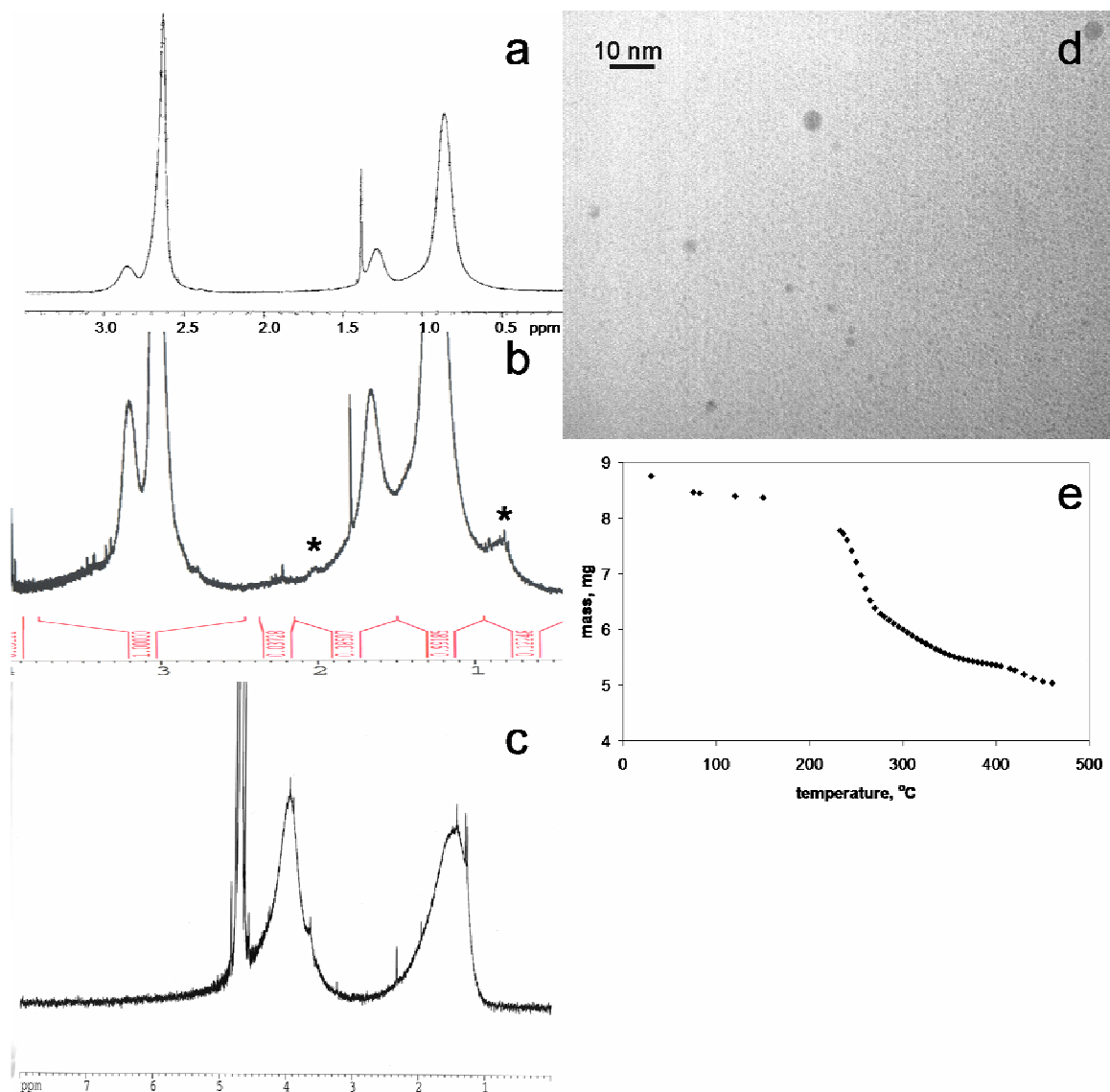


Figure 43. Characterization of Au-MPCs and Pt-MPCs. (a) Proton NMR of Au-MPCs showing composition of monolayer and purity of the sample; (b) Proton NMR of Au-MPCs presenting peptide linker (peaks indicative of peptide are denoted by *); (c) Proton NMR of Pt-MPCs showing composition of the monolayer and purity of the sample; (d) TEM image of Au-MPCs showing spherical cluster, approximate size, and size dispersity; (e) TGA data of Au-MPCs showing a decomposition transition at ~ 200 °C and the overall percent of organic molecules by weight.

characterization of both nanoparticles allowed for size and composition approximation (Au-MPCs *ave* diameter = 4.3 ± 1.7 nm, *ave* composition = $\text{Au}_{1460}\text{TMA}_{776}$; Pt-MPC *ave*

diameter = 2.5 nm, *ave* composition = Pt₂₉₄Tiop₁₀₄) as well as determination of absorbance and fluorescence properties. Proton NMR of Au-MPCs, Au-MPCs presenting peptide, and Pt-MPCs are available in Figure 43 a, b, and c, respectively. TEM and TGA data for Au-MPCs can be found in Figure 43 d and e, respectively. UV-visible absorbance and near-IR fluorescence of Au-MPCs and Pt-MPCs are available in Figure 44.

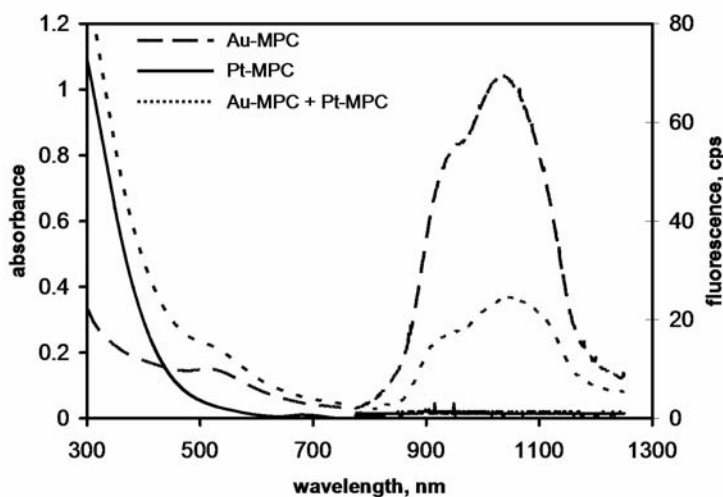


Figure 44. Absorbance (300-750 nm) and fluorescence (ex 680 nm, em 775-1250 nm) of Au-MPCs at 100 nM, Pt-MPCs at 100 nM, and of a mixture of Au-MPCs and Pt-MPCs, each at 100 nM.

While both nanoparticles exhibit broad absorbance across the UV and visible region, Au-MPCs have a distinct plasmon resonance band centered at 520 nm and a brown/red hue due to their relatively large diameter.^{169, 179} Pt-MPCs show little to no plasmon resonance band and an orange-brown color due to their smaller diameter.¹⁸⁰ Furthermore, Au-MPCs show significantly stronger near-IR fluorescence as compared to Pt-MPCs when excited at either 400 or 680 nm. This may be due to the composition or size of the metal

core or could be related to the length or polarity of the capping ligand. Mixing equimolar solutions of Au-MPCs and Pt-MPCs (Figure 44) shows an additive absorption spectrum, but quenched fluorescence. This quenching is believed not to come only from self-absorbance or self-quenching (upon effectively doubling the solution absorbance), but from a collisional or reversible, electrostatic interaction.¹⁷¹

Fluorescence Enhancement of Coupled Nanoparticles

We also report on static enhancement of near-IR fluorescence upon coupling of Au-MPCs directly to Pt-MPCs. A significant advantage of monolayer-protected clusters is the ease with which they are functionalized or derivatized. Either through reactions with the protecting ligand (i.e. amide coupling)³⁵ or through direct reaction with the metal core (place exchange),³⁴ functional units ranging from redox molecules⁴⁴ to peptide epitopes^{49, 51} have been presented on MPCs. Similar strategies have been used to couple or bridge nanoparticles.^{121, 182-185} Rigid, conjugated, thiol-terminated linkers have allowed for spatial arrangement of gold and silver nanoparticles into dimers, trimers, and tetramers, which has led to the study of optical and electromagnetic coupling.¹⁸³ Feldheim, et al. observed a small shift in the plasmon resonance band upon coupling gold particles into dimers and trimers.¹⁸² Long, flexible peptide linkers (**D**, Figure 45) were place exchanged onto Au-MPCs for the purpose of nanoparticle coupling. Interestingly, the intrinsic fluorescence of Au-MPCs was enhanced by addition of the peptide linker, but was still quenched by mixing with Pt-MPCs (**E**, Figure 45).

Direct coupling of **D** to Pt-MPCs was achieved through the free amine of the peptide linker, the multiple carboxylic acids on Pt-MPCs, and standard amide coupling reagents.

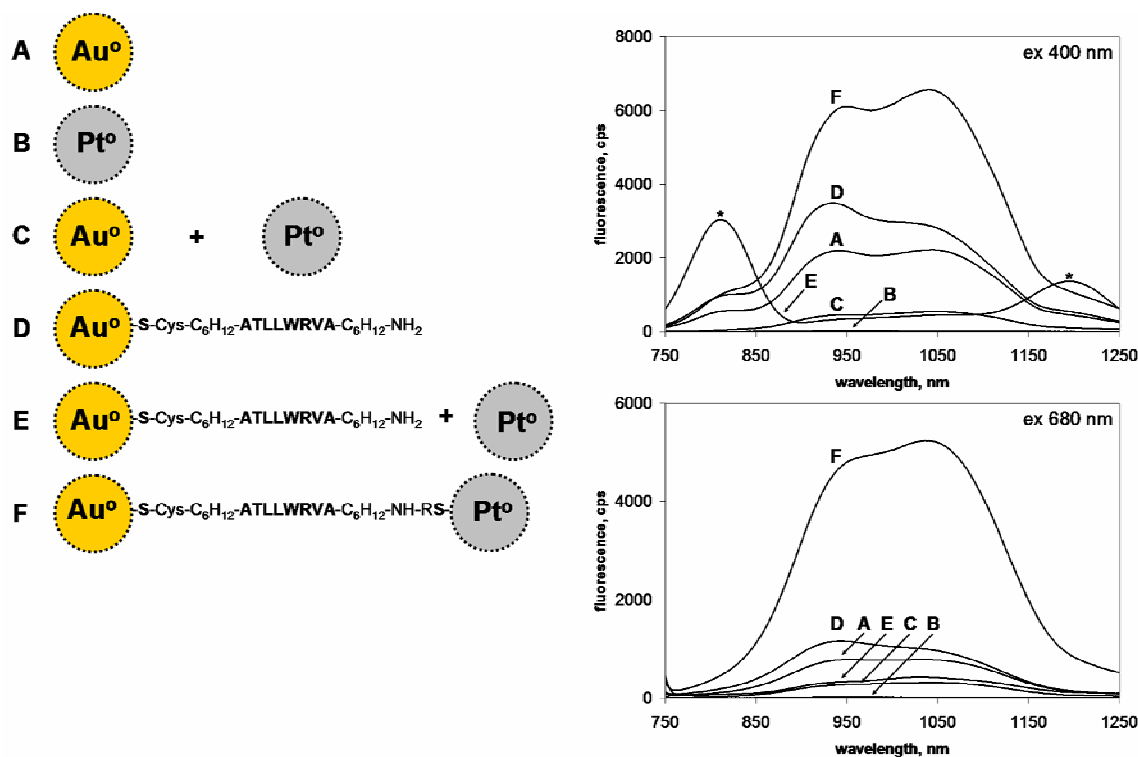


Figure 45. Idealized cartoon of monolayer-protected clusters, conjugates, and mixtures and their fluorescence when excited at 400 nm or 680 nm. The concentrations of gold or platinum nanoparticles in all solution were approximately $0.36 \mu\text{M}$ at 400 nm excitation and $0.24 \mu\text{M}$ at 680 nm excitation. Fluorescence for each solution was normalized to a standard solution of **A**. *Artifact fluorescence from 2nd and 3rd overtone of 400 nm. (**A**) Gold nanoparticle capped with TMA ligand; (**B**) Platinum nanoparticle capped with tiopronin ligand; (**C**) non-conjugated equimolar mixture of **A** and **B**; (**D**) Gold nanoparticle **A** presenting approximately 30 peptide linkers per nanoparticle; (**E**) non-conjugated, equimolar mixture of **B** and **D**; (**F**) Nanoparticles **B** and **D** covalently coupled through the peptide linker.

Equimolar amounts of **D** and Pt-MPCs were used in order to promote one-to-one Au-MPC to Pt-MPC coupling. The reaction mixture was purified by size exclusion chromatography (Sephadex G50, Sigma), similar to previous experiments,¹⁸¹ in order to remove impurities and possibly separate products by size or coupling efficiency. Initially, four fractions were collected from the column: the beginning of the nanoparticle band, the middle, the end of the band until no visible nanoparticle remained, and

remaining buffer eluent. Initial characterization of these fractions shows a slight red shift in the Au-MPC plasmon resonance band, indicating coupled or aggregated clusters. Proton NMR also shows Au-MPCs and Pt-MPCs in the same solution, though cannot confirm conjugation (Figure 46a). TEM images show a lack of broad aggregation, but MPCs in proximity to each other, suggesting the presence of dimers or trimers (Figure 46b).

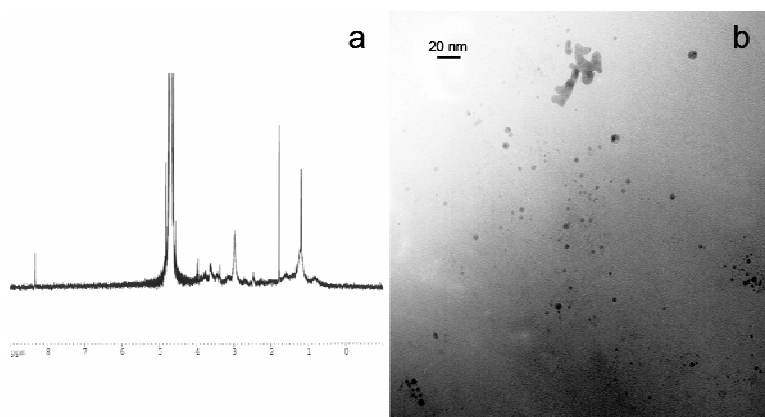


Figure 46. Characterization of MPC conjugates. (a) ^1H NMR of Au-MPC/Pt-MPC conjugates. At the high concentrations generally needed for NMR, aggregation between the positively-charged Au-MPCs and the negatively-charged Pt-MPCs causes interesting peak shifts, which makes peak analysis difficult. Peaks indicative of Au-MPCs, peptide, and Pt-MPCs are present, but overlapping. (b) TEM image of Au-MPC/Pt-MPC conjugates showing a lack of broad aggregation, a relatively large number of isolated, unconjugated nanoclusters, and the possibility of dimers and trimers.

The most conclusive data is the fluorescence enhancement upon conjugation. Representative fluorescence of coupled nanoparticles (**F**) from early and middle fractions, as compared to uncoupled and mixed nanoparticles, is available in Figure 45. When excited at both 400 and 680 nm, a significant increase in fluorescence intensity is observed as compared to all other nanoparticle mixtures at similar concentrations (**A-E**,

concentrations confirmed by visible absorbance). Fluorescence measurements taken on different days were normalized to a standard solution of **A**. Comparable results were obtained upon repeating this procedure in two additional replicate experiments. The increase in fluorescence intensity for **F** as compared to **D** is available in Table 11 and ranges from a small increase of 1.35x when excited at 400 nm to a larger increase of 4.65x when excited at 680 nm.

Table 11. Fluorescence ratio of **F** relative to **D**.

Replicate Experiment	Column Fraction	Excitation Wavelength	
		400 nm	680 nm
1	2	2.34 ± 0.11	4.65 ± 0.08
2	2	1.89 ± 0.11	4.52 ± 0.08
3	2	1.35 ± 0.09	1.48 ± 0.09
3	3	2.52 ± 0.09	2.55 ± 0.09

While excitation at 680 nm appears to provide overall lower fluorescence intensity, emission from that wavelength seems to be more sensitive to nanoparticle coupling. A much larger increase in fluorescence can be obtained when coupled nanoparticle **F** is compared to a gold/platinum mixture **E**, where collisional or reversible quenching occurs. This is evidenced in Figure 45 where **F** fluorescence is enhanced 14.6x at 400 nm excitation and 12.2x at 680 nm excitation. The differences in fluorescence measurements from replicate experiments certainly come from differences in excitation wavelength, variability in column separation and fraction collection, and small differences in sample preparation. The large nanoparticle size dispersity, which could affect nanoparticle optical properties, the distance between coupled nanoparticles, as well as the number of peptide linkers per particle, may also play a role in the measurement precision.

In order to limit some of these differences and better understand the contents of our sample, further size exclusion chromatography experiments were conducted on nanoparticles from the 3rd replicate experiment. The fractions from this sample were recombined and subsequently re-separated in order to collect volume-defined fractions. The chromatogram from this separation is available in Figure 47. The fluorescence spectrum for each 1 mL fraction from this separation was obtained and compared to **D** at similar concentrations (concentrations of fractions were matched to controls via visible absorbance). The percent increase in fluorescence intensity, as compared to the control, is also plotted in Figure 47 and indicates that nanoparticles in early fractions exhibit larger fluorescence enhancement. This agrees with the principles of size-exclusion chromatography; that larger analytes will pass through the column more quickly than smaller analytes.

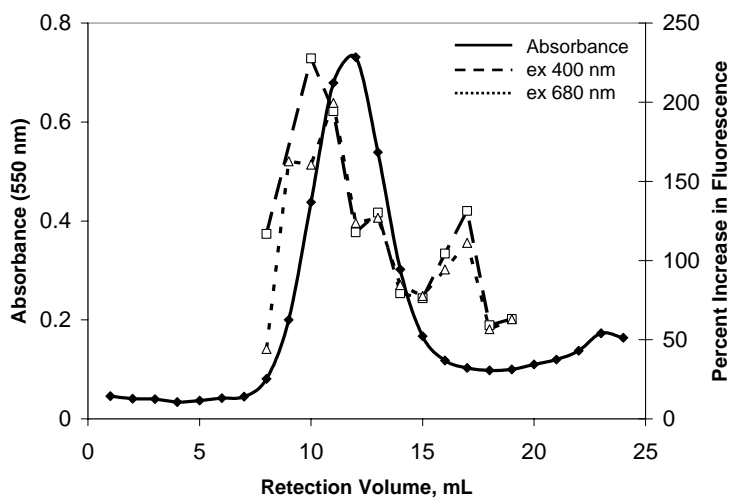


Figure 47. Fluorescence enhancement after fractionation of coupled nanoparticles using size-exclusion column chromatography. Absorbance of each fraction is plotted to show the retention of the nanoparticle on the column. The percent increase in fluorescence is plotted by fraction and shows that a greater increase in fluorescence is observed in early fractions.

It is also interesting to note the fluorescence peak shape in Figure 45. Regardless of excitation wavelength, Au-MPCs exhibit two distinct peaks in their emission band. These two peaks, at 942 nm and 1045 nm, are of roughly equal intensity in a Au-MPC solution (**A**). Changing the overall charge and polarity of Au-MPCs via place exchange of the peptide linker (**D**) also changes the peak shape. The higher energy peak is intensified and slightly blue shifted to 935 nm as compared to the lower energy peak, which remains around 1045 nm. Further coupling of **D** to Pt-MPCs elicits another change in peak shape. The low energy peak remains at 1045 nm, but is intensified compared to the higher energy peak, which is red shifted back to 950 nm. These changes in peak shape and intensity appear to be due to polarity changes in the nanoparticle ligand and suggest that the interesting phenomenon of fluorescence enhancement may also be related to electronic interactions between the metal nanoparticle cores facilitated by the opposite polarities of the MPC protecting ligands. The Au-MPCs are permanently positively charged due to the trimethylammonium ligand and the Pt-MPCs are negatively charged at neutral pH due to the carboxylic acid termini of the tiopronin ligand. This opposite polarity facilitates an electrostatic interaction of the nanoparticle ligands, which may promote an electronic interaction between the metal cores. This interaction may create an electronically conjugated system that enhances fluorescence emission of the Au-MPCs. Preliminary experiments using Au-MPCs with tiopronin ligands, a similar peptide linker (amino acid sequence: NH₂-YPYDVDPDYAC-COOH), and Au-MPCs with TMA ligand showed comparable fluorescence enhancement (data not shown). This suggests that the composition of the linker may not be important, but the linker length

may play a role. It also indicates that enhancement of gold nanoparticle fluorescence may be possible using different types of metal cores with different electronic structures.

Enzymatic Linker Cleavage

This observed fluorescence enhancement has applications in the realm of biosensors. Changes in optical properties have long been used in molecular identification and in chemical and biological sensing. Nanoparticle-based optical sensors have been important additions as analytical methods and have been used in the detection of many different analytes. For example, techniques have made use of shifts in plasmon resonance band absorbance upon extended aggregation and polymeric network formation for the sequence-specific, sensitive detection of DNA.¹⁸⁶ A similar approach was used for studying molecular recognition and lectin-carbohydrate interactions.¹⁸⁷ Single-mismatch detection in oligonucleotides has also been achieved using a FRET-based molecular beacon and the phenomenon of gold nanoparticle fluorescence quenching.¹⁷⁴ Enzyme-active probes have also been predicated on these phenomenon and have been assembled from organic dyes,^{188, 189} conjugated fluorescent polymers,¹⁹⁰ semi-conductor quantum dots,¹⁹¹ and gold nanoparticles^{191, 192} for the detection of different proteases. A peptide-linked near-IR active transducer using a combination of fluorescence enhancement from coupled nanoparticles and fluorescence quenching from separated nanoparticles could also be used in protease detection. Numerous cleavable peptide linkers could be employed to couple gold and platinum nanoparticles, creating enhanced fluorescence. Specifically severing the linker would liberate the nanoparticles and reduce fluorescence intensity. The peptide linker used in these studies (NH₂-C₆H₁₂-AVR*W[#]LLTA-C₆H₁₂-

Cys-COOH) was designed as a substrate for the common serine protease trypsin and the cancer-related protease matrix metalloprotease-9 (MMP-9).¹⁹³ Trypsin is known to cleave after basic amino acids such as lysine (K) and arginine (R, denoted by *), while MMP-9 cleaves after tryptophan (W, denoted by #).¹⁹³ The advantages of a MMP sensor that could potentially be used in near-IR imaging experiments are obvious, though initial enzyme experiments were carried out using the widely available and well-studied trypsin.

Fluorescence spectra for reactions of coupled MPCs with trypsin protease were recorded every 10-15 min for three different solutions: (1) coupled MPCs with enzyme, held at 37 °C; (2) coupled MPCs with no enzyme, held at 37 °C; (3) coupled MPCs with enzyme, held at room temperature. The percent decrease in fluorescent intensity for these solutions over 3-4 hours is plotted in Figure 48.

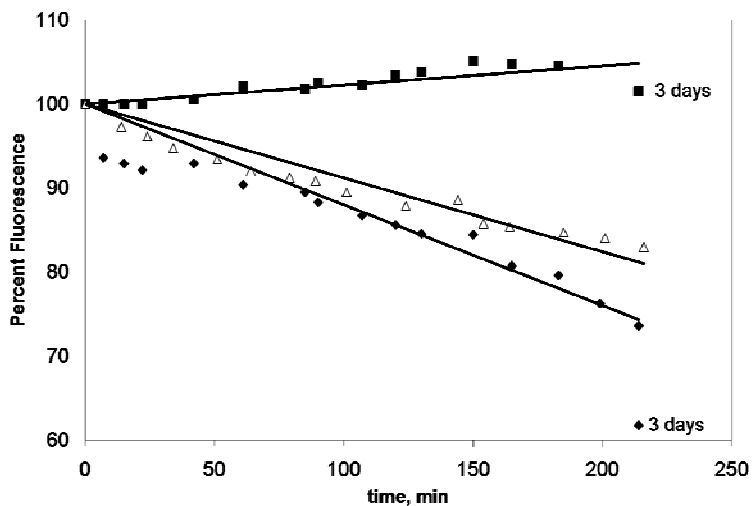


Figure 48. Decrease in fluorescence upon enzymatic cleavage of the peptide linker in (F). Coupled nanoparticle show 38% decrease in fluorescence intensity when incubated with the protease trypsin at 37 °C (diamond). Fluorescence decrease occurred more slowly when incubated at ~25 °C (triangle). Coupled nanoparticle in the absence of enzyme did not show photobleaching or loss of fluorescence (square). Slight increase in fluorescence is attributed to minor evaporation of solvent and concentration of particle.

Solution (1) shows a constant decrease in fluorescence intensity to 74% of initial intensity over approximately 200 min. Solution (2), coupled cluster with no enzyme, shows some variability in fluorescence but retains nearly 100% of initial fluorescence. A slight increase in fluorescence is attributed to the slow evaporation of solvent leading to concentration of the analyte. This not only confirms the activity of the enzyme, but also removes the possibility of fluorescence decrease from photobleaching. Solution (3), which was run at room temperature, showed a decrease in fluorescence intensity to 83% of the initial intensity, as expected due to the lower temperature. The two solutions initially held at 37 °C were revisited after 3 subsequent days at room temperature to show that only 62% of initial fluorescence remained for solution (1) while solution (2) remained around 100%. Final fluorescence intensity that is 62% of initial intensity is likely due to incomplete cleavage of all peptide linkers. Complete cleavage would yield a solution of coupled, mixed nanoparticles exhibiting quenched fluorescence, as in (E). However, the stable fluorescence after 3 days suggests the achievement of an endpoint where all of the accessible peptide is cleaved. Further optimization of enzyme experiments and longer time studies may elucidate this point. In general, the length of these initial studies and relatively slow rate of cleavage suggests a lack of kinetic lability for peptide cleavage. Steric hindrance is likely a dominating factor in this case as the two linked nanoparticles block enzymatic access to the coupling peptide in between. While additional spacer units on either end of the peptide linker may provide for easier access to the protease, it may also alter the fluorescent properties of the couple. Practical use of this phenomenon as a device would certainly require the optimization of these and other parameters.

Conclusions

These experiments highlight the interesting and useful phenomena of gold/platinum nanoparticle fluorescence quenching when untethered and fluorescence enhancement when coupled. Gold TMA-MPCs have intrinsic near-IR fluorescence, while platinum tiopronin-MPCs have little to no fluorescence. The Pt-MPCs are able to quench the fluorescence of the Au-MPCs when mixed in solution, but are also able to cause fluorescence enhancement when coupled by a peptide linker. Enhancement of up to 4.50x as compared to peptide-presenting Au-MPCs and nearly 15x when compared to a quenched mixture of Au-MPCs and Pt-MPCs was observed. Fluorescence enhancement is speculated to be derived from the opposite polarity of the two nanoparticle ligands promoting an electronic interaction between the metal cores, creating an electronically conjugated system. This enhancement has potential in the design of numerous biosensors. A 38% decrease in fluorescence intensity was observed upon cleavage of the peptide linker by the protease trypsin. Further study and optimization of this system would be possible and necessary for practical use as an enzyme sensor.

APPENDIX A

DETECTION OF EBOLA VIRUS GLYCOPROTEINS USING A QUARTZ CRYSTAL MICROBALANCE IMMUNOSENSOR

Ineffective Ebola virus detection methods, as well as a lack of preventative medical measures, have prompted the study of alternative strategies. Attempts to develop an assay to detect and distinguish between Ebola Envelope Glycoproteins (EBO/G) from the Sudan/Gulu and Zaire strains began with the identification of polyclonal and monoclonal anti-glycoprotein antibodies. Four antibodies (rabbit antiserum and monoclonal antibodies 17A3, 6D11, and 15H10), as well as their corresponding glycoproteins, were obtained through the Southeast Regional Center for Excellence in Emerging Infections and Biodefense (SERCEB). These antibodies are produced by different methods, are of different subtypes, and are thought to have strain and subunit specificity. Using these antibodies and a Quartz Crystal Microbalance (QCM) transducer^{2, 3, 52} we have designed a biosensor that employs monoclonal antibody 15H10 to directly detect EBO/G with good sensitivity and in real-time.

Several immunosensor assembly strategies, including covalent, non-specific, and recognition-based immobilization, were employed in the optimization of antibody presentation on the QCM surface. In all cases, biological antibody capture agents provided the most consistent antibody presentation. As such, the biosensor was comprised of the QCM quartz crystal, a gold electrode, antibody capture agent (Protein A, Protein G, or Protein L), and anti-EBO/G. Protein A and G are known to non-specifically adsorb to a hydrophobic gold electrode and specifically bind the Fc region of

IgG. This particular antibody immobilization method benefits from the presentation of IgG in such a way that antibody CDRs are unobstructed.^{2, 194} Protein A and G also show species and subtype specificity. For example, Protein A binds strongly to mouse IgG_{2a}, but weakly to mouse IgG₁, while Protein G shows moderate binding to IgG₁.¹⁹⁴ Protein L is thought to bind the kappa light chain region of immunoglobulin without interfering with antigen binding. For this reason, Protein L binds strongly to all mouse IgG subtypes as well as mouse IgM.¹⁹⁴ Using these capture agents, all four antibody samples were immobilized and used in the detection of Zaire and Sudan/Gulu EBO/G, similar to a manner previously described (Chapter II).

After immunosensor assembly, EBO/G was diluted to various concentrations in 50 mM phosphate buffer and introduced to the assembled sensor for a set time of 12 minutes at a flow rate of 30 μ L/min. A new sensor was assembled for each EBO/G binding event. Binding of either strain to rabbit antiserum, 6D11, and 17A3 was largely unsuccessful. Adsorption at low concentrations did not seem to follow a linear trend, while adsorption at high concentrations either indicated apparently low K_a values or non-specific binding. Successful adsorption at relevant concentrations was observed with monoclonal antibody 15H10 for both strains of EBO/G, though the antibodies appeared to have an increased affinity for the Zaire strain glycoprotein over the Sudan/Gulu strain glycoprotein. Adsorption increased with increasing concentration until saturation was reached (Figure 49a). This data allowed the calculation of an equilibrium adsorption constant (K_a) by fitting to a Langmuir isotherm³ for the Zaire strain EBO/G of $(9 \pm 1) \times 10^6 \text{ M}^{-1}$. Although concentration dependent binding occurred for the Sudan/Gulu strain, the large error in isotherm fitting precluded K_a calculation. Kinetic constants were also calculated

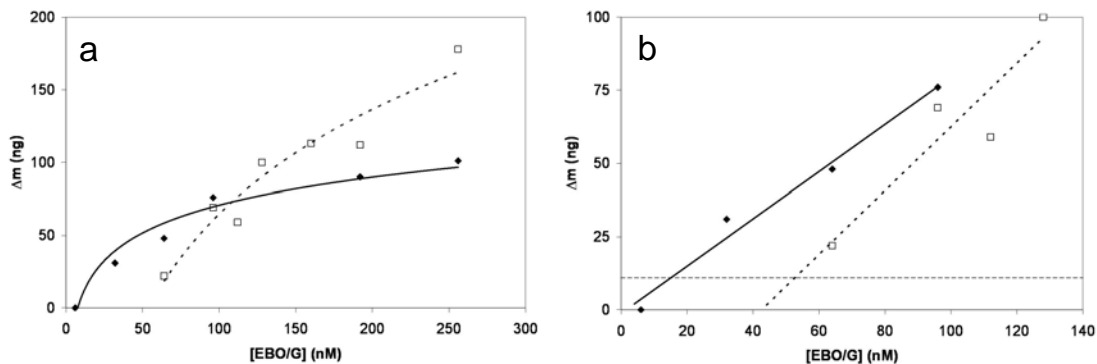


Figure 49. (a) EBO/G adsorption to immobilized antibody, fit to a non-linear curve (Zaire, solid diamond; Sudan/Gulu, open square). (b) Linear region of low concentrations were used to obtain limits of detection.

for the Zaire strain using individual EBO/G binding curves. The forward rate constant (k_f) was found to be $(7.9 \pm 0.6) \times 10^3 \text{ M}^{-1}\text{s}^{-1}$ and the reverse rate constant (k_r) was $(1.9 \pm 0.1) \times 10^{-3} \text{ s}^{-1}$. The quotient of these is equal to the K_a and was determined to be $(4.1 \pm 0.3) \times 10^6 \text{ M}^{-1}$, which is in reasonable proximity to the K_a calculated by isotherm fitting. Affinity (K_a) in the range of $10^6 - 10^7$ is consistent with previously studied immunological systems,^{2, 24, 49, 51} though it is somewhat lower than anticipated for monoclonal antibody. Several methods exist for potentially obtaining a higher affinity antibody.^{10, 11, 22, 23} Another, relatively new approach would be to complete conformational epitope mapping of 15H10 to EBO/G using peptide epitope presenting nanoclusters.⁵¹ Tight binding antigen mimics could then be used in the creation of new antibodies.

Detection limits were calculated for this system by comparing the lowest detectable mass change (11 ng at a signal-to-noise ratio of 3) to the low concentration linear adsorption regions in Figure 49b. Accordingly the lowest detectable concentration of the Zaire and Sudan/Gulu strain glycoproteins would be 14 nM and 56 nM, respectively.

Improved detection limits could be achieved by using a higher affinity antibody, by presenting a higher density of antibody on the QCM surface, or by using a higher MHz crystal. Furthermore, limits for the detection of the intact ebola virus will be significantly better due to the weight of a large virus particle.

Short term future work might include the exploration of antibody immobilization strategies, instrument setup optimization, and detection of EBO/G in more complex samples. The design of a portable, hand-held QCM for environmental and physiological testing is another important goal in instrument development. Peptide epitope presentation on nanoclusters for epitope mapping and to simulate virus particle weight is a further option. Complete details of this work have been published by Yu, et al.¹⁹⁵

APPENDIX B

QUARTZ CRYSTAL MICROBALANCE STUDY OF PIEZOELECTRIC INK JET PROCESSING OF MATERIALS

Piezoelectric ink jet printing is a non-contact, non-destructive, rapid prototyping technique for patterning materials used in medicine and biology. A quartz crystal microbalance sensor was initially used in the study of printing reproducibility and in determining the weight of single printed spots. In initial experiments, the frequency of a 9 MHz crystal was recorded in air before and after printing a 289 single-drop array of multi-walled carbon nanotubes. After accounting for changes in the density and viscosity of the printed solution, a measurement of 861 ng was recorded (Figure 50).

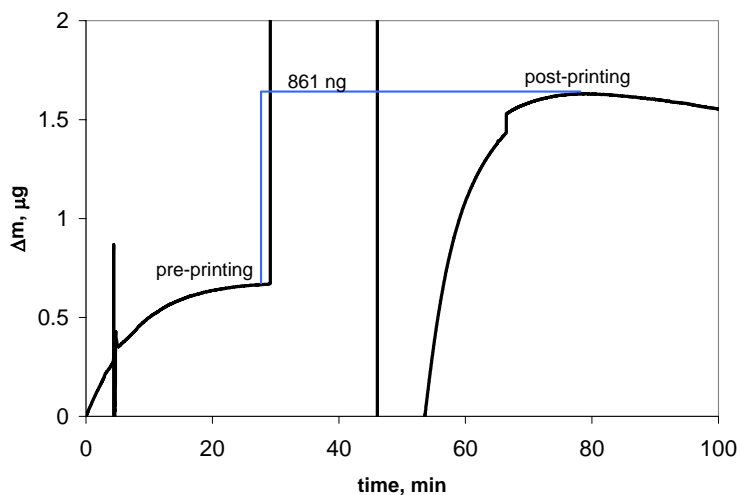


Figure 50. Weight measurement of multi-walled carbon nanotubes solutions using a quartz crystal microbalance.

This equates to 2.978 ng/drop or a ~3 pL drop (assuming a density of 1 g/mL). Future experiments should include a mass/drop calculation for the printing of 1 to 289 drops, the reproducibility of printing any number of drops, and the evaporation time for any number of drops. One potential application for such piezoelectric printing would be in the realm of QCM sensing, where two or more antibodies could be independently, spatially patterned onto a single QCM electrode. This would allow rapid sensor fabrication and multi-analyte detection on a single crystal. The detail of piezoelectric printing were recently published by Sumerel, et al.¹⁹⁶

APPENDIX C

ELECTROSPRAY MASS SPECTROMETRY STUDY OF TIOPRONIN MONOLAYER-PROTECTED GOLD NANOCCLUSERS

Electrospray ionization time-of-flight mass spectrometry (ESI-TOF-MS) was used in the study of gold monolayer-protected cluster synthesis. Studies involved the mass spectral analysis of MPC precursors (Au-Tiop polymers) before and after reduction with sodium borohydride. Standard Tiop-MPC synthetic strategies^{2, 49} were employed, though progress was arrested at certain points to allow for characterization. Co-dissolving HAuCl₄ (0.33 mmol) and tiopronin (1.1 mmol) in 6:1 methanol/glacial acetic acid resulted in the formation of a white, flocculent, light sensitive polymer that grew and precipitated over time. This polymer was determined to grow from the aggregation of a Au₄Tiop₄ cyclic or cubic structure. Interestingly, this structure was also seen as a minor component in the MPC sample post-reduction/purification, indicating the presence of the structure in solution or, more likely, on the surface of the MPC. These results may influence the synthesis of future MPCs, the structural understanding of MPCs, and the mechanistic understanding of MPC reactivity. UV/visible absorbance and transmission electron microscopy measurements were also involved in these studies. Further details can be found in worked recently accepted for publication.¹⁹⁷

APPENDIX D

SINGLE-CHAIN FRAGMENT-VARIABLE RECOMINANT ANTIBODIES WITH AFFINITY FOR ZERO-VALENT METALS

QCM studies have been involved in the development of biological interfaces for inorganic materials. One approach has harnessed the power of the immune system to identify antibodies that bind selectively with zero valent metals. Phage-selected, single chain (ScFv) recombinant antibodies²² to several classes of nanoparticles have been identified. Binding such antibodies directly to bare metal electrodes on QCM crystals is an effective method for confirming activity. Preliminary results have suggested that these recombinant antibodies do bind to the metal for which they have been selected, though the composition of the metal surface (i.e. oxide) may also play an important role in recognition. As seen in Figure 51a, an anti-Ag antibody bound to an unpolished Ag electrode immediately after washing with nitric acid and reforming the oxide layer. Oxide layer formation can be detected after washing with nitric acid (Figure 51a), but the mass adsorption for antibody binding plus oxide formation is far greater than oxide formation only. The Δm due to antibody binding (the difference between the two curves) is 0.6 μg . Unfortunately, attempted removal of bound antibody upon washing of the QCM surface with phosphate buffer does not show mass stripping. This suggests non-specific adsorption over equilibrium recognition. Anti-Ag antibody adsorption was further reinforced by the addition of an anti-E antibody bound FITC fluorescent tag to a short peptide chain (E-tag) on the anti-Ag antibody. Fluorescent emission from the FITC tag/anti-E/E-tag/anti-Ag/Ag QCM complex was captured in an image from fluorescent

microscopy (Figure 51b). Controls (anti-E antibody binding to a silver surface) were performed and yielded a background with significantly less fluorescence (Figure 51b, inset). This two-fold detection shows adsorption of this antibody to its inorganic target and suggests the possibility of a new biology/inorganic interface.

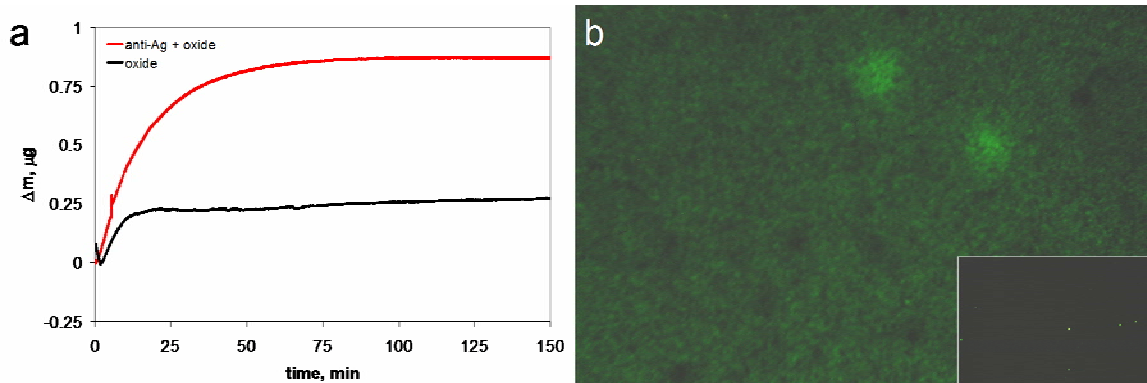


Figure 51. (a) Anti-Ag ScFv antibody binding to a newly formed silver oxide surface (red) shows a larger Δm than oxide formation only (black). (b) Fluorescence microscopy image of anti-Ag antibody bound to Ag substrate and control experiment (inset).

REFERENCES

1. *The material presented in this chapter has largely been published in another source, which is under the copyright of Wiley VCH.*
2. Gerdon, A. E.; Wright, D. W.; Cliffel, D. E. *Anal. Chem.* **2005**, *77*, 304-310.
3. Gerdon, A. E.; Wright, D. W.; Cliffel, D. E., Quartz Crystal Microbalance Characterization of Nanostructure Assemblies in Biosensing. In *Characterization Tools for Nanosystems in Life Sciences*, 1 ed.; Kumar, C., Ed. Wiley-VCH: New York, 2005; *1*, 109-144.
4. Niemeyer, C. M. *Angew. Chem. Int. Ed.* **2001**, *40*, 4128-4158.
5. Storhoff, J. J.; Mirkin, C. A. *Chem. Rev.* **1999**, *99*, 1849-1862.
6. Whaley, S. R.; English, D. S.; Hu, E. L.; Barbara, P. F.; Belcher, A. M. *Nature* **2000**, *405*, 665-668.
7. Slocik, J. M.; Naik, R. R.; Stone, M. O.; Wright, D. W. *J. Mater. Chem.* **2005**, *15*, 749-753.
8. Knecht, M. R.; Wright, D. W. *Chem. Commun.* **2003**, *24*, 3038-3039.
9. Nelson, D. L.; Cox, M. M., *Lehninger Principles of Biochemistry*. Worth Publishers: New York, 2000.
10. Morris, G. E., Choosing A Method for Epitope Mapping. In *Epitope Mapping Protocols*, ed.; Ed. Humana Press: Totowa, NJ, 1996; *66*, 1-9.
11. Mernaugh, R.; Mernaugh, G., *Molecular Methods in Plant Pathology*. CRC Lewis Publishers: Boca Raton, 1995.
12. Crowther, J. R., *The ELISA Guidebook*. Humana Press: Totowa, New Jersey, 2001.
13. Bernard, A. M.; Lauwerys, R. R. *Clin. Chem. Acta* **1982**, *119*, 335-339.
14. Tamiya, E.; Wantanbe, N.; Matsuoka, H.; Karube, I. *Biosensors* **1988**, 139-146.
15. Ortega-Vinuesa, J. L.; Molina-Bolivar, J. A.; Hidalgo-Alvarez, R. *J. Immunol. Methods* **1996**, *190*, 29-38.
16. Lyon, L. A.; Musick, M. D.; Natan, M. J. *Anal. Chem.* **1998**, *70*, 5177-5183.
17. Nam, J.-M.; Thaxton, C. S.; Mirkin, C. A. *Science* **2003**, *301*, 1884-1886.

18. Tang, D. P.; Yuan, R.; Chai, Y. Q.; Zhong, X.; Liu, Y.; Dai, J. Y.; Zhang, L. Y. *Anal. Biochem.* **2004**, *333*, 345-350.
19. Ho, K.-C.; Tsai, P.-J.; Lin, Y.-S.; Chen, Y.-C. *Anal. Chem.* **2004**, *76*, 7162-7168.
20. Liu, G.; Wang, J.; Kim, J.; Jan, M. R. *Anal. Chem.* **2004**, *76*, 7126-7130.
21. Slocik, J. M.; Moore, J. T.; Wright, D. W. *Nano Letters* **2002**, *2*, 169-173.
22. Bird, R. E.; Hardman, K. D.; Jacobson, J. W.; Johnson, S.; Kaufman, B. M.; Lee, S.-M.; Lee, T.; Pope, S. H.; Riordan, G. S.; Whitlow, M. *Science* **1988**, *242*, 423-426.
23. Shen, Z.; Stryker, G. A.; Mernaugh, R. L.; Yu, L.; Yan, H.; Zeng, X. *Anal. Chem.* **2005**, *77*, 797-805.
24. Zhang, Y.; Telyatnikov, V.; Sathe, M.; Zeng, X.; Wang, P. G. *J. Am. Chem. Soc.* **2003**, *125*, 9292-9293.
25. Wegner, G. J.; Lee, H. J.; Corn, R. M. *Anal. Chem.* **2002**, *74*, 5161-5168.
26. Bentzen, E. L.; House, F.; Utley, T. J.; Crowe, J. E. J.; Wright, D. W. *Nano Letters* **2005**, *5*, 591-595.
27. Hostetler, M. J.; Green, S. J.; Stokes, J. J.; Murray, R. W. *J. Am. Chem. Soc.* **1996**, *118*, 4212-4213.
28. Ingram, R. S.; Hostetler, M. J.; Murray, R. W. *J. Am. Chem. Soc.* **1997**, *119*, 9175-9178.
29. Wuelfing, W. P.; Zamborini, F. P.; Templeton, A. C.; Wen, X.; Yoon, H.; Murray, R. W. *Chem. Mater.* **2001**, *13*, 87-95.
30. Schaaf, T. G.; Knight, G.; Shafigullin, M. N.; Borkman, R. F.; Whetten, R. L. *J. Phys. Chem. B* **1998**, *102*, 10643-10646.
31. Templeton, A. C.; Chen, S.; Gross, S. M.; Murray, R. W. *Langmuir* **1999**, *15*, 66-76.
32. Alvarez, M. M.; Khoury, J. T.; Schaaf, T. G.; Shafigullin, M. N.; Vezmar, I.; Whetten, R. L. *J. Phys. Chem. B* **1997**, *101*, 3706-3712.
33. Lee, D.; Donkers, R. L.; Wang, G.; Harper, A. S.; Murray, R. W. *J. Am. Chem. Soc.* **2004**, *126*, 6193-6199.
34. Hostetler, M. J.; Templeton, A. C.; Murray, R. W. *Langmuir* **1999**, *15*, 3782-3789.
35. Templeton, A. C.; Hostetler, M. J.; Warmoth, E. K.; Chen, S.; Hartshorn, C. M.; Krishnamurthy, V. M.; Forbes, M. D. E.; Murray, R. W. *J. Am. Chem. Soc.* **1998**, *120*, 4845-4849.

36. Slocik, J. M.; Knecht, M. R.; Wright, D. W., *Biogenic nanoparticles*. American Scientific Publishers: Stevenson Ranch, 2004.
37. Daniel, M.-C.; Astruc, D. *Chem. Rev.* **2004**, *104*, 293-346.
38. Brust, M.; Walker, M.; Bethell, D.; Schiffrin, D. J.; Whyman, R. *Chem. Commun.* **1994**, *7*, 801-802.
39. Hostetler, M. J.; Wingate, J. E.; Zhong, C.-J.; Harris, J. E.; Vachet, R. W.; Clark, M. R.; Londono, J. D.; Green, S. T.; Stokes, J. J.; Wignall, G. D.; Glish, G. L.; Porter, M. D.; Evans, N. D.; Murray, R. W. *Langmuir* **1998**, *14*, 17-30.
40. Montalti, M.; Prodi, L.; Zaccheroni, N.; Baxter, R.; Teobaldi, G.; Zerbetto, F. *Langmuir* **2003**, *19*, 5172-5174.
41. Song, Y.; Murray, R. W. *J. Am. Chem. Soc.* **2002**, *124*, 7096-7102.
42. Bain, C. D.; Troughton, E. B.; Tao, Y. T.; Evall, J.; Whitesides, G. M.; Nuzzo, R. G. *J. Am. Chem. Soc.* **1989**, *111*, 321-335.
43. Bain, C. D.; Whitesides, G. M. *J. Am. Chem. Soc.* **1989**, *111*, 7164-7175.
44. Templeton, A. C.; Cliffel, D. E.; Murray, R. W. *J. Am. Chem. Soc.* **1999**, *120*, 4845-4849.
45. Gu, H.; Ho, P. L.; Tong, E.; Wang, L.; Xu, B. *Nano Letters* **2003**, *3*, 1261-1263.
46. Zheng, M.; Huang, X. *J. Am. Chem. Soc.* **2004**, *126*, 12047-12054.
47. Hainfeld, J. F.; Powell, R. D. *J. Histochem. Cytochem.* **2000**, *484*, 471-480.
48. Van Regenmortel, M. H. V. *Phil. Trans. R. Soc. Lond. B* **1989**, *323*, 451-466.
49. Gerdon, A. E.; Wright, D. W.; Cliffel, D. E. *Biomacromolecules* **2005**, *6*, 3419-3424.
50. Misumi, S.; Endo, M.; Mukai, R.; Tachibana, K.; Umeda, M.; Honda, T.; Takamune, N.; Shoji, S. *J. Biol. Chem.* **2003**, *278*, 32335-32343.
51. Gerdon, A. E.; Wright, D. W.; Cliffel, D. E. *Angew. Chem. Int. Ed.* **2006**, *45*, 594-598.
52. Janshoff, A.; Galla, H. J.; Steinem, C. *Angew. Chem. Int. Ed.* **2000**, *39*, 4004-4032.
53. Cady, W. G., *Piezoelectricity*. McGraw-Hill: New York, 1946.
54. Martin, S. J.; Spates, J. J.; Wessendorf, K. O.; Schneider, T. W. *Anal. Chem.* **1997**, *69*, 2050-2054.
55. Nomura, T.; Okuhara, M. *Anal. Chim. Acta* **1982**, *142*, 281-284.

56. Kanazawa, K. K.; Gordon, J. G. *Anal. Chem.* **1985**, *57*, 1770-1771.
57. Martin, S. J.; Granstaff, V. E.; Frye, G. C. *Anal. Chem.* **1991**, *63*, 2272-2281.
58. Rickert, J.; Brecht, A.; Gopel, W. *Anal. Chem.* **1997**, *69*, 1441-1448.
59. Chagnard, C.; Gilbert, P.; Watkins, A. N.; Beeler, T.; Paul, D. W. *Sensors and Actuators B* **1996**, *32*, 129-136.
60. Maxtek, Inc. <http://www.maxtekinc.com> (Oct 2006),
61. Hillier, A. C.; Ward, M. D. *Anal. Chem.* **1992**, *64*, 2539-2554.
62. Bandey, H. L.; Martin, S. J.; Cernosek, R. W.; Hillman, A. R. *Anal. Chem.* **1999**, *71*, 2205-2214.
63. Martin, S. J.; Bandey, H. L.; Cernosek, R. W. *Anal. Chem.* **2000**, *72*, 141-149.
64. Theisen, L. A.; Martin, S. J.; Hillman, A. R. *Anal. Chem.* **2004**, *76*, 796-804.
65. Hung, V. N.; Abe, T.; Minh, P. N.; Esashi, M. *Sensors and Actuators A* **2003**, *108*, 91-96.
66. Tatsuma, T.; Watanabe, Y.; Oyama, N. *Anal. Chem.* **1999**, *71*, 3632-3636.
67. Fawcett, N. C.; Craven, R. D.; Zhang, P.; Evans, J. A. *Anal. Chem.* **1998**, *70*, 2876-2880.
68. Thompson, M.; Kipling, A. L.; Duncan-Hewitt, W. C. *Analyst* **1991**, *116*, 881-890.
69. Wijekoon, W. M. K. P.; Asgharian, B.; Casstevens, M.; Samoc, M.; Talapatra, G. B.; Prasad, P. N.; Geisler, T.; Rosenkilde, S. *Langmuir* **1992**, *8*, 135-139.
70. Salamon, Z.; Macleod, H. A.; Tollin, G. *Biochim. Biophys. Acta* **1997**, *1331*, 131-152.
71. Lyon, L. A.; Musick, M. D.; Smith, P. C.; Reiss, R. D.; Pena, D. J.; Natan, M. J. *Sensors and Actuators B* **1999**, *54*, 118-124.
72. Lyon, L. A.; Pena, D. J.; Natan, M. J. *J. Phys. Chem. B* **1999**, *103*, 5826-5831.
73. Pale-Grosdemange, C.; Simon, E. S.; Prime, K. L.; Whitesides, G. M. *J. Am. Chem. Soc.* **1991**, *113*, 12-20.
74. Templeton, A. C.; Zamborini, F. P.; Wuelfing, W. P.; Murray, R. W. *Langmuir* **2000**, *16*, 6682-6688.
75. Mamedov, A. A.; Belov, A.; Giersig, M.; Mamedova, N. N.; Kotov, N. A. *J. Am. Chem. Soc.* **2001**, *123*, 7738-7739.

76. Decher, G. *Science* **1997**, *277*, 1232-1237.
77. Hicks, J. F.; Seok-Shon, Y.; Murray, R. W. *Langmuir* **2002**, *18*, 2288-2294.
78. Katz, E.; de Lacy, A. L.; Fierro, J. L. G.; Palacios, J. M.; Fernandez, V. M. *J. Electroanal. Chem.* **1993**, *358*, 247-259.
79. Davis, K. A.; Leary, T. R. *Anal. Chem.* **1989**, *61*, 1227-1230.
80. Bohinski, R. C. *J. Chem. Educ* **2000**, *77*, 1460-1462.
81. Deisenhofer, J. *Biochemistry* **1981**, *20*, 2361-2370.
82. Karpovich, D. S.; Blanchard, G. J. *Langmuir* **1994**, *10*, 3315-3322.
83. Lauffenburger, D. A.; Linderman, J. J., *Receptors: models for binding, trafficking, and signaling*. Oxford University Press: New York, 1996.
84. Ebara, Y.; Itakura, K.; Okahata, Y. *Langmuir* **1996**, *12*, 5165-5170.
85. Ebato, H.; Gentry, C. A.; Herron, J. N.; Muller, W.; Okahata, Y.; Ringsdorf, H.; Suci, P. A. *Anal. Chem.* **1994**, *66*, 1683-1689.
86. Smith, E. A.; Thomas, W. D.; Kiessling, L. L.; Corn, R. M. *J. Am. Chem. Soc.* **2003**, *125*, 6140-6148.
87. Bard, A. J.; Faulkner, L. R., *Electrochemical Methods: Fundamentals and Applications*. John Wiley & Sons, Inc.: New York, 2001.
88. Su, X.; Chew, F. T.; Li, S. F. Y. *Anal. Sci.* **2000**, *16*, 107-114.
89. Zuo, B.; Li, S.; Guo, Z.; Zhang, J.; Chen, C. *Anal. Chem.* **2004**, *76*, 3536-3540.
90. Stine, R.; Pishko, M. V.; Schengrund, C.-L. *Anal. Chem.* **2005**, *77*, 2882-2888.
91. Uttenthaler, E.; Schraml, M.; Mandel, J.; Drost, S. *Biosens. Bioelectron.* **2001**, *16*, 735-743.
92. Kastl, K.; Ross, M.; Gerke, V.; Steinem, C. *Biochemistry* **2002**, *41*, 10087-10094.
93. Han, L.; Daniel, D. R.; Maye, M. M.; Zhong, C.-J. *Anal. Chem.* **2001**, *73*, 4441-4449.
94. Zamborini, F. P.; Leopold, M. C.; Hicks, J. F.; Kulesza, P. J.; Malik, M. A.; Murray, R. W. *J. Am. Chem. Soc.* **2002**, *124*, 8958-8964.
95. Grate, J. W.; Nelson, D. A.; Skaggs, R. *Anal. Chem.* **2003**, *75*, 1868-1879.
96. Willner, I.; Patolsky, F.; Weizmann, Y.; Willner, B. *Talanta* **2002**, *56*, 847-856.

97. Weizmann, Y.; Patolsky, F.; Willner, I. *Analyst* **2001**, *126*, 1502-1504.
98. Patolsky, F.; Lichtenstein, A.; Willner, I. *J. Amer. Chem. Soc.* **2000**, *122*, 418-419.
99. Hwang, S.; Kim, E.; Kwak, J. *Anal. Chem.* **2005**, *77*, 579-584.
100. Price, C. P.; Newman, D. J., *Principles and practice of immunoassay*. Stockton Press: New York, 1991.
101. Quinn, C. P.; Semenova, V. A.; Elie, C. M.; Romero-Steiner, S.; Greene, C.; Li, H.; Stamey, K.; Steward-Clark, E.; Schmidt, D. S.; Mothershed, E.; Pruckler, J. *Emerging Infectious Diseases* **2002**, *8*, 1103-1110.
102. Salamon, Z.; Macleod, H. A.; Tollin, G. *Biochim. Biophys. Acta* **1997**, *1331*, 117-129.
103. Lian, W.; Litherland, S. A.; Badrane, H.; Tan, W.; Wu, D.; Baker, H. V.; Gulig, P. A.; Lim, D. V.; Jin, S. *Anal. Biochem.* **2000**, *334*, 135-144.
104. Wu, X.; Liu, H.; Liu, J.; Haley, K. N.; Treadway, J. N.; Larson, J. P.; Ge, N.; Peale, F.; Bruchez, M. P. *Nature Biotech.* **2003**, *21*, 41-46.
105. Liu, X.; Sun, Y.; Song, D.; Zhang, Q.; Tian, Y.; Bi, S.; Zhang, H. *Anal. Biochem.* **2004**, *222*, 99-104.
106. Kosslinger, C.; Uttenthaler, E.; Drost, S.; Aberl, F.; Wolf, H.; Brink, G.; Stanglmaier, A.; Sackmann, E. *Sensors and Actuators B* **1995**, *24-25*, 107-112.
107. Spangler, B. D.; Wilkinson, E. A.; Murphy, J. T.; Tyler, B. J. *Anal. Chim. Acta* **2001**, *444*, 149-161.
108. Ma, Z.; Wu, J.; Zhou, T.; Chen, Z.; Dong, Y.; Tang, J.; Sui, S.-F. *New J. Chem.* **2002**, *26*, 1795-1798.
109. Wang, H.; Zeng, H.; Liu, Z.; Yang, Y.; Deng, T.; Shen, G.; Yu, R. *Anal. Chem.* **2004**, *76*, 2203-2209.
110. Leppla, S.; Robbins, J.; Schneerson, R.; Shiloach, J. *J. Clin. Invest.* **2002**, *109*, 141-144.
111. Crowe, J. E. *J. Vaccine* **1998**, *16*, 1423-1432.
112. Chargelegue, D.; Obeid, O. E.; Hsu, S.-C.; Shaw, M. D.; Denbury, A. N.; Taylor, G.; Steward, M. W. *J. Virology* **1998**, *72*, 2040-2046.
113. Douglas, T.; Strable, E.; Willits, D.; Aitouchen, A.; Libera, M.; Young, M. *Adv. Mater.* **2002**, *14*, 415-418.
114. Bracci, L.; Lozzi, L.; Lelli, B.; Pini, A.; Neri, P. *Biochemistry* **2001**, *40*, 6611-6619.

115. Zayats, M.; Kharitonov, A. B.; Pogorelova, S. P.; Lioubashevski, O.; Katz, E.; Willner, I. *J. Am. Chem. Soc.* **2003**, *125*, 16006-16014.
116. Patolsky, F.; Ranjit, K. T.; Lichtenstein, A.; Willner, I. *Chem. Commun.* **2000**, 1025-1026.
117. Vaughan, R. D.; O'Sullivan, C. K.; Guilbault, G. G. *Enzyme and Microbial Technology* **2001**, *29*, 635-638.
118. Langford, J.; Pavey, K. D.; Olliff, C. J.; Cragg, P. J.; Hanlon, G. W.; Paul, F.; Rees, G. D. *Analyst* **2002**, *127*, 360-367.
119. Brauer, G., *Handbook of Preparative Inorganic Chemistry*. AP: New York, 1965.
120. Yoshimoto, M.; Kurosawa, S. *Anal. Chem.* **2002**, *74*, 4306-4309.
121. Novak, J. P.; Brousseau, L. C., III; Vance, F. W.; Johnson, R. C.; Lemon, B. I.; Hupp, J. T.; Feldheim, D. L. *J. Am. Chem. Soc.* **2000**, *122*, 12029-12030.
122. Lide, D. R., *Handbook of Chemistry and Physics*. 77 ed.; CRC: Boca Raton, 1996.
123. The Protein Data Bank. <http://www.pdb.org> (Sept 2003),
124. Whitesides, G. M.; Mathias, J. P.; Seto, C. T. *Science* **1991**, *254*, 1312-1319.
125. Thess, A.; Lee, R.; Nikolaev, P.; Dai, H.; Petit, P.; Robert, J.; Xu, C.; Lee, Y. H.; Kim, S. G.; Rinzler, A. G.; Colbert, D. T.; Scuseria, G. E.; Tomanek, D.; Fischer, J. E.; Smalley, R. E. *Science* **1996**, *273*, 483-487.
126. Ramanathan, T.; Fisher, F. T.; Ruoff, R. S.; Brinson, L. C. *Chem. Mater.* **2005**, *17*, 1290-1295.
127. Knecht, M. R.; Wright, D. W. *Langmuir* **2004**, *20*, 4728-4732.
128. Knecht, M. R.; Wright, D. W. *Chem. Mater.* **2004**, *16*, 4890-4895.
129. Tang, X.; Schneider, T. W.; Walker, J. W.; Buttry, D. A. *Langmuir* **1996**, *12*, 5921-5933.
130. Muller, G. M.; Shapira, M.; Arnon, R. *Proc. Natl. Acad. Sci. USA* **1982**, *79*, 569-573.
131. Lu, Y.; Ding, J.; Liu, W.; Chen, Y.-H. *Int. Arch. Allergy Immunol.* **2002**, *127*, 245-250.
132. Fleury, D.; Barrere, B.; Bizebard, T.; Daniels, R. S.; Skehel, J. J.; Knossow, M. *Nature Struct. Biol.* **1999**, *6*, 530-534.

133. Churchill, M. E. A.; Stura, E. A.; Pinilla, C.; Appel, J. R.; Houghten, R. A.; Kono, D. H.; Balderas, R. S.; Fieser, G. G.; Schulze-Gahmen, U.; Wilson, I. A. *J. Mol. Biol.* **1994**, *241*, 534-556.
134. Martin, S. E.; Peterson, B. R. *Bioconjugate Chem.* **2003**, *14*, 67-74.
135. Petosa, C.; Collier, R. J.; Klimpel, K. R.; Leppla, S. H.; Liddington, R. C. *Nature* **1997**, *385*, 833-838, PDB ID: 1ACC.
136. Little, S.; Novak, J. P.; Lowe, J. R.; Leppla, S.; Singh, Y.; Klimpel, K. R.; Lidgerding, B. C.; Friedlander, A. *Microbiology* **1996**, *142*, 707-715.
137. Flick-Smith, H. C.; Walker, N. J.; Gibson, P.; Bullifent, H.; Hayward, S.; Miller, J.; Titball, R. W.; Williamson, E. D. *Infect. Immun.* **2002**, *70*, 1653-1656.
138. Reed, D. S.; Smoll, J.; Gibbs, P.; Little, S. *Cytometry* **2002**, *49*, 1-7.
139. Santelli, E.; Bankston, L. A.; Leppla, S. H.; Liddington, R. C. *Nature* **2004**, *430*, 905-908.
140. Wild, M. A.; Xin, H.; Maruyama, T.; Nolan, M. J.; Calveley, P. M.; Malone, J. D.; Wallace, M. R.; Bowdish, K. S. *Nature Biotech.* **2003**, *21*, 1305-1306.
141. Ingram, R. S.; Hostetler, M. J.; Murray, R. W. *J. Am. Chem. Soc.* **1997**, *119*, 9175-9178.
142. Roitt, I. M.; Delves, P. J., *Roitt's Essential Immunology*. Blackwell Science: Oxford, 2001.
143. Zhang, J.; Xu, J.; Li, G.; Dong, D.; Song, X.; Guo, Q.; Zhao, J.; Fu, L.; Chen, W. *Biochem. Biophys. Res. Commun.* **2006**, *341*, 1164-1171.
144. Chen, Z.; Moayeri, M.; Zhou, Y.-H.; Leppla, S.; Emerson, S.; Sebrell, A.; Yu, F.; Svitel, J.; Schuck, P.; St. Claire, M.; Purcell, R. *J. Infect. Dis.* **2006**, *193*, 625-633.
145. Gubbins, M. J.; Berry, J. D.; Corbett, C. R.; Mogridge, J.; Yuan, X. Y.; Schmidt, L.; Nicolas, B.; Kabani, A.; Tsang, R. S. *FEMS Immunol. Med. Microbiol.* **2006**, *47*, 436-443.
146. Gu, M.-L.; Leppla, S. H.; Klinman, D. M. *Vaccine* **1999**, *17*, 340-344.
147. Francis, M. J., Synthetic Peptides. In *Vaccine Protocols*, 1 ed.; Robinson, A.; Farrar, G. H.; Wiblin, C. N., Ed. Humana Press: Totowa, New Jersey, 1996; 75-90.
148. Virella, G.; Bierer, B. E., The Induction of an Immune Response: Antigens, Lymphocytes, and Accessory Cells. In *Medical Immunology*, 5 ed.; Virella, G., Ed. Marcel Dekker: New York, 2001; 51-76.

149. Paciotti, G. F.; Myer, L.; Weinreich, D.; Goia, D.; Pavel, N.; McLaughlin, R. E.; Tamarkin, L. *Drug Delivery* **2004**, *11*, 169-183.
150. Hillyer, J. F.; Albrecht, R. M. *J. Pharm. Sci.* **2001**, *90*, 1927-1936.
151. Visaria, R. K.; Griffin, R. J.; Williams, B. W.; Ebbini, E. S.; Paciotti, G. F.; Song, C. W.; Bischof, J. C. *Mol. Cancer Ther.* **2006**, *5*, 1014-1020.
152. Hainfeld, J. F.; Slatkin, D. N.; Smilowitz, H. M. *Phys. Med. Biol.* **2004**, *49*, N309-N315.
153. Hainfeld, J. F.; Slatkin, D. N.; Focella, T. M.; Smilowitz, H. M. *Brit. J. of Rad.* **2006**, *79*, 248-253.
154. O'Neal, D. P.; Hirsch, L. R.; Halas, N. J.; Payne, J. D.; West, J. L. *Cancer Letters* **2004**, *209*, 171-176.
155. Wang, H.; Huff, T. B.; Zweifel, D. A.; He, W.; Low, P. S.; Wei, A.; Cheng, J.-X. *Proc. Natl. Acad. Sci. USA* **2005**, *102*, 15752-15756.
156. Niidome, T.; Yamagata, M.; Okamoto, Y.; Akiyama, Y.; Takahashi, H.; Kawano, T.; Katayama, Y.; Niidome, Y. *J. Control. Release* **2006**, *114*, 343-347.
157. Ziegler, J.; Chang, R. T.; Wright, D. W. *J. Am. Chem. Soc.* **1999**, *121*, 2395-2400.
158. Skelton, N. J.; Chazin, W. J., *Peptide and Protein Drug Analysis: Solution Structure Determination of Proteins by Nuclear Magnetic Resonance Spectroscopy*. Marcel Dekker, Inc.: New York, 2000.
159. Ellman's Reagent. <http://www.piercenet.com/files/0311dh4.pdf> (Jan 2005),
160. Biodesign International. <http://www.biodesign.com> (2004),
161. Godfrey, M. A. J., Immunoaffinity and IgG receptor technologies. In *Affinity Separations*, ed.; Matejtschuk, P., Ed. IRL Press: Oxford, 1997; 141-193.
162. Virella, G., Hypersensitivity Reactions. In *Medical Immunology*, 5 ed.; Virella, G., Ed. Marcel Dekker: New York, 2001; 397-410.
163. Stewart-Tull, D. E. S., The Use of Adjuvants in Experimental Vaccines. In *Vaccine Protocols*, 1 ed.; Robinson, A.; Farrar, G. H.; Wiblin, C. N., Ed. Humana Press: Totowa, 1996; 135-155.
164. Peterson, R. R.; Cliffel, D. E. *Anal. Chem.* **2005**, *77*, 4348-4353.
165. Bigioni, T. P.; Whetten, R. L.; Dag, Ö. *J. Phys. Chem. B* **2000**, *104*, 6983-6986.
166. Huang, T.; Murray, R. W. *J. Phys. Chem. B* **2001**, *105*, 12498-12502.

167. Huang, T.; Murray, R. W. *J. Phys. Chem. B* **2003**, *107*, 7434-7440.
168. Wang, G.; Huang, T.; Murray, R. W.; Menard, L.; Nuzzo, R. G. *J. Am. Chem. Soc.* **2005**, *127*, 812-813.
169. Templeton, A. C.; Wuelfing, W. P.; Murray, R. W. *Acc. Chem. Res.* **2000**, *33*, 27-36.
170. Zhao, Y.; Jiang, Y.; Fang, Y. *Chem. Phys.* **2006**, *323*, 169-172.
171. Cheng, P. P. H.; Silvester, D.; Wang, G.; Kalyuzhny, G.; Douglas, A.; Murray, R. W. *J. Phys. Chem. B* **2006**, *110*, 4637-4644.
172. Schneider, G.; Decher, G.; Nerambourg, N.; Praho, R.; Werts, M. H. V.; Blanchard-Desce, M. *Nano Letters* **2006**, *6*, 530-536.
173. Wargnier, R.; Baranov, A. V.; Maslov, V. G.; Stsiapura, V.; Artemyev, M.; Pluot, M.; Sukhanova, A.; Nabiev, I. *Nano Letters* **2004**, *4*, 451-457.
174. Dubertret, B.; Calame, M.; Libchaber, A. J. *Nature Biotech.* **2001**, *19*, 365-370.
175. Zhang, J.; Malicka, J.; Gryczynski, I.; Lakowicz, J. R. *Anal. Biochem.* **2004**, *330*, 81-86.
176. Lakowicz, J. R.; Shen, Y.; D'Auria, S.; Malicka, J.; Fang, J.; Gryczynski, Z.; Gryczynski, I. *Anal. Biochem.* **2002**, *301*, 261-277.
177. Hernandez, F. E.; Yu, S.; Garcia, M.; Campiglia, A. D. *J. Phys. Chem. B* **2005**, *109*, 9499-9504.
178. Thomas, K. G.; Kamat, P. V. *J. Am. Chem. Soc.* **2000**, *122*, 2655-2656.
179. Cliffel, D. E.; Zamborini, F. P.; Gross, S. M.; Murray, R. W. *Langmuir* **2000**, *16*, 9699-9702.
180. Eklund, S. E.; Cliffel, D. E. *Langmuir* **2004**, *20*, 6012-6018.
181. Novak, J. P.; Nickerson, C.; Franzen, S.; Feldheim, D. L. *Anal. Chem.* **2001**, *73*, 5758-5761.
182. Brousseau, L. C., III; Novak, J. P.; Marinakos, S. M.; Feldheim, D. L. *Adv. Mater.* **1999**, *11*, 447.
183. McConnell, W. P.; Novak, J. P.; Brousseau, L. C., III; Fuierer, R. R.; Tenent, R. C.; Feldheim, D. L. *J. Phys. Chem. B* **2000**, *104*, 8925-2930.
184. Novak, J. P.; Feldheim, D. L. *J. Am. Chem. Soc.* **2000**, *122*, 3979-3980.

185. Peng, X.; Wilson, T. E.; Alivisatos, A. P.; Schultz, P. G. *Angew. Chem. Int. Ed.* **1997**, *36*, 145-147.
186. Elghanian, R.; Storhoff, J. J.; Mucic, R. C.; Letsinger, R. L.; Mirkin, C. A. *Science* **1997**, *277*, 1078-1081.
187. Hone, D. C.; Haines, A. H.; Russell, D. A. *Langmuir* **2003**, *19*, 7141-7144.
188. McIntyre, J. O.; Fingleton, B.; Wells, K. S.; Piston, D. W.; Lynch, C. C.; Gautam, S.; Matrisian, L. M. *Biochem. J.* **2004**, *377*, 617-628.
189. Pham, W.; Choi, Y.; Weissleder, R.; Tung, C.-H. *Bioconjugate Chem.* **2004**, *15*, 1403-1407.
190. Wosnick, J. H.; Mello, C. M.; Swager, T. M. *J. Am. Chem. Soc.* **2005**, *127*, 3400-3405.
191. Chang, E.; Miller, J. S.; Sun, J.; Yu, W. W.; Colvin, V. L.; Drezek, R.; West, J. L. *Biochem. Biophys. Res. Commun.* **2005**, *334*, 1317-1321.
192. Guarise, C.; Pasquato, L.; De Filippis, V.; Scrimin, P. *Proc. Natl. Acad. Sci. USA* **2006**, *103*, 3978-3982.
193. Chen, E. I.; Li, W.; Godzik, A.; Howard, E. W.; Smith, J. W. *J. Biol. Chem.* **2003**, *278*, 17158-17163.
194. Instructions - Protein A, A/G, L, and G. <http://www.piercenet.com> (Sept 2005),
195. Yu, J.-S.; Liao, H.-X.; Gerdon, A. E.; Huffman, B. J.; Searce, R. M.; McAdams, M.; Alam, S. M.; Popernack, P.; Sullivan, N.; Wright, D. W.; Cliffler, D. E.; Nabel, G.; Haynes, B. F. *J. Vir. Meth.* **2006**, *137*, 219-228.
196. Sumerel, J.; Lewis, J.; Doraiswamy, A.; Deravi, L. F.; Sewell, S. L.; Gerdon, A. E.; Wright, D. W.; Narayan, R. J. *Biotechnol. J.* **2006**, *1*, 976-987.
197. Gies, A. P.; Hercules, D. M.; Gerdon, A. E.; Cliffler, D. E. *J. Am. Chem. Soc.* **2006**, (accepted).

CURRICULUM VITAE

Aren E. Gerdon

Vanderbilt University
Department of Chemistry
Station B 351822
Nashville, TN 37235
Lab Phone: (615) 322-5013
E-mail: a.gerdon@vanderbilt.edu

Education

- PhD, Analytical Chemistry, Vanderbilt University, Nashville, TN, Dec 2006
Thesis title: "Peptide Epitope Functionalized Nanoclusters for Life Science Applications"
Advisor: David E. Cliffel GPA: 3.762
- BA, Chemistry (*cum laude*, Honors), Hanover College, Hanover, IN, May 2002
Research title: "Nitration of Human Serum Albumin with Peroxynitrite: Detection of Nitrated Tyrosine Residues with Mass Spectrometry"
Advisor: Paul Austin GPA: 3.682

Course Work – Vanderbilt University

- Fall 2002 – Inorganic Chemistry, Bioorganic Chemistry, Electrochemistry
- Spring 2003 – Biochemistry: Molecular Structure and Function, Bioinorganic Chemistry, Separation Methods
- Fall 2003 – Chemistry Seminar
- Spring 2004 – Chemistry Seminar, Advanced Analytical Chemistry

Honors and Awards

- 6th Annual VINSE Nanoscience Poster Competition Winner, 2005
- NIH Chemical Biology Training Grant Recipient, 2003-2005
- Vanderbilt University Institute of Chemical Biology Fellow, 2002-2004
- Vanderbilt University Warren Fellow, 2002
- Hanover College Ned Guthrie Chemistry Award Recipient, 2002
- Hanover College Presidential Scholar, 1998-2002
- Hanover College Music Scholar, 1998-2002
- Member of Gamma Sigma Pi Honor Society
- Member of Mortar Board Honor Society
- Member of Alpha Lambda Delta Honor Society
- Member of Phi Eta Sigma Honor Society

Professional Activities and Service

- American Chemical Society, National Member, 2003-Present

- Future Faculty Preparation Program Participant, Vanderbilt University, 2002-2005
- Vanderbilt University Chemistry Department Steering Committee Leader, 2003-2005
- American Chemical Society, Hanover College Chapter, President, 2001-2002
- American Chemical Society, Hanover College Chapter, Chair of Publicity, 2000-2001

Teaching Experience

2002-2006 Vanderbilt Students Volunteering for Science, Vanderbilt University

- Team leader in many trips to local 5th and 6th grade classrooms to teach science lessons

2005-2006 Talent Identification Program, Duke University

- Co-Instructor (2005) and Instructor (2006) of a three-week intensive course on Nanotechnology taught to gifted 9th and 10th grade students from across the country

Research Experience and Qualifications

2002-2006 Graduate Research Assistant, Vanderbilt University

Advisor: David E. Cliffel

- Developed new interfaces between immunology and monolayer-protected nanoclusters
- Experienced in materials synthesis and functionalization and bioconjugation techniques
- Developed analytical technique, quartz crystal microbalance, for evaluation of bio-interfaces
- Experienced in immunosensor design (QCM, SPR, ELISA) and materials characterization (NMR, TEM, TGA, UV/visible spectroscopy).
- Familiar with electrochemical analysis, fluorescence spectroscopy, infrared spectroscopy, AFM, circular dichroism, chromatography, capillary electrophoresis, free flow electrophoresis, and mass spectrometry.
- Experience with BSL 2 work: human blood, live virus, mouse antibody production

2001-2002 Undergraduate Research Assistant, Hanover College

Advisor: Paul Austin

- Studied effect of reactive oxygen species (peroxynitrite) on albumin protein
- Gained experience with liquid chromatography, ESI/TOF MS, and trypsin-digestion

2001 Summer Intern, ELANCO (Eli Lilly), Greenfield, IN

Advisor: Scott Holmstrom

- Fluorescently labeled pharmaceutical compounds for low detection limits

- Gained experience with liquid chromatography, fluorescent labels, and instrument design

Publications

- Richardson, K.M.; Gerdon, A.E.; McIntyre, J.O.; Cliffel, D.E. “Coupled Monolayer-Protected Clusters Exhibit Enhanced Near-IR Fluorescence” *J. Am. Chem. Soc.* **2006**, (submitted).
- Gies, A.P.; Hercules, D.M.; Gerdon, A.E.; Cliffel, D.E. “Electrospray Mass Spectrometry Study of Tiopronin Monolayer-Protected Gold Nanoclusters” *J. Am. Chem. Soc.* **2006**, (submitted).
- Sumerel, J.; Lewis, J.; Doraiswamy, A.; Deravi, L.F.; Sewell, S.L.; Gerdon, A.E.; Wright, D.W.; Narayan, R.J. “Piezoelectric ink jet processing of materials for medical and biological applications” *Biotechnol. J.* **2006**, *1*, 976-987.
- Yu, S-J.; Liao, H-X.; Gerdon, A.G.; Huffman, B.J.; Scarce, R.M.; McAdams, M.; Alam, S.M.; Popernack, P.; Sullivan, N.; Wright, D.W.; Cliffel, D.E.; Nabel, G.; Haynes, B.F. “Detection of Human and Non-human Primate Ebola Virus Envelope Using Monoclonal and Polyclonal Antibodies in ELISA, Surface Plasmon Resonance, and a Quartz Crystal Microbalance Immunosensor” *J. Vir. Methods* **2006**, *137*, 219-228.
- Gerdon, A.E.; Wright, D.W.; Cliffel, D.E. “Epitope Mapping of the Protective Antigen of B. Anthracis Using Nanoclusters Presenting Conformational Peptide Epitopes.” *Angew. Chem. Int. Ed.* **2006**, *45*, 594-598.
- Gerdon, A.E.; Wright, D.W.; Cliffel, D.E. “Hemagglutinin Linear Epitope Presentation on Monolayer-Protected Nanoclusters Elicits Strong Antibody Binding.” *Biomacromolecules* **2005**, *6*, 3419-3424.
- Gerdon, A.E.; Wright, D.W.; Cliffel, D.E. “Quartz Crystal Microbalance Characterization of Nanostructure Assemblies in Biosensing” in *Characterization Tools for Nanosystems in Life Sciences*, 1st Ed, Kumar, C. Ed, Wiley-VCH: New York, **2005**, 109-144.
- Gerdon, A.G.; Wright, D.W.; Cliffel, D.E. “Quartz Crystal Microbalance Detection of Glutathione-Protected Nanoclusters Using Antibody Recognition.” *Anal. Chem.* **2005**, *77*, 304-310.

Presentations

- Gerdon, A.E.; Wright, D.W.; Cliffel, D.E. “Conformational Antigen Mimics Interface with Monoclonal Antibodies for Epitope Mapping.” *Abstracts of Papers*, Gordon Research Conference: Biointerface Science, Les Diablerets, Switzerland, 2006; Poster Session I - 26.

- Gerdon, A.E.; Huffman, B.J.; Wright, D.W.; Cliffel, D.E. "Detection of Ebola Glycoprotein Using a Quartz Crystal Microbalance Immunosensor." *Abstracts of Papers*, 231st National Meeting of the American Chemical Society, Atlanta, GA, 2006; I&EC 0001.
- Gerdon, A.E.; Wright, D.W.; Cliffel, D.E. "Epitope Mapping of the Protective Antigen of B. Anthracis Using Nanoclusters Presenting Conformational Peptide Epitopes." *Abstracts of Papers*, Pittsburg Conference, Orlando, FL, 2006; Biomedical Analysis 850-8.
- Gerdon, A.E.; Wright, D.W.; Cliffel, D.E. "Epitope Mapping of the Protective Antigen of B. Anthracis Using Nanoclusters Presenting Conformational Peptide Epitopes." *Abstracts of Papers*, International Chemical Congress of Pacific Basin Societies, Honolulu, HI, 2005; ANYL 890.
- Gerdon, A.E.; Huffman, B.J.; Wright, D.W.; Cliffel, D.E. "Detection of Ebola Capsid Protein Using a Quartz Crystal Microbalance Immunosensor." *Abstracts of Papers*, 57th Southeast/61st Southwest Joint Regional Meeting of the American Chemical Society, Memphis, TN, 2005; Biosensors 160.
- Gerdon, A. E.; Wright, D. W.; Cliffel, D. E. "QCM Detection of Glutathione Protected Nanoclusters Using Antibody Recognition." *Abstracts of Papers*, Pittsburgh Conference, Orlando, FL, 2005; Nanotechnology: Applications 440-10.
- Gerdon, A. E.; Wright, D. W.; Cliffel, D. E. "QCM Detection of Glutathione Protected Nanoclusters Using Antibody Recognition." *Abstracts of Papers*, 56th Southeast Regional Meeting of the American Chemical Society, Research Triangle Park, NC, 2004; General Poster IV 362.
- Gerdon, A. E.; Wright, D. W.; Cliffel, D. E.; Mernaugh, R. "Confirmed Binding of Single Chain (ScFv) Recombinant Antibodies to Zero Valent Metals with Quartz Crystal Microbalance." *Abstracts of Papers*, 227th National Meeting of the American Chemical Society, Anaheim, CA, 2004; INOR 980.
- Gerdon, A.E.; Mernaugh, R.; Wright, D. W.; Cliffel, D. E. "Quartz Crystal Microbalance Study of Interfaces between Inorganic Materials and Biological Components." Presented as Invited Speaker, Sewanee College, Sewanee, TN, 2003.
- Gerdon, A.; Wright, D.; Cliffel, D.; Mernaugh, R. "Confirmed Binding of Single Chain (ScFv) Recombinant Antibodies to Zero Valent Metals with Quartz Crystal Microbalance." *Abstracts of Papers*, 55th Southeast Regional Meeting of the American Chemical Society, Atlanta, GA, 2003; INOR 467.

References

- Prof. David E. Cliffel
Vanderbilt University, Department of Chemistry, Station B 351822, Nashville,
TN 37235
(615) 343-3937, d.cliffel@vanderbilt.edu
- Prof. David W. Wright
Vanderbilt University, Department of Chemistry, Station B 351822, Nashville,
TN 37235
(615) 322-2536, david.wright@vanderbilt.edu
- Prof. Ned Porter
Vanderbilt University, Department of Chemistry, Station B 351822, Nashville,
TN 37235
(615) 343-4371, n.porter@vanderbilt.edu
- Prof. Eva Harth
Vanderbilt University, Department of Chemistry, Station B 351822, Nashville,
TN 37235
(615) 343-3405, eva.m.harth@vanderbilt.edu